Department of Mechanical, Bioresources and Biomedical Engineering,

College of Science, Engineering and Technology

Modelling of the fluid structure interaction of the horizontal axis bio-inspired wind turbine blade and effect on annual energy production

By

Arinao Netshivhulana

Submitted in fulfillment of the requirements for the Master of Engineering degree

Supervisor: Prof H Ngwangwa

Co-supervisors: Prof F. Nemavhola

Prof T Pandelani

Dr D. Modungwa

May 2026

ACKNOWLEDGEMENT

I wish to convey my profound appreciation to everybody who assisted me during the course of this Master's thesis.

I am deeply grateful to my supervisors, Prof. H Ngwangwa, Prof. T Pandelani, Prof. F Nemavhola, and Dr. D. Modungwa, for their steadfast direction, perceptive comments, and continual support. Their experience and guidance have been important in influencing both the trajectory and calibre of this study. To Mr. Lebea Lebogang, I express my profound gratitude for your mentorship and advice during this research.

I express my gratitude to the faculty and staff of Department of Mechanical, Bioresources and Biomedical Engineering at University of South Africa (UNISA) for fostering an environment of academic rigor and curiosity. Special thanks to my group of researchers, whose collaborative spirit and technical discussions enriched my understanding and challenged me to grow.

My coworkers and friends deserve my gratitude for their companionship, brainstorming late night sessions and moral support. Your presence made this journey not only bearable but memorable. My appreciation to Mr Obakeng Levy Siko for a learning journey, guidance and a sharing of powerful knowledge on ANSYS software.

To my family Mashudu (Husband) and my children, Khangwelo, Mpho, Phathutshedzo and Tshilidzi, your love, patience, and belief in me have been my anchor. I dedicate this work to you not forgetting my twin sister Asiashu Novhe who never gave up encouraging me.

Finally, I acknowledge the inspiration drawn from nature and sustainable engineering principles, which continue to fuel my passion for biomimicry and renewable energy solutions.

DECLARATION OF INTEREST

I hereby certify that the dissertation I have submitted to the University of South Africa in partial fulfilment of the requirements for the Master of Engineering degree is original to me and has not been submitted anywhere else. To the best of my ability, I further affirm that this dissertation was written in accordance with the University of South Africa (Guidelines for Archiving of Electronic Versions of Theses and Dissertations (ETDs). All sources that were used or quoted were also acknowledged with complete reference.

Arinao Glory Netshivhulana ------------------------------------

Candidate **Signature**

ABSTRACT

In response to South Africa's ongoing energy crisis, the exploration of renewable energy technologies has become increasingly urgent. Wind energy, as one of the fastest growing renewable sources, offers significant potential for sustainable power generation. In this study, performance improvement of Horizontal Axis Wind Turbines (HAWTs) was explored by employing a bio inspired blade design method. To improve the aerodynamic efficiency, inspired by the aerodynamically efficient wing shape of the albatross, a corrugated version of the GOE174 airfoil was designed. The original airfoil geometry was rebuilt from NACA data and methodically adjusted by amplitude functions for generating corrugations. The resulting 2D profile was extruded in Solid Edge to get a full 3D blade model and then analyzed with ANSYS Fluent 2025R1. Computational fluid dynamics (CFD) simulations were performed using the k-ω SST turbulence model to examine the lift and drag characteristics over a wide variety of angles of attack.

The main goal was to investigate the potential of bio-inspired corrugation to boost the aerodynamic efficiency compared to smooth blade. The results revealed that corrugated geometry always have higher drag but offer better lift-to-drag ratios at low angles of attack, particularly around 2.71 m/s where stall delay is noted. The corrugated airfoil performs similarly at 3.47 m/s, with a marginal edge at 20° angle of attack, with a power coefficient (Cp) of 0.466 relative to 0.459 for the smooth profile. Analysis of the Annual Energy Production (AEP) showed a small but measurable increase of 1.4%: 16.753 kWh/year for the corrugated blade compared to 16.518 kWh/year for the smooth blade. These efficiencies are minor but important to long term turbine operating in low to moderate wind environments. The results demonstrate the promise of bio-inspired corrugated patterns for HAWT performance improvement, tying computational modelling to experimental applicability, and emphasize the relevance of biomimicry in the development of renewable energy technology.

Error comparison between CFD and wind tunnel experiments indicated good agreement at low velocity ($\sigma = 0.156$), considerable variability at 3.47 m/s ($\sigma = 0.322$) and significant disparities at 5.36 m/s ($\sigma = 0.908$). The corrugated airfoil showed better lift stability, stall delay and higher efficiency, which is beneficial for the practical application in HAWTs.

TABLE OF CONTENTS

LIST OF FIGURES

LIST OF TABLES

LIST OF ABBREVIATIONS & GLOSSARY

A – Wing Area

AoA – Angle of Attack

CD – Coefficient of Drag

CFD – Computational Fluid Dynamis

CL – Coefficient of Lift

D – Drag Force

HAWT - Horizontal Axis Wind Turbine

L – Lift Force

NACA – National Advisory Committee for Aeronautics

Rho – Air Density

V – Velocity of Fluid Flow

VAWT – Vertical Axis Wind Turbines

NOMENCLATURE

ρ - Density

μ – dynamic viscosity

α – Alpha, angle of attack

CHAPTER 1: BACKGROUND TO THE RESEARCH

1.1. Introduction

There is an ever-increasing need for research in alternative power generating plants and performance improvements thereof. This study examined the benefits of wind energy as a rapidly expanding renewable energy source. The nature offers the finest solutions because it has created objects, processes, materials, and functions to maximize efficiency (Pellerito et al. 2019). The present research has pursued the modelling of the fluid-structure interaction of a horizontal-axis bio-inspired airfoil, constructed on the basis of the wing morphology of the most efficient birds in terms of aerodynamics, such as the albatross (Pellerito et al. 2019). Among renewable energy sources, the conversion of wind energy from kinetic to mechanical energy through turbines has been one of the most improved technologies in the recent decade (Gaitan-Aroca et al. 2020)

Figure 1: The wings of an Albatross bird(Pellerito et al. 2019)

The most crucial component of the wind energy sector is the wind turbine. Horizontal axis wind turbines (HAWT) as shown of figure 2 and vertical axis wind turbines (VAWT) are the two primary categories (Gaitan-Aroca et al. 2020). HAWT are currently the most used in industry because VAWT have been discovered to have issues controlling the rotor, making them less flexible and ineffective at absorbing energy (Gaitan-Aroca et al. 2020).

Figure 2: The group of HAWTs in Wind Farm (Sedaghat et al. 2012)

The present study builds upon this biomimetic foundation by acquiring the geometry data of the GOE174 airfoil and reconstructing its two-dimensional profile using Microsoft Excel. Then a corrugated version was made by adding a sinusoidal amplitude function to the baseline surface coordinates, developing a redesigned geometry which looks like natural wing structures. The corrugated profile was merged into Solid Edge software to construct a three-dimensional protruded wing form for computational and experimental investigation. The geometry was then imported into ANSYS Fluent 2025R1 for computational fluid dynamics (CFD) simulations, where the k-ω SST turbulence model was chosen for its known ability to accurately anticipate high pressure gradients and adverse pressure regions. The CFD simulation was performed to study the effect of corrugation for different angles of attack. The intent was to determine the optimum geometry for the highest lift generation, and hence the highest wind turbine efficiency.

Wind tunnel testing was conducted to experimentally validate the computational analysis. The corrugated airfoil, created through additive manufacturing, was placed in a test chamber, and a force gauge was set up to measure both lift and drag forces. These trials generated real data in controlled conditions, enabling a direct comparison with the CFD projections. The triangulation of computational and experimental results ensures validity and reliability of the results and encourages methodological rigor. Ethical issues were taken care of by explicit reporting, good data management and understanding of methodological limitations. The importance of corrugated airfoils lies in their ability to utilize fluid-structure interaction (FSI) phenomena. When air flows over the airfoil, the difference in air velocity over the top and bottom of the airfoil produces a pressure difference that causes aerodynamic loading.

The corrugated structure deforms a little elastically, changing its effective camber and angle of attack. This structural change alters the flow field, increasing the pressure difference and maintaining lift. The dynamic equilibrium created by the bidirectional coupling between fluid forces and structural response stabilizes aerodynamic performance, particularly in the presence of stall onset and adverse pressure gradients. Mulligan (2020)showed that elasto flexible lifting surfaces can raise camber, delay stall, and enhance energy production by up to 35%. Although alterations of the chamber are not included in the present work, emphasis is laid on geometric corrugation as a technique of improving the aerodynamic properties. Importantly, the corrugations must be precisely calibrated since increasing them too much might lead to a loss of lift and increase in drag.

This work contributes to current knowledge of bio-inspired wind turbine blade design by systematically merging computer modelling, experimental validation and theoretical analysis. The methodological sections offer a detailed platform for the evaluation of the aerodynamic performance of corrugated airfoils in the context of wind energy applications. The present work intends to improve the understanding of the possible modelling of the wind turbine performance using the biomimetic design by performing the analysis of the coupled fluid-structure interaction dynamics and the measurements of the lift and drag characteristics at different angles of attack. These results highlight the need of innovative blade designs in addressing worldwide energy issues and demonstrate the potential of bio-inspired engineering for future sustainable power production.

The aerodynamic center is precisely one quarter chord back of the leading edge of a cambered airfoil which has unusual forms on both sides of the camber line. In contrast to symmetric airfoils, cambered airfoils have a reduced stall angle(Ansari et al. n.d.). The airfoil, whether symmetrical or cambered, has elements such as chord and camber lines, edges, and surfaces, as seen in Figure 3.

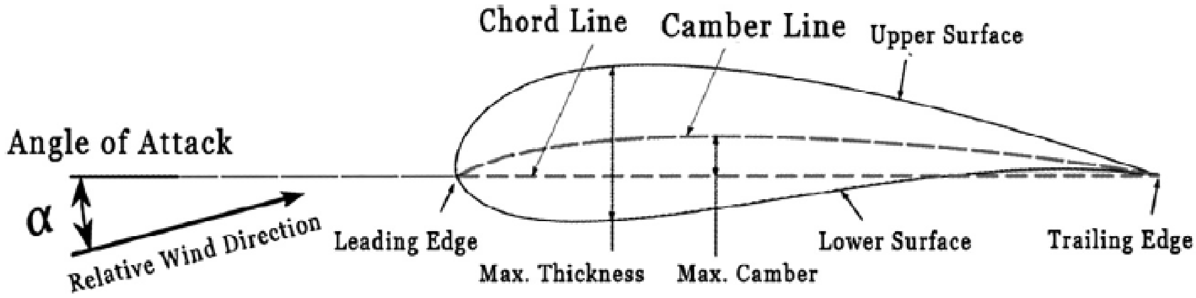

Figure 3: The airfoil geometry (Gray et al. 2021)

The examination of the blade's aerodynamics is the first step in achieving higher power performance. According to Patel et al. (2014), the aerodynamic design phase of the wind turbine blade considered the airfoil shape, a specified tip speed ratio, the rated wind velocity, and a designated angle of attack**Error! Reference source not found.** Turbine blades are moved by lift and drag forces, which transform wind energy into the kinetic energy of the blades. The kinetic energy of the wind is captured by wind turbines, which then transform it into mechanical and electrical energy through the generator and blades, respectively Jureczko et al. (2005). The rotor is turned by the torque produced throughout the length of the turbine blades, which are attached to a single rotor shaft (Jureczko et al. 2005). The power that the wind turbine produces is dependent on the aerodynamic forces that are applied to its blades (Jureczko et al. 2005). The individual blades of a wind turbine make up the majority of its design (Jureczko et al. 2005)**.** Wind turbines often undergo deflections due to aerodynamic loads during operation, and the implementation of elastic blades as a proactive angle mechanism has been previously examined by Mulligan (2020).

An elasto-flexible lifting surface increases the chamber, increasing lifting capacities and delaying the halt arrival, preventing the abrupt decline in lift, according to wind tunnel experiments. This had boosted wind turbine energy output by up to 35% according to Mulligan (2020). This research did not consider the chamber changes. In order to change the aerodynamic qualities, study has focused on changing the complete geometry of the airfoil face (Mulligan 2020).

However, a corrugated skin needs to be tuned properly because enlarging the corrugations would reduce lift and increase drag (Mulligan 2020).

1.2. Problem identification

Despite advances in wind turbine technology, the aerodynamic efficiency of traditional smooth airfoil designs remains limited, particularly at high angles of attack where flow separation and stall can significantly reduce performance. Traditional Computational Fluid Dynamics (CFD) models are valuable but may not capture the full complex interplay between airflow and innovative, bio-inspired geometries such as corrugated wings. However, the effect of these bio-inspired corrugated patterns on the lift and drag characteristics and the degree of the correlation between the CFD predictions and the experimental data is limited to the existing knowledge. This deficiency hampers the advancement of more efficient wind turbine blades capable of optimizing the energy capture under a wide range of operating conditions.

Given that lift and drag forces are the principal factors influencing turbine performance, and airfoil geometry is dictated by the exact coordinates of its surfaces, it is essential to examine bio-inspired corrugated airfoils using a combination of computational and experimental methods which is the main problem identification of this study.

1.3. Objectives and aims

This study aimed to enhance the aerodynamic efficiency of a HAWT through the development of a corrugated, bio-inspired blade design. The airfoil data used was derived from the albatross bird wing on NACA website. The primary aim was to enhance the overall performance by modelling the bio-inspired airfoil from albatross wing profile, simulate and analyze lift and drag coefficient across varying angles of attack using a 3D wing model derived from NACA eirfoil data, and to validate these results against wing tunnel experiment. The specific objectives were to:

a) Identify bio-inspired turbine blade geometries by analysing and adopting shape derived from bird wings, with particular focus on the albatross wing profile.
b) Determine and compare the aerodynamic efficiency of corrugated bird wing-shaped airfoil to establish performance benchmarks relative to conventional turbine blade design.

c) Develop a modified corrugated airfoil profile using MS Excel based on NACA-derived albatross wing coordinated to maximise aerodynamic efficiency.
d) Create a 3D model of corrugated wing using Solid edge (student version) and further model it in ANSYS for simulation versus angle of attack.
e) Validate modelled design results of a corrugated airfoil wing by computational and experimental approaches to assure correctness and applicability of the actual world.
f) Determine the effect on annual energy production.

1.4. Modelling assumptions

For the sake of modelling, certain simplifications were included to enable effective and controllable aerodynamic simulation within the constraints of the program used and the computational resources available. These assumptions simplify the study while maintaining a decent level of accuracy of the performance of the low-speed wings:

a) Steady-state flow conditions

   The simulation excludes transitory phenomena such as gusts, oscillations, or dynamic stall that may arise in a non-time-invariant airflow surrounding the corrugated airfoil. This approach was devised to elucidate the average aerodynamic performance at each angle of attack, facilitating expedited calculations.

b) Ignoring the effects of compressibility at low speeds

   The air is assumed to be incompressible with no appreciable loss of precision. This simplifies the governing equations and reduces the processing effort.

c) Idealized boundary layer conditions

   Under ideal circumstances, the boundary layer was modelled, frequently with turbulence models such as k-ε or k-ω, which fail to resolve fine-scale laminar-to-turbulent transitions. This method provides a useful compromise between processing cost and simulation accuracy, but it might miss minute flow events close to the surface.

1.5. Limitation on wind tunnel experiment

The wind tunnel was comprised of a wheel to turn the blade to various angles of attack a desired. The wheel runs with interval of 0^0, 30^0,60^0,90^0, -30^0, -60^0 and -90^0.

The following are limitations:

a) When a corrugated airfoil is at angle of attack ranges from -20^0 - 20^0, the wind that is blowing through the fan would not be able to turn the turbine as it is parallel to the flow, therefore it is difficult to get the results no matter the speed of the fan.
b) The corrugated blade is parallel to the flow; these angles are not allowing the pressure differential on both surfaces to generate lift and rotational force.
c) The fan placement or tunnel design has a limit when it comes to the angles of attack.
d) The corrugated aifoil orientation on the said angles of attack did not allow effective lift and drag generation.
e) The range of testable combinations is restricted by tunnel size and mounting hardware and flow uniformity constraints. Wall interference and blockage effects can alter the flow pattern around the model and lead the simulation to depart from the ideal conditions.
f) The physical model evaluated in the wind tunnel is a scaled-down version of the full-size applications. This scaling results in fluctuations of Reynolds numbers, impacting the behaviour of the boundary layer and the characteristics of flow separation. As a result, actual conditions may not be accurately represented by the recorded aerodynamic performance.

1.6. Outline of the dissertation

Chapter 1 is an overview of the primary purpose of this work and the key elements examined during airfoil modelling and simulation, which serves as an introduction. The major goal of the study was discussed in this section including the assumptions made towards simulating the corrugated airfoil. The constraints that the wind tunnel demonstrated during the laboratory experiment, as well as the goals and objectives of this investigation were explained in detail in this section.

Chapter 2 discussed the research conducted by different researchers, together with their findings and anything pertinent to this analysis of earlier work and known as Literature Review. More information about the different kinds of airfoils and the simulations that were done earlier is provided in this section. This section covered the different findings from the literature review.

Chapter 3 discusses the methodology for modelling the HAWT blade using a bio-inspired approach. It provides a detailed explanation of the information gathered from the NACA website and the created a corrugated airfoil using an Excel profile. The method of modelling the 3D corrugated airfoil in a CFD software, including meshing, boundary conditions, and simulation, was demonstrated in detail together with the excel profile of a corrugated airfoil that was loaded into Solid Edge (student version). The chapter went on to demonstrate the procedures followed during the Wind Tunnel demonstration in order to confirm with the CFD.

Chapter 4 is structured into five principal sections to elucidate and analyze the outcomes of the CFD simulation. The initial section delineates the data outcomes obtained during the simulation, succeeded by an analysis of their consequences. The second section examines the velocity and pressure contours at varying angles of attack, highlighting flow behaviour and pressure distribution over the corrugated airfoil surface. The third section shows graphical findings showing the fluctuation of lift and drag coefficients with attack angle, which provides insights in aerodynamic performance. The influence of inlet velocity on aerodynamic characteristic across angle of attack will be highlighted on section four of this chapter. Lastly the analyzation of the lift-to-drag coefficient ratio as an indication of angle of attack, offering a comparative metric for aerodynamic efficiency.

Chapter 5 is organized into four key sections to present and discuss the comparison on the CFD and wind tunnel experiment results of a corrugated airfoil. First section details the data results collected during experiment followed by a discussion of their implications. The second section presents graphical results illustrating the variation of lift and drag coefficient in relation to the angle of attack, proving insights into aerodynamic performance between CFD and wind tunnel experiment. The influence of inlet velocity on aerodynamic characteristic across angle of attack as compared to CFD behaviour was highlighted on section three of this chapter.

Lastly the analyzation of the lift-to-drag coefficient ratio as a function of angle of attack, offering a comparative metric for aerodynamic efficiency between CFD and wind tunnel experiment.

CHAPTER 2: LITERATURE REVIEW

2.1. Wind turbine

Wind turbine is a devise that converts wind power into electricity (Cabanillas Sánchez 2013). Wind turbines are either horizontal axis or vertical axis. Wind turbine with a rotor axis that is significantly parallel to the wind flow is referred to as a horizontal axis wind turbine (Cabanillas Sánchez 2013). The horizontal axis wind turbine was used in this study. The aerodynamic efficiency of a wind turbine is significantly influenced by the profiles of its blades (Jureczko et al. 2005). In comparison to other renewable energy technologies, more and more people are becoming interested in wind energy (Jureczko et al. 2005). The blade aerodynamic study is the initial step to improving power performance, see figure 4. During the aerodynamic design phase of wind turbine blades, it is essential to examine the airfoil shape, design tip speed ratio, design angle of attack, and rated wind speed (Cabanillas Sánchez 2013).

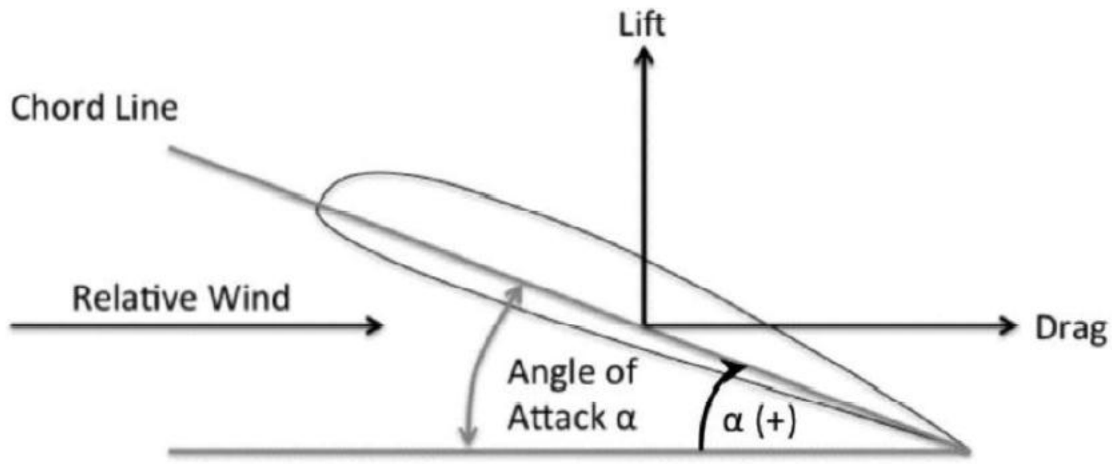

Figure 4: Airfoil geometry (Gray et al. 2021)

In its most basic form, direct airfoil design begins with an assumed airfoil shape such as a that from NACA airfoil database, identifies the section's most challenging feature, and corrects it. Until there is no longer a significant issue with the section, this procedure of addressing the most obvious issues with a given airfoil is repeated.

2.2. Wind turbine materials

Materials for wind turbine blades include resins composed of glass fibre reinforced polyester, glass fibre reinforced epoxy, and carbon fibre reinforced epoxy (Amjith et al. 2020). Glass fibres and a resin matrix work together to create composites that are sturdy, light, impervious to corrosion, and dimensionally stable. They often have lower manufacturing costs and offer excellent dielectric strength as well as good design flexibility (Amjith et al. 2020). Composites are adaptable, and these materials enable wind specialists to fix turbines more quickly and extend the life of the blades (Amjith et al. 2020).

2.3. Albatross bird wings

In general, birds may fly in a variety of ways, which can be further split into powered flight and unpowered flight (Pellerito et al. 2019). With a 3.5 m wingspan and an 8.5 kg weight, albatross can fly at top ground speeds of more than 35 m/s (Pellerito et al. 2019).

Without flapping their wings, these birds can maintain these speeds for up to eight hours. An albatross needs 81 W of power to fly at 19.5 m/s, assuming a maximum lift to drag ratio of 20 (Pellerito et al. 2019). Albatrosses are anticipated to navigate within the low Reynolds number flow zone ($7 \times 10^4 > Re > 2 \times 10^5$)(Muruga et al. 2021).

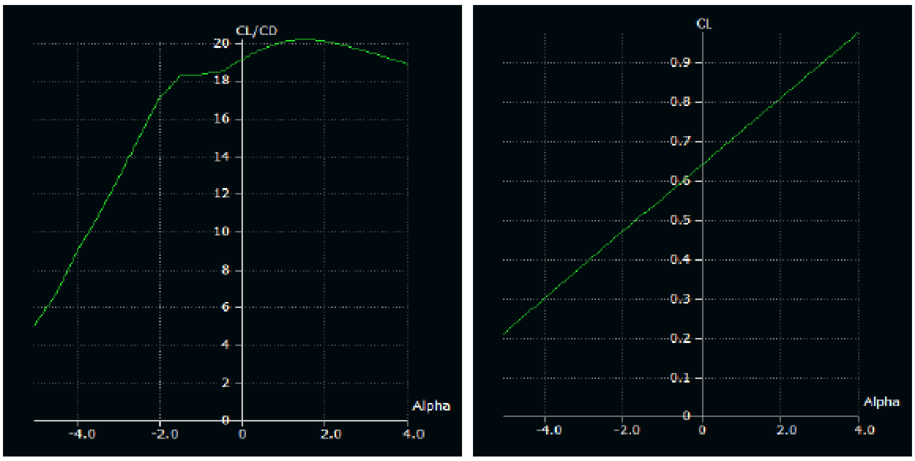

(a) Cl/Cd vs AoA (b) Cl vs AoA

Figure 5: Assessment of Aerodynamic Performance of GOE 173 Integrated into the Wing Model (Muruga et al. 2021)

According to Muruga et al. (2021) , figure 5, demonstrates that the airfoil generates a significantly larger coefficient of lift (C_L) at elevated angles of attack (AOA). Consequently, the Albatross GOE173 has a significantly elevated drag coefficient (CD) compared to other GOE 174, attributable to its pronounced camber (Muruga et al. 2021).

However, at a negative angle of attack, such as -2^0, it generates significantly less drag compared to those with GOE173 that provide positive lift. Consequently, -2^0 can be regarded as the optimal angle of attack, yielding a positive lift coefficient and significantly reduced drag (Muruga et al. 2021).

2.4. Airfoil

An object's cross-sectional shape that generates an aerodynamic force when traversing a fluid, such as air, is termed an airfoil.

There exist two categories of airfoils, specifically:

- Symmetric and
- Cambered airfoil (Ansari et al. 2022)

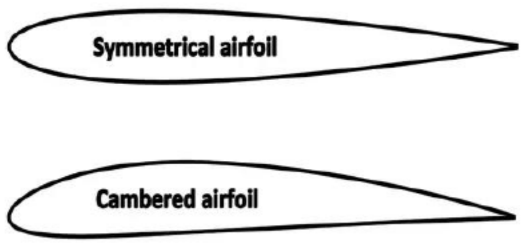

Figure 6: Symmetrical and Cambered Airfoils (Ansari et al. 2022)

As noted by Patel et al. (2014) a symmetric airfoil generates no lift when positioned at a zero-degree angle of attack. In contrast, a cambered airfoil distinguished by its asymmetry above and below the camber line exhibits different aerodynamic behaviour. Figure 6 showed cambered profiles, these profiles have their aerodynamic centre remains fixed at one-quarter of the chord length behind the leading edge, though the lift characteristics differ due to the curvature of the camber line.

Compared to symmetric airfoils, cambered airfoils have a lower stall angle (Ansari Shamsher Ali et al. 2022).

2.5. Airfoil mathematical framework

Uneven distribution of the airflow across an airfoil causes forces to be applied to its surface on figure 7 according to Osei et al. (2020). Dwivedi et al. n.d. shows equation (1) representing the lift force, which is perpendicular to the relative wind flow. When there is a differential in air pressure between an airfoil's upper and lower surface sections, this force is produced (Mamadaminov 2013). The correlation between the actual airflow velocity at the airfoil of a conventional wind turbine blade section is articulated in equation (1) page 23 according to Osei et al. (2020) and Patel et al. (2014).

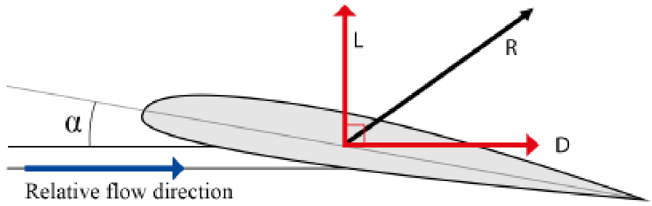

Figure 7: The forces acting on the airfoil (Lundberg et al. 2015)

$$L = C_l \frac{1}{2} \rho U^2 cl \quad (1)$$

(Dwivedi & Vashishta 2023)demonstrated on equation (2) how drag force is produced by uneven pressure on an airfoil's surfaces when it is pointing forward, away from the incoming flow, and parallel to the flow direct.

$$D = C_d \frac{1}{2} \rho U^2 cl \quad (2)$$

An airfoil differs from other types of structures due to the ratio of the lift and drag forces that cause the system to produce thrust and torque (Mamadaminov 2013). The lift force, a positive force, must be increased and the drag force, a negative force, must be as much smaller in order to attain a high lift to drag ratio.

Equation (3) uses the lift-to-drag ratio as an expression.

$$\frac{L}{D} = \frac{C_l(\frac{1}{2})\rho U^2 cl}{C_d(\frac{1}{2})\rho U^2 cl} = \frac{C_l}{C_d} \quad (3)$$

Reynolds number, which is shown as a function of an airfoil's performance characteristics, has a considerable impact on the values of an airfoil's drag and lift characteristics.

Osei et al. (2020) used mathematics to express the Re for the airflow over the airfoil as an equation (4).

$$Re = \frac{\rho U c}{\mu} = \frac{Uc}{v} \quad (4)$$

2.6. Airfoil aerodynamics performance

2.6.1. Lift coefficient (Cl)

A solid item moving through a fluid creates lift, a mechanical aerodynamic force that resists the weight of the airborne entity and sustained its elevation. It acts through the flying object's centre of pressure and is a vector quantity as mentioned by Rao Chakravarthy et al. The differential in velocity between the flying object and the fluid surrounding it produces the lift. Whether the fluid is traversing across an object or the thing is traveling through the fluid makes no difference. Coefficient of Lift (CL), a nondimensional coefficient, is typically used to assess lift by Sharma (2016).
Faraihan Zulkefli et al. (2016) shows the values of lift coefficient from experimental method and compared it with values retrieved from numerical analysis and Xfoil database as seen on figure 8.

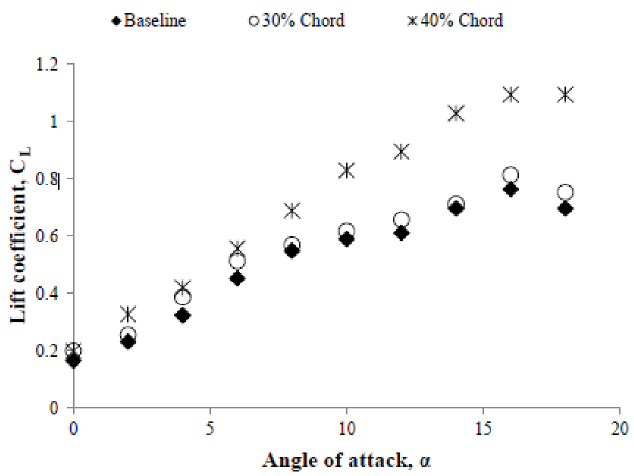

Figure 8: Reynolds number of 15 000, Lift coefficient against AoA graph (Faraihan Zulkefli et al. 2016)

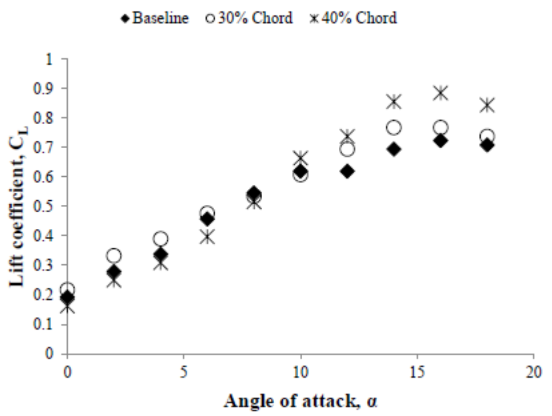

Figure 9: Reynolds number of 35 000, Lift coefficient against AoA graph (Faraihan Zulkefli et al. 2016)

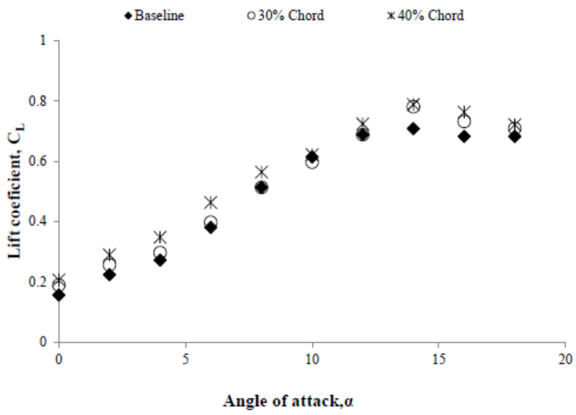

Figure 10: Lift coefficient against angle of attack at Reynolds number = 50 000 (Faraihan Zulkefli et al. 2016)

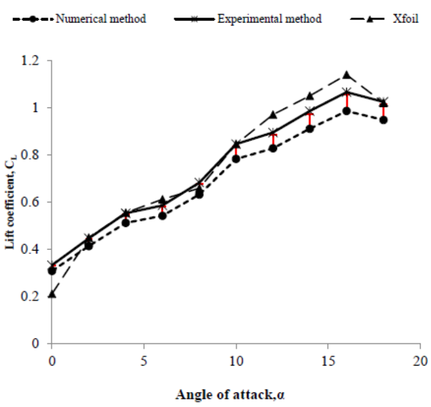

Figure 11: Comparison between numerical method and XFoil database (Faraihan Zulkefli et al. 2016)

Figures 9-11 plot and show the lift coefficient values from the experiment, the numerical analysis, and the XFoil database. It was observed that the lift coefficient values for each of the three scenarios on figure 12 climbed gradually until they reached a stall at a 16^0 angle. While the figures for XFoil had been 1% higher, the values from the numerical analysis were almost 7% lower than those from the experiment. Consequently, the greater lift coefficient from the experiment demonstrated the efficacy of the blower application in the actual situation, and the numerical analysis confirmed the experimental result. The findings also showed that the wind tunnel environment affected a number of variables, including temperature, density, and pressure as demonstrated by Faraihan et al. (2016).

Figure 12 illustrates that the lift and drag coefficients errors for the last four grids were maintained under 1% throughout angles of attack ranging from 0 to 100, with a 20 interval (Zhu et al. 2023).

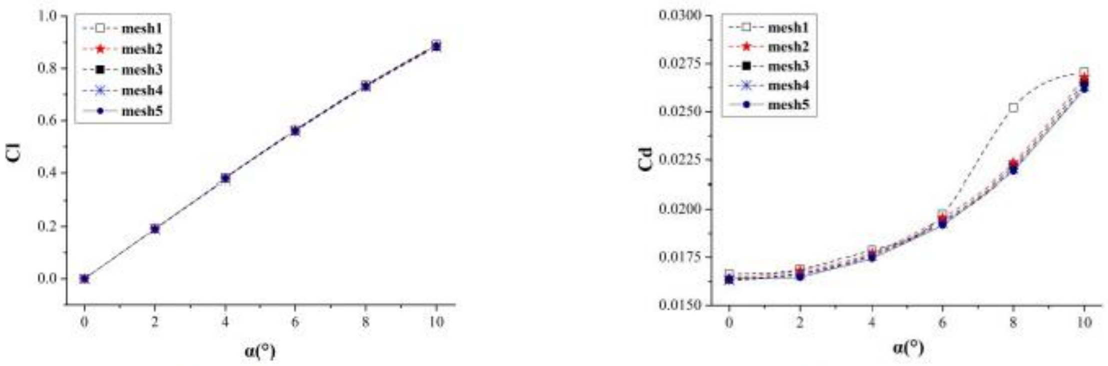

(a) Lift coefficients. (b) Drag coefficients.

Figure 12: Coefficients of lift and drag for evidence of independence (Zhu et al. 2023)

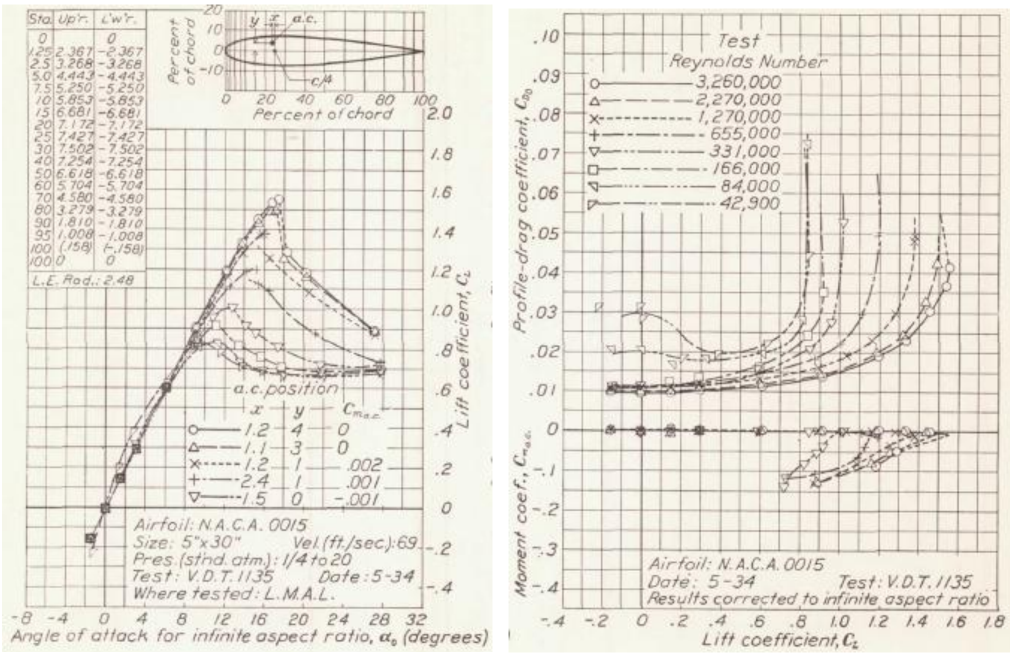

Figure 13: Coefficients of lift, drag against AoA of NACA0015 and NACA0018 **(Jacobs Eastman et al. 1937)**

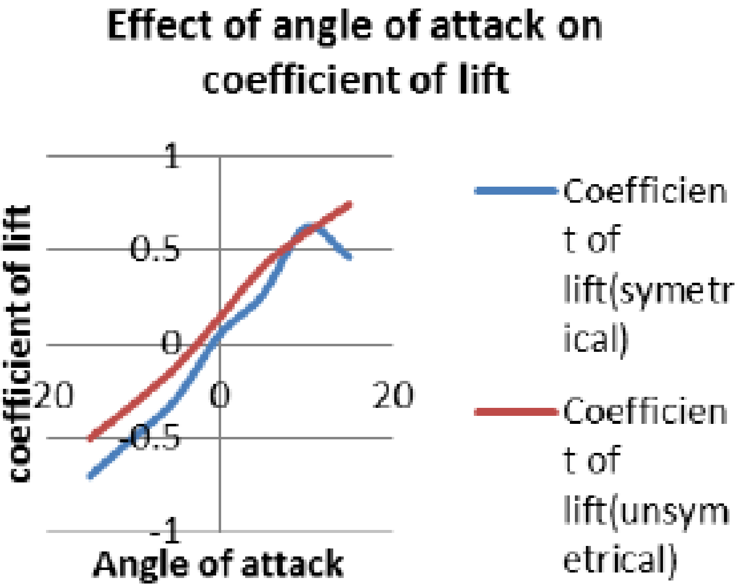

Figure 14: Impact of AoA on lift coefficient (Sreedevi KNV et al. 2020)

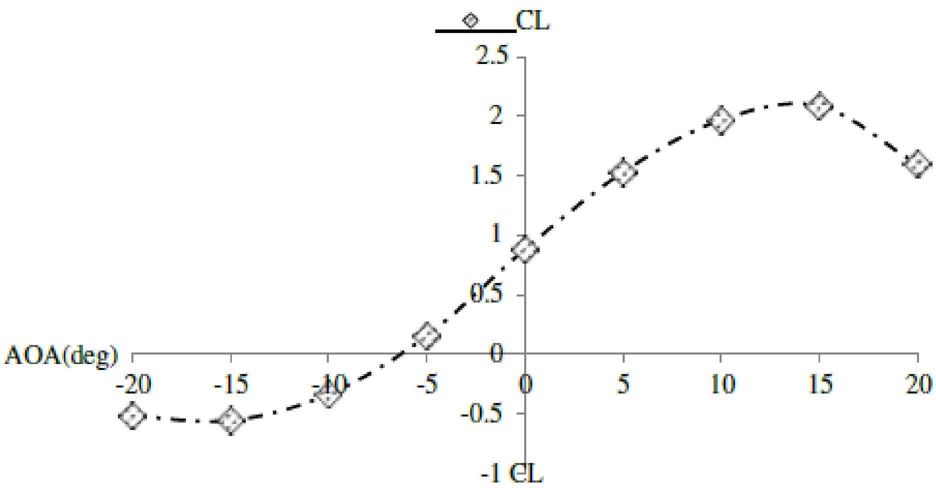

Figure 15: Numerical solution of NACA 6212 lift coefficient diagram against angle of attack (Akbari 2021)

The impact of AOA on the aerodynamic forces of drag and coefficient of lift is displayed in graphs on figure 14 (Sreedevi KNV et al. 2020) and 15 (Akbari 2021). Lift forces from both symmetrical and unsymmetrical airfoils grow as the angle of attack rises from -15^0 to 15^0, reaching a maximum value at 15^0.

2.6.2. Drag coefficient (Cd)

In a fluid medium, the drag force operates in the direction opposing to that of the object that is moving. It lessens an object's lift in addition to opposing its motion in a fluid medium (Rao et al. 2018). The fluid's density, the size of an object and configuration, the fluid's compressibility and viscosity, the fluid's velocity, and the fluid around a moving object all affect drag. The coefficient of drag, a dimensionless metric, evaluates the resistance of a moving item in a fluid (Sharma 2016). As the angle of attack rises, drag force decreases as discussed by (Sreedevi KNV et al. 2020) and shown on figure 16.

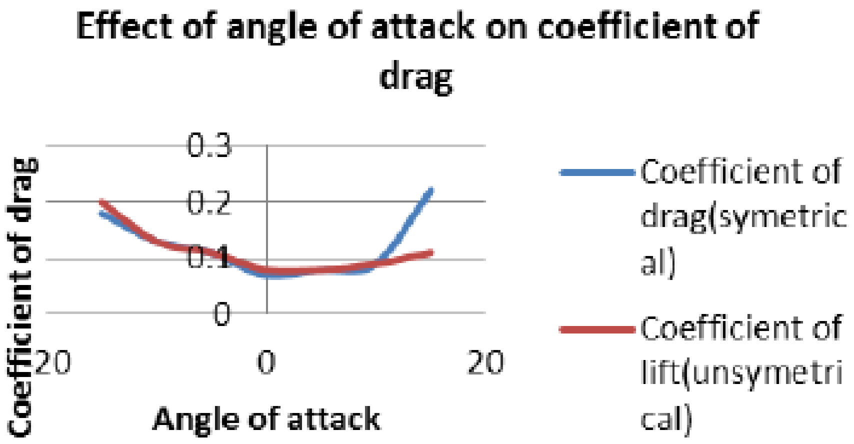

Figure 16: Impact of angle of attack on drag coefficient(Sreedevi KNV et al. 2020)

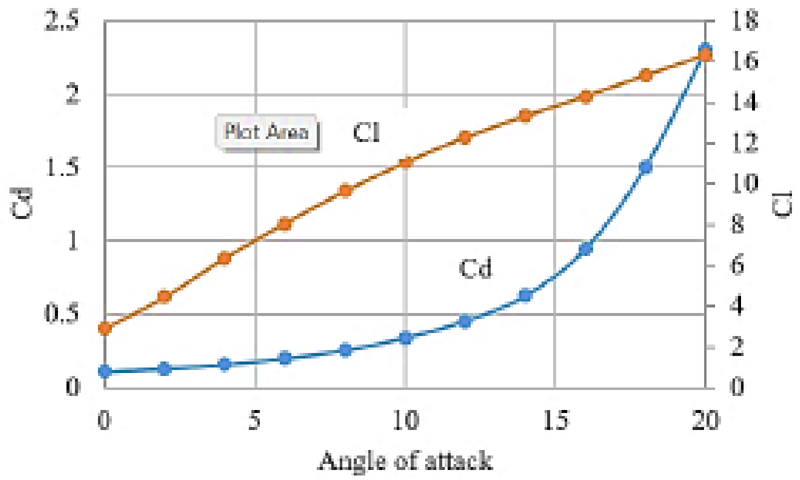

Figure 17: Lift and drag coefficients against AoA (Ghose et al. 2024)

Figure 17 illustrates the variation in the coefficients of drag and lift concerning the angle of attack. It has been observed that an increase in the angle of attack corresponds with an elevation in both CL and CD by Ghose et al. (2024). Nonetheless, the lift coefficient escalation rate diminishes as the angle of attack grows, while the drag coefficient escalates rapidly with a rise in angle of attack shown by Ghose et al. (2024).

2.7. Surface modification's impact on aerodynamic performance

In order to change the aerodynamic qualities, study has examined alterations to the complete geometry of the airfoil surface by Mulligan (2020) Research indicates that skins with corrugations on both sides can generate eddies in the troughs, which efficiently circulation of air akin to tapered airfoils, so delaying stall Mulligan (2020). Figures 18 and 19 illustrate the relationship between drag coefficients and the angles of attack. In lift comparisons, the smooth airfoil generates the most lift, peaking at approximately 12° , but due to its streamlined design, it experiences a rapid decline in lift immediately following detachment (Isyaku Kunya et al. 2024) .

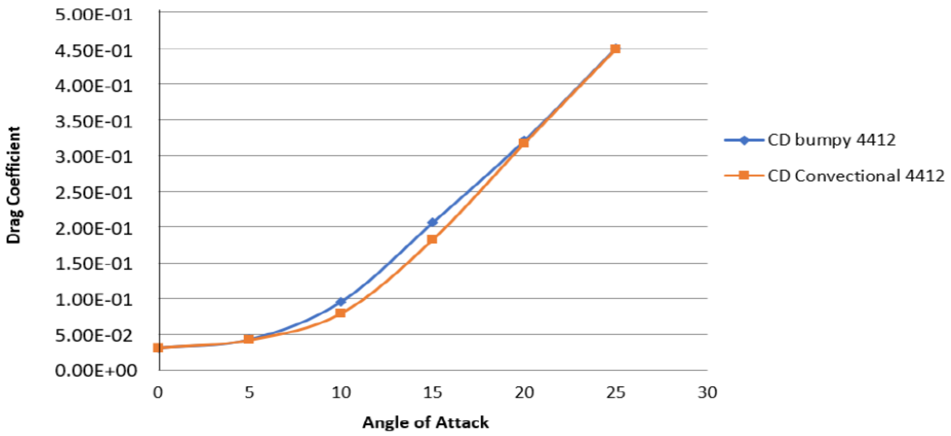

Figure 18: Drag coefficient versus angle of attack (Isyaku Kunya et al. 2024)

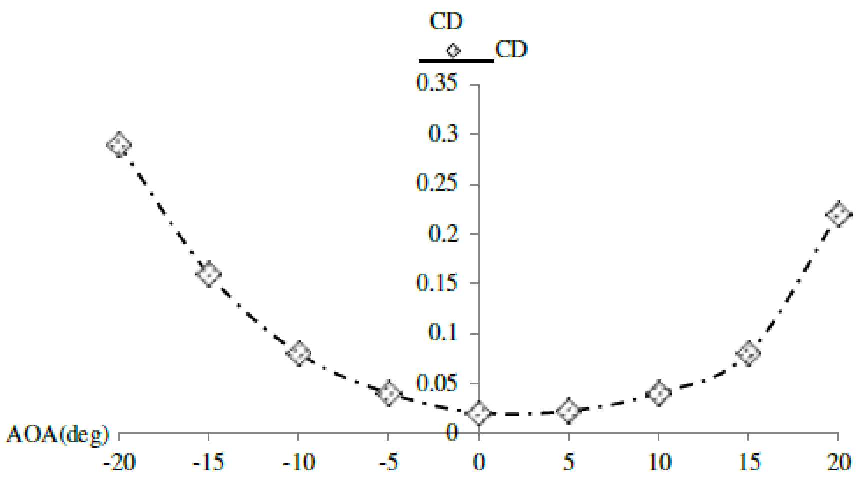

Figure 19: Numerical solution of NACA 6212 drag coefficient diagram against angle of attack (Akbari 2021)

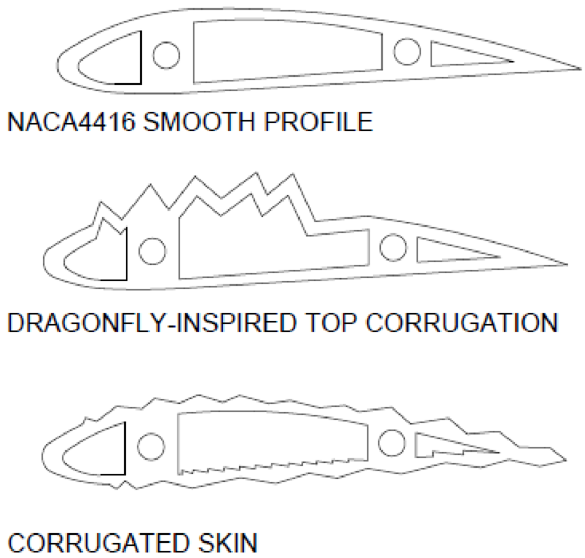

Figure 20: Airfoil Designs, top Corrugated and Corrugated (Mulligan 2020)

The corrugated shapes on figure 20 configurations exhibit a notable enhancement in postponing stall by 4° and demonstrate an extended transition period prior to total boundary layer separation by Mulligan (2020).

On the airfoil surfaces, deeper surface grooves can get rid of laminar separation bubbles. As a result, small wind turbine aerodynamic performance increase as mentioned by Liu et al. (2020). While a shallow groove necessitates a reduced aspect ratio of the recess depth to the channel depth, a deep groove can have a bigger ratio of aspects that helps stabilize the vortex (Liu et al. 2020). The main factor influencing how well airfoil's function is the distance from the baseline boundary layer thickness (Liu et al. 2020) . The most effective ratio of recess depth is between 1.0 and 1.5. The depth of the recess has an impact on the groove aspect of ratio (Liu et al. 2020). To stabilize the vortex, however, a greater aspect ratio (narrower groove) is needed if the groove is deep (Liu et al. 2020). For a ratio of recess depth < 1.2, a narrower groove with a reduced aspect ratio can more effectively contain the vortex (Liu et al. 2020). An arc groove increases wall friction, while a rectangular cross form decreases it, enhances vortex stability, and better limits fluid motion inside the groove, especially for a recess depth ratio of 1.2 to 1.5 (Liu et al. 2020). At the design AOA = 100, optimal airfoil surface grooves boost the lift-to-drag ratio by around fifty percent and increase the small wind turbine power coefficient by 2%.

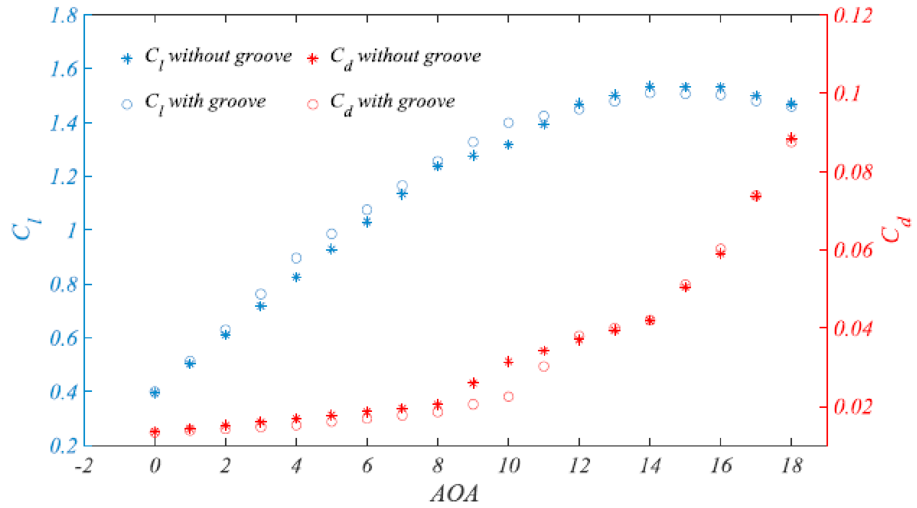

Figure 21: Comparison of the calculated lift and drag coefficients of the NACA4415 with and without surface grooves (Liu et al. 2020)

(Gao, Chen, Li & Yao 2021) examined the aerodynamic efficacy of wind turbines integrated with herringbone groove design. The principal objective of the study was to illustrate a bionic design for wind turbine blades, inspired by the owl's wing airfoil and the herringbone groove pattern of its feathers by Gao et al. (2021).

Numerical modelling was employed to examine how the bionic blade and other blades alter the pressure and flow pattern. The standard model used was NACA4412 with the tip speed ratio of 6, rated speed of 5m/s and rated power of 200W.

According to Xu et al. (2024), the implementation of a corrugated structure results in an average drag increase of 7.19% and a maximum increase of 26.9%. However, it concurrently yields a substantial lift enhancement, with an average rise of 13.04% and a maximum rise of 21.47%.

Figure 22: Prototype Blade (Gao et al. 2021)

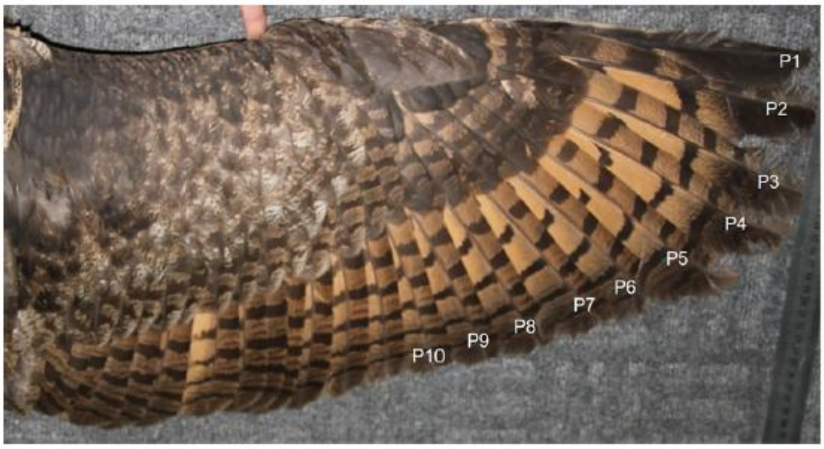

Figure 23: The wing of owl (Gao et al. 2021)

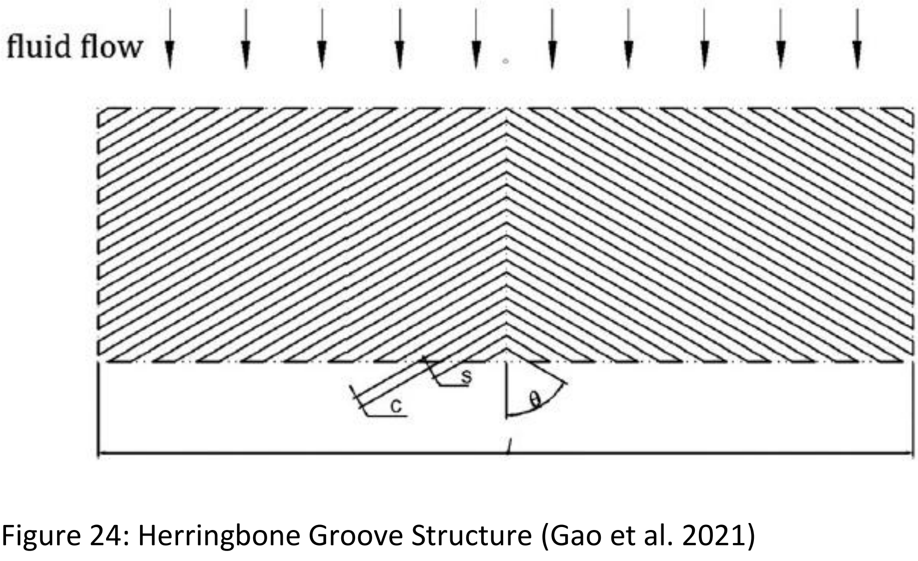

Figure 24: Herringbone Groove Structure (Gao et al. 2021)

According to Gao et al. 2021) the enhancement of the blades' aerodynamic efficiency is the primary factor augmenting the pressure differential between the windward and leeward surfaces of the blade.

The herringbone groove design shown on figures 23-24 and airfoils on the owl wing improve the pressure differential in the blade (Gao et al. 2021). Less pressure is applied to the leeward surface of the blades because of faster flow velocity and larger leading-edge curvature of the blades (Gao et al. 2021). The concave contour of the blade shown on figure 25 is what causes the augmentation of pressure on the aerial surface (Gao et al. 2021). The local strain on the blade surface is decreased by the herringbone groove arrangement (Gao et al. 2021).

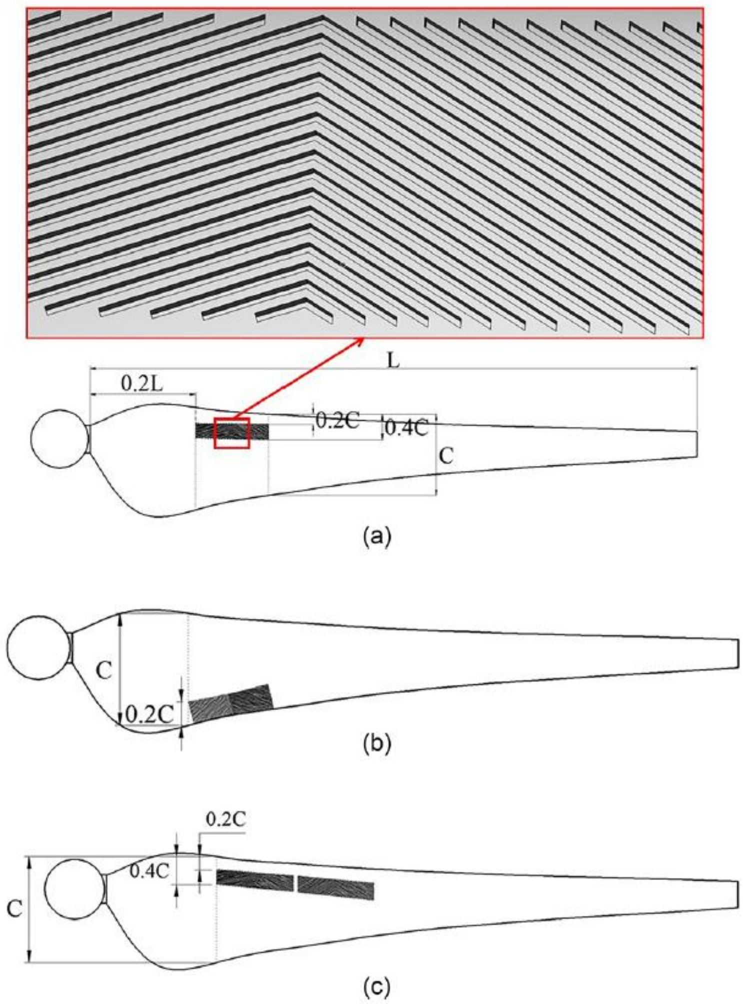

Figure 25: (a) Blade A (b) Blade B and (c) Blade C of the Bionic Coupling

There is a little vortex that causes the reduction of the pressure in the area (Gao et al. 2021). The herringbone structure's pressure in the groove diminishes as a result of the groove's vortex, which causes the pressure coefficient oscillation on the windward blade surface on figure 26 (Gao et al. 2021).

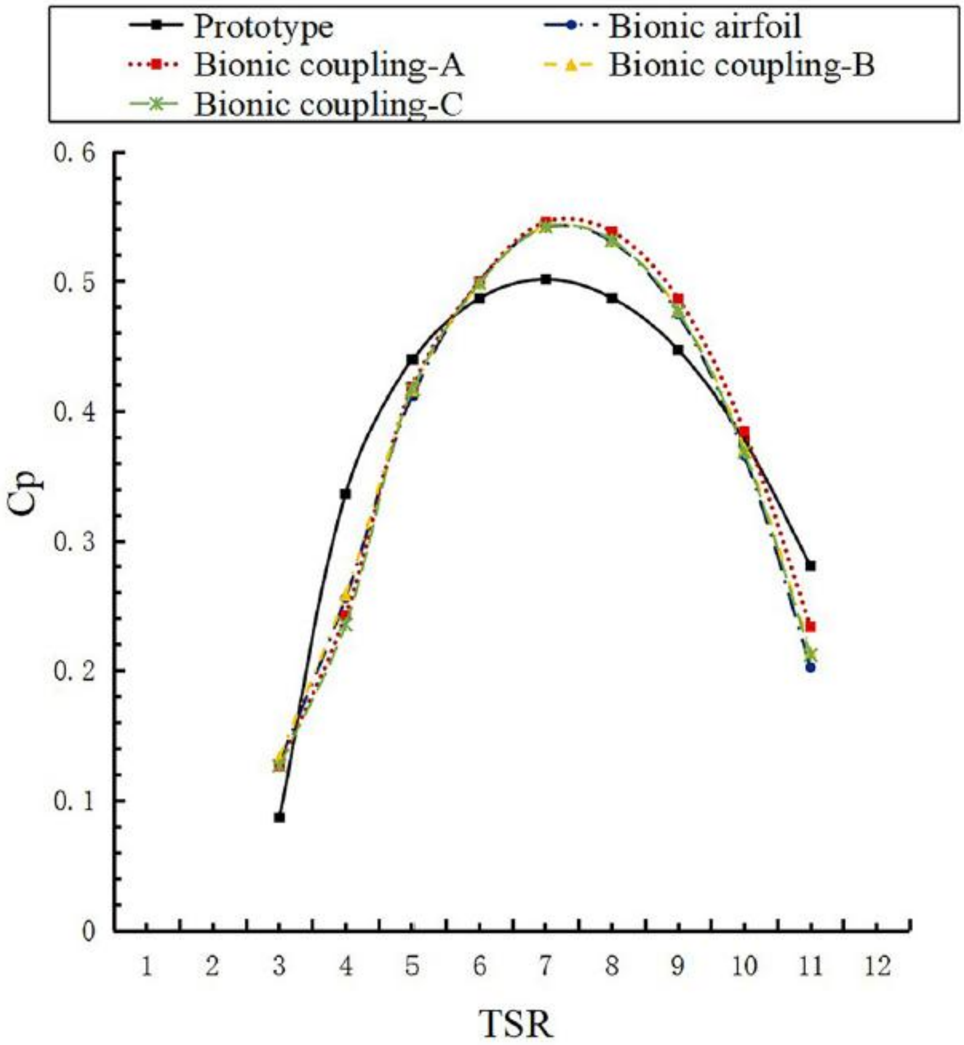

Figure 26: The Wind Turbines' Cp at various TSRs (Gao et al. 2021)

2.8. The low wind speed airfoil

There are several engineering parameters that must be met when choosing an airfoil, but aerodynamic performance and structural strength should be prioritized over electromagnetic interference, acoustic noise generation, and aesthetic appeal (Gray et al. 2021). This selection suggests that a wind turbine that is running in a low wind location should have better aerodynamics than a wind turbine that is operating in a high wind area (Gray et al. 2021).

The lift-to-drag ratio, lift coefficient and Reynolds number all play crucial roles in achieving greater aerodynamics and design performance.

The goal was to construct an airfoil with the best relative thickness possible in order to enhance power output. The results shown on figure 27 are the comparisons of existing airfoil's design against the angle of attack. According to this graph shown on figure 27 was concluded that some airfoil has higher Cl/Cd ratio than others when it comes to different Reynolds numbers that were tested on.

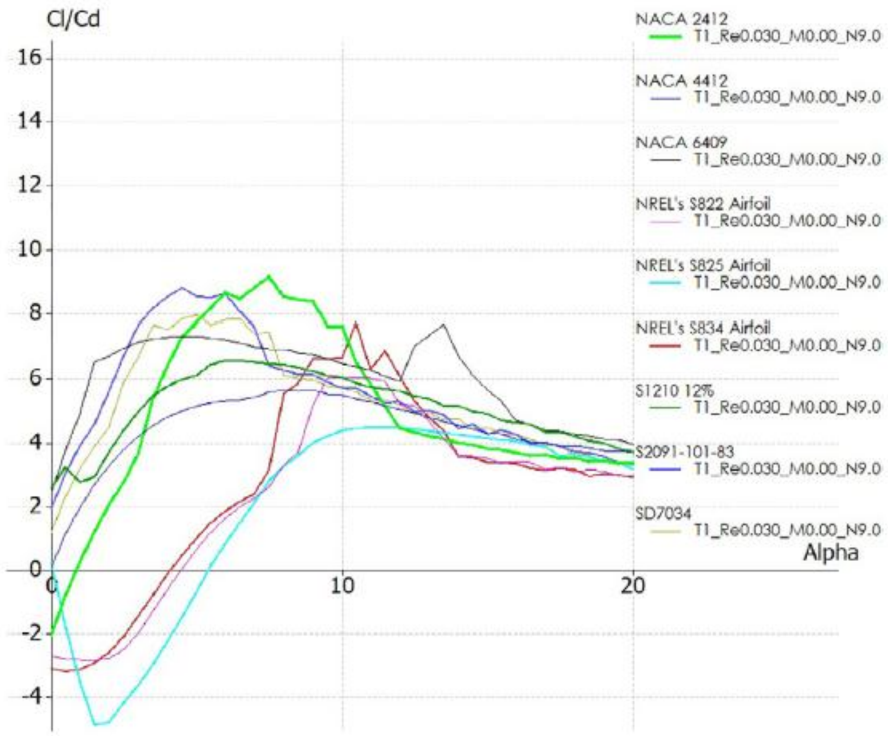

Figure 27: The comparison between lift-to-drag ratio against alpha at $\boldsymbol{Re}\ \mathbf{3.0x10^{4}}$ (Gray et al. 2021)

For researchers attempting to comprehend the mechanical conduct of low Reynolds number fliers, the dragonfly has acted as a model (Khan et al. 2021). According to studies, the front wing of a dragonfly has an incredibly corrugated structure that can be used to create the best bio-inspired micro air vehicles and to take advantage of new technologies to create advanced wing shapes and designs (Khan et al. 2021). A corrugated wing also provides more lift and less drag, according to earlier computational research. The dragonfly wing bends and twists a lot when flying, changing how the structure responds to loading circumstances and how aerodynamics behave (Khan et al. 2021). Figures 28-29 shows the geometry that was used, which was drawn from the sub-costa region of the wing of the dragonfly, which makes up 40% of the forewing's chordwise total span(Zhang et al. 2025). Several corrugated structures on the dragonfly's wing cross-section in the middle of its span improve performance (Khan & Padhy 2021).

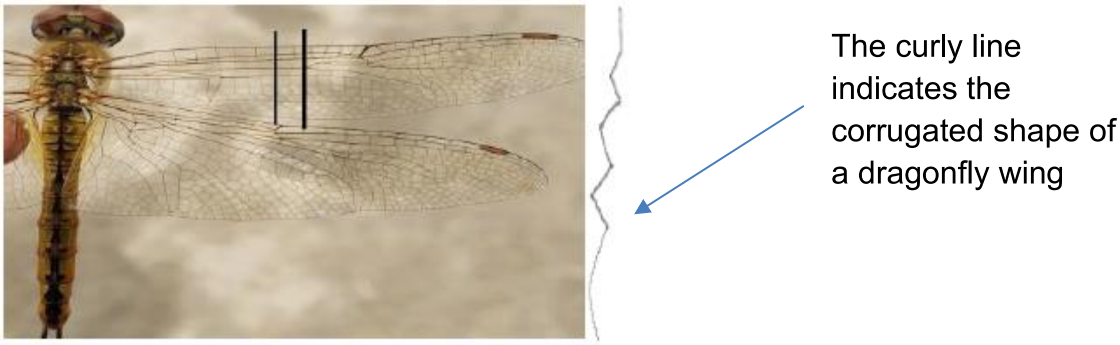

Figure 28: Dragonfly wing shown as pleated corrugate airfoil (Khan et al. 2020)

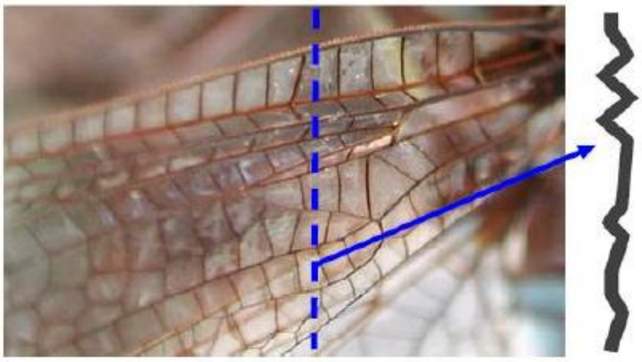

Figure 29: The midsection of the fore wing's cross-section (Khan et al. 2020)

Figure 30 shows the stiff 2D corrugated shape and the standard airfoil NACA 0015's CATIA V5 model (Zhang et al. 2025; Prasad et al. 2018)

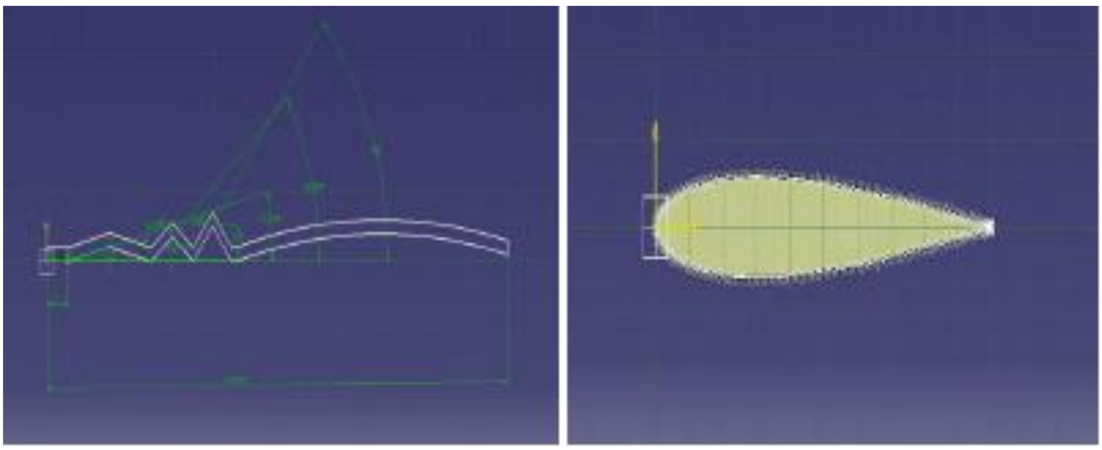

Figure 30: Pleated corrugated airfoil and NACA 0015 (Iqbal et al. 2025)

The chord measures 110 mm in length and is 4 mm thick, and the span is regarded as a single unit. In other studies, it has demonstrated the significance of the chordwise fluctuation in the cross-sectional area (Khan & Padhy 2021).

The purpose of the final remarks is to clarify the performance parameters of the standard NACA0012 airfoil and the bio-inspired corrugated dragonfly wing's cross-section at two distinct Reynolds numbers, 75000 and 115000 (Khan & Padhy 2021).

2.9. Methodologies used by various researchers

In order to provide relevant findings, the methodological technique is described by Ayon Sarkar et al. (2025) as follows: generating the geometry, defining the domain, creating the mesh, setting up the solver, conducting the simulation, and post-processing the results as needed and vital.

2.10. Types of computational geometry

There are few types of computational domains that can be used in ANSYS Design Modeler, some are C-type and rectangular type. Figure 31 depicts the C-type, including a circular arc on the left side that serves as a velocity entrance, while the vertical line on the right-side functions as the pressure exit.

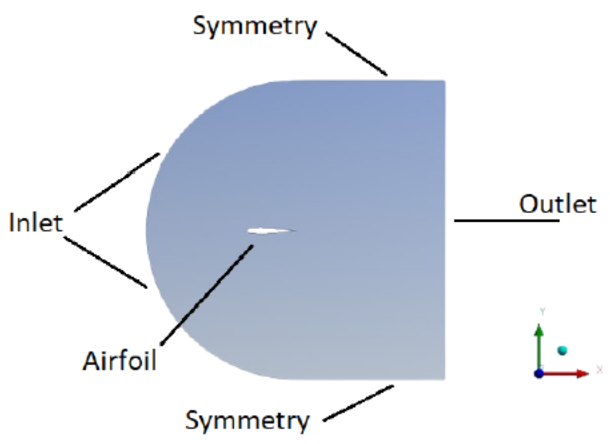

Figure 31: Computational C-type Domain or (Iqbal et al. 2025)

According to the CFD simulation results, smooth airfoils perform substantially worse than pleated corrugated profiles at all angles of attack. The corrugated airfoil has a higher maximum gliding ratio and a higher lift to drag ratio between 4^0 and 8^0 than the standard airfoil type being studied here (Khan et al. 2021). The rectangular computational domain or enclosure is also used in the ANSYS Design Modeler on figure 32 below shows the rectangular enclosure (Iqbal et al. 2025).

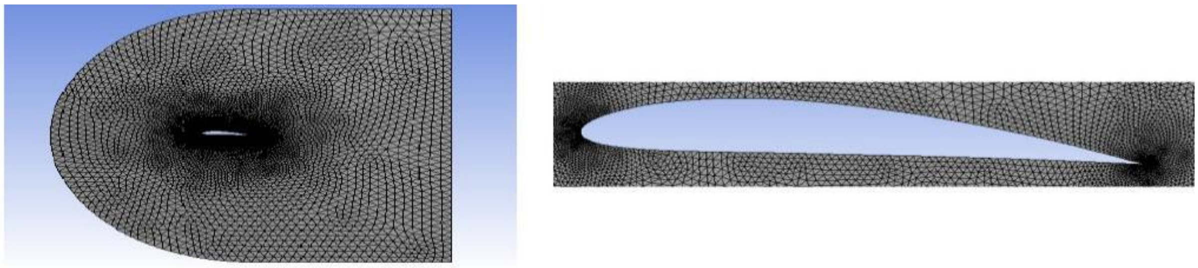

Figure 32: Mesh surrounding the airfoil with a zoomed view (Iqbal et al. 2025)

Performance of the airfoil is studied in detail by modeling numerous angle of attack to highlight its influence on the lift and drag coefficient as well as other important flow characteristics. Also, another simulation is conducted using another airfoil configuration like NACA 4412 to investigate the impact of airfoil geometry on flow behavior by Iqbal et al. (2025). This means that a new mesh with a fine enough resolution should be created to obtain accurate results and to correctly represent the geometrical features and the flow properties of the airfoil as illustrated on figure 32. Finally, the examination of the resampled data offers significant information on the performance and the aerodynamic characteristics of the airfoil.

2.11. Velocity contours around the airfoil

The velocity contour, according to Ansari et al. n.d.., is a contour that provides us with specific details regarding the fluid flow above and below the airfoil. It also illustrates how velocity changes at different angles of attack. Even when the angle of attack is at zero, the cambered airfoil's shape is so distinct that the fluid flow over its surface is relatively higher than at its bottom surface. At the exact leading edge, however, when velocity is zero and the position can be summed up as a stagnation point, the air regularly strikes the surface. In actuality, the stagnation point is also influenced by the angle of assault. According to (Ansari et al. 2022), the stagnation point seems to move away from the leading edge on the upper surface for different negative angles of attack and away from the leading edge on the lower surface for different positive angles of attack.

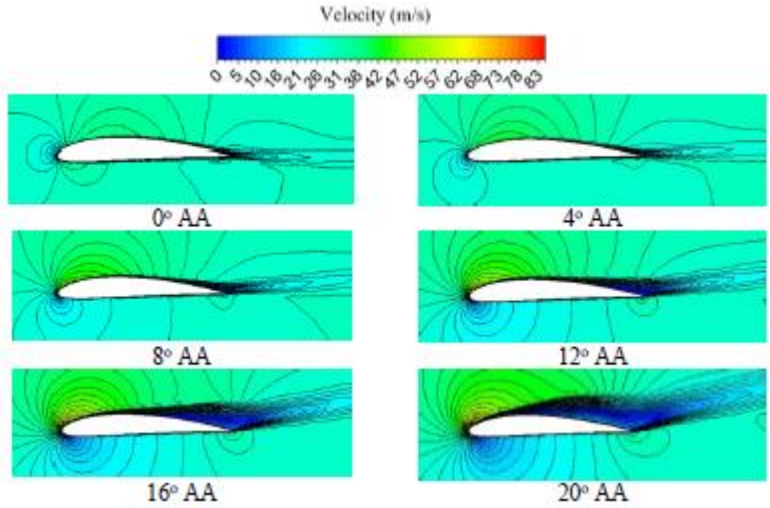

Figure 33: Velocity Contour Flow with angle of attack from 0^0 to 20^0 (Ghose et al. 2024)

Furthermore, figure 33 illustrates that when the angle of attack rises, the airflow velocity around the lower surface of the airfoil diminishes. Consequently, Bernoulli's principle is validated in this instance by the pressure-velocity relationship. With an increase in the angle of attack, boundary layer separation results in a more pronounced backflow towards the tail, as illustrated in Figure 34. This elevates drag resistance as the angle of attack rises.

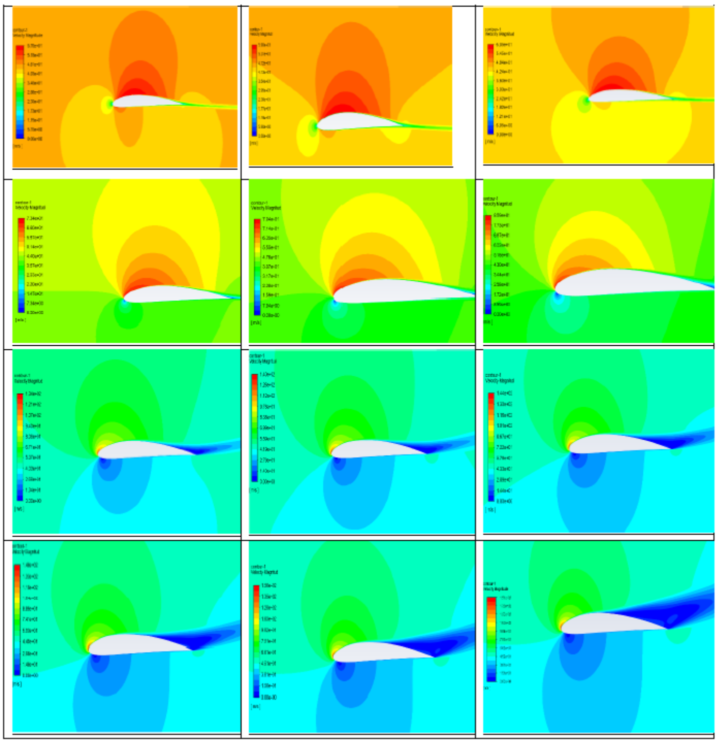

Figure 34: Velocity Contour Flow (0^0-20^0)(Ansari et al. 2022)

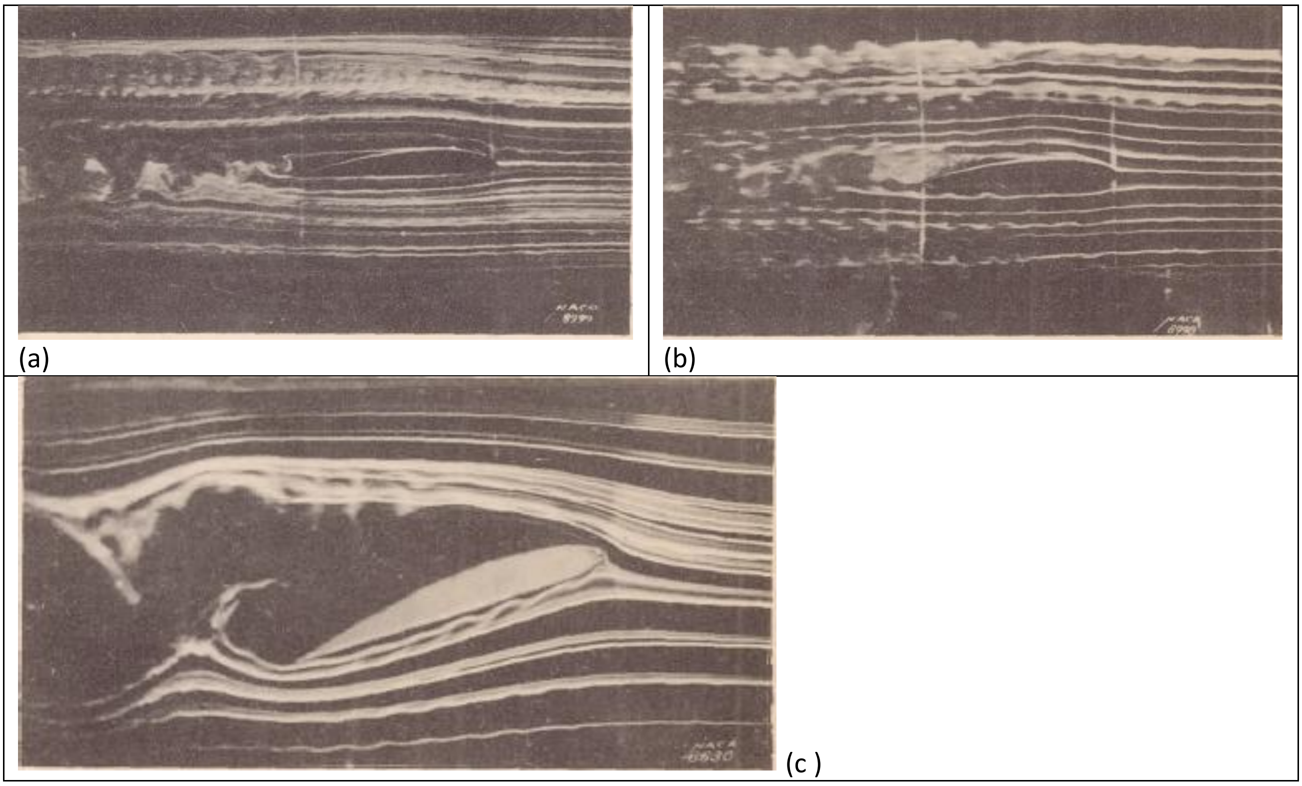

Figure 35: Separation occurring on an airfoil in a smoke tunnel at (a) a low angle of attack, (b) a decreased angle of attack but with an elevated Reynolds Number, (c) at an elevated angle of attack

Figures 35 (a), (b), and (c) illustrate the position and characteristics of the laminar separation on a cambered airfoil, as evidenced by three photographs captured in the smoke tunnel. The third image depicts laminar separation occurring immediately beneath the nose at elevated angles of attack, whereas the preceding two photos exhibit pronounced separation even at a zero angle of attack. Consequently, it is evident that if the Reynolds Number is insufficient to induce turbulence at that site, the separation of the laminar boundary layer will invariably occur near the nose at any relatively high lift coefficient (Jacobs Eastman et al. 1937).

A comparison of figures 33 and 34 makes the impact quite evident. Turbulence is shown developing at a "transition point" along the separated boundary layer posterior to the laminar separation point in Figure 35, which corresponds to an elevated Reynolds Number. The transition point is a variable and large region where the laminar layer progressively evolves into the fully developed turbulent layer (Jacobs Eastman et al. 1937). The transition area advances toward the separation point as the Reynolds number increases (Jacobs Eastman et al. 1937). Turbulence creation leads to an increase in the thickness of the boundary layer separating stagnant air from the overlying flow, until turbulent mixing nearly reaches the airfoil surface (Jacobs Eastman et al. 1937)

2.12. Lift to drag ratio (Cl/Cd) or Aerodynamics results

The most desirable aspect of any design is a higher value for this ratio. The drag-to-lift ratio can be raised by either raising or lowering the lift coefficient; however, in the case of an aircraft design, the weight of the aircraft directly affects the lift, while the aerodynamic design of the aircraft and its wings determine the drag (Sharma 2016)

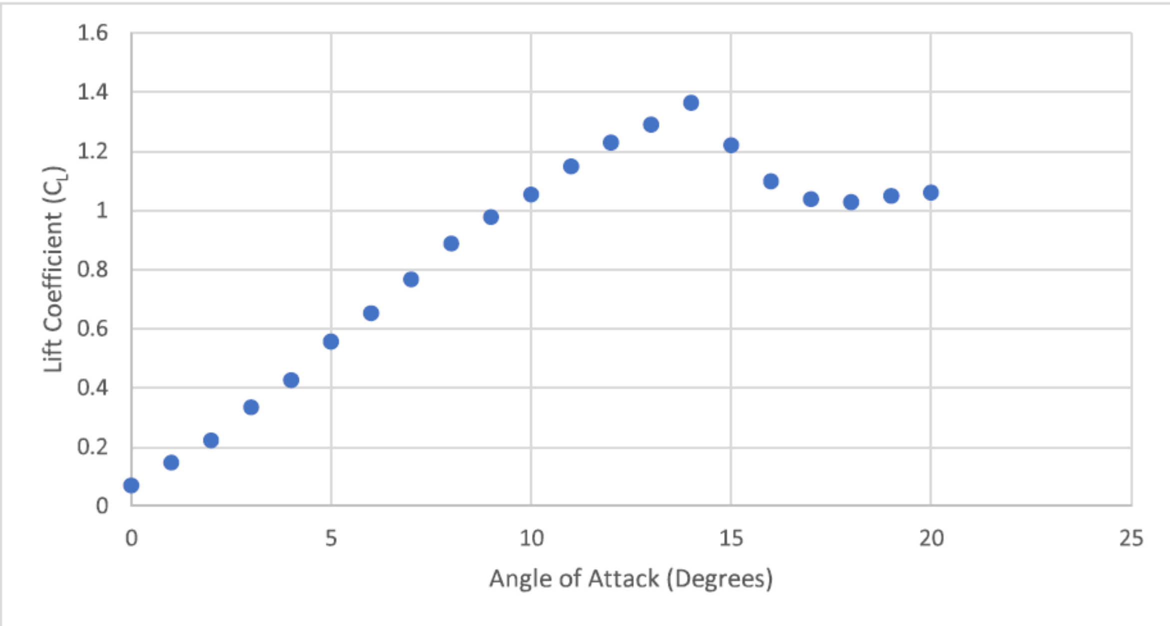

Figure 36: Lift Coefficient values at various angles of attack (Khalid 2022)

Figure 36 shows a calculated lift coefficient at an angle of attack ranging from 0^0 to 20^0(Khalid 2022). According to the graph, CL increases as the angle of attack increases. But as the angle of attack increases further after 14^0, the CL falls (Khalid 2022). The fluid separates because the high-pressure gradient causes pressure forces to overcome the fluid's inertial forces. This fluid separation causes the CL to decrease as the AoA rises (Khalid 2022).

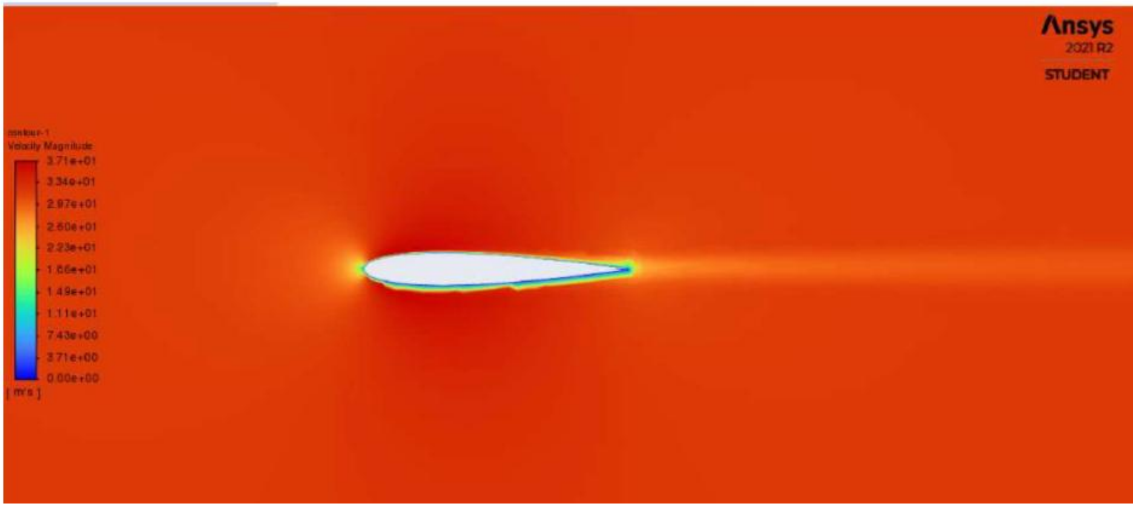

Figure 37: Velocity Contours at 0^0 Angle of Attack (Khalid 2022)

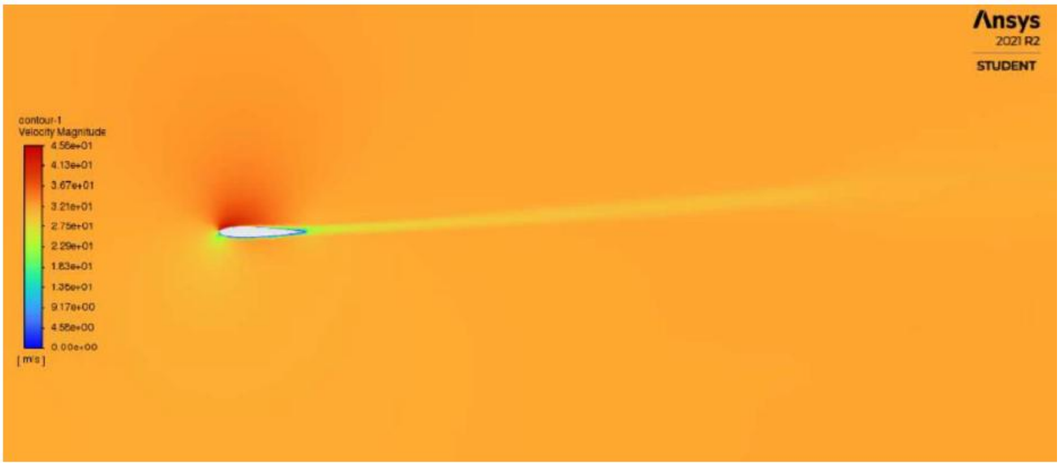

Figure 38: The Contours of velocity at 5^0 AoA (Khalid 2022)

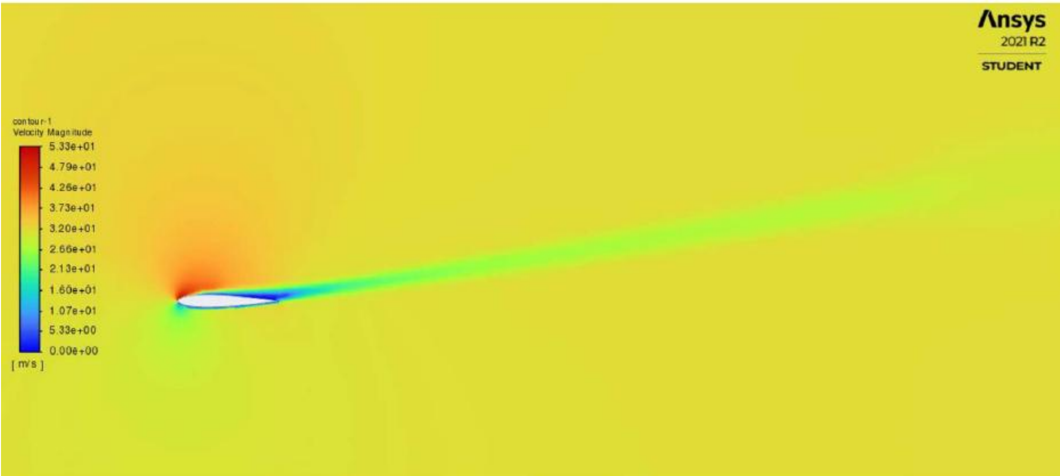

Figure 39: The Contours of velocity at 10^0 Angle of Attack (Khalid 2022)

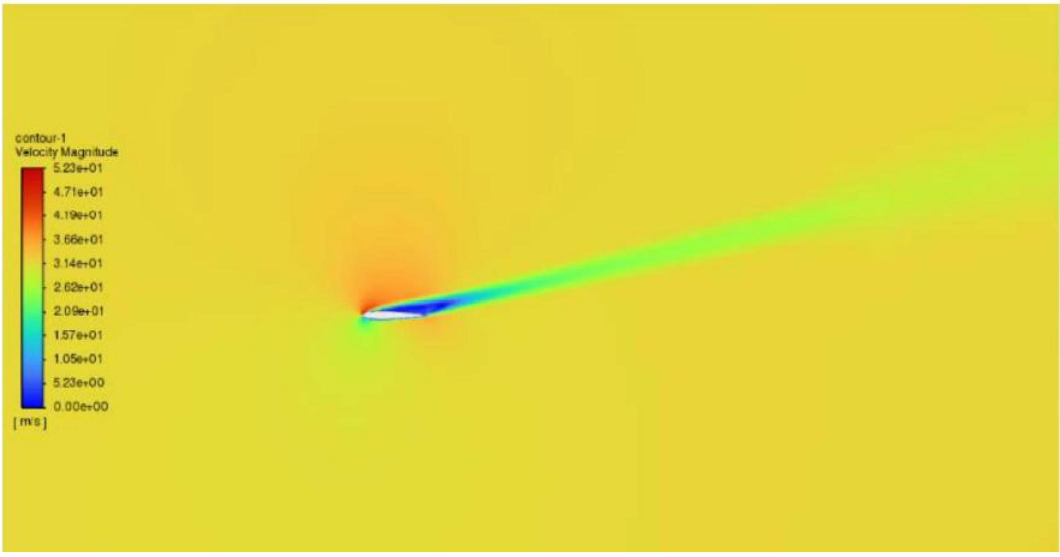

Figure 40: The Contours of velocity at 15^0 Angle of Attack (Khalid 2022)

Figure 41: The Contours of velocity at 20^0 Angle of Attack (Khalid 2022)

Figures 37 to 41 depict the velocity magnitude contours generated from CFD simulations at different angles of attack. The stagnation point is located near the leading edge, resulting in a velocity of zero.

Figures 42 to 46 illustrate the pressure magnitude contours generated by CFD simulations at various angles of attack. According to the Bernoulli principle, pressure decreases at elevated velocities. Similarly, more pressure at the bottom pushes the shape upward creating lift, while lower pressure in the upper part is due to increasing velocity.

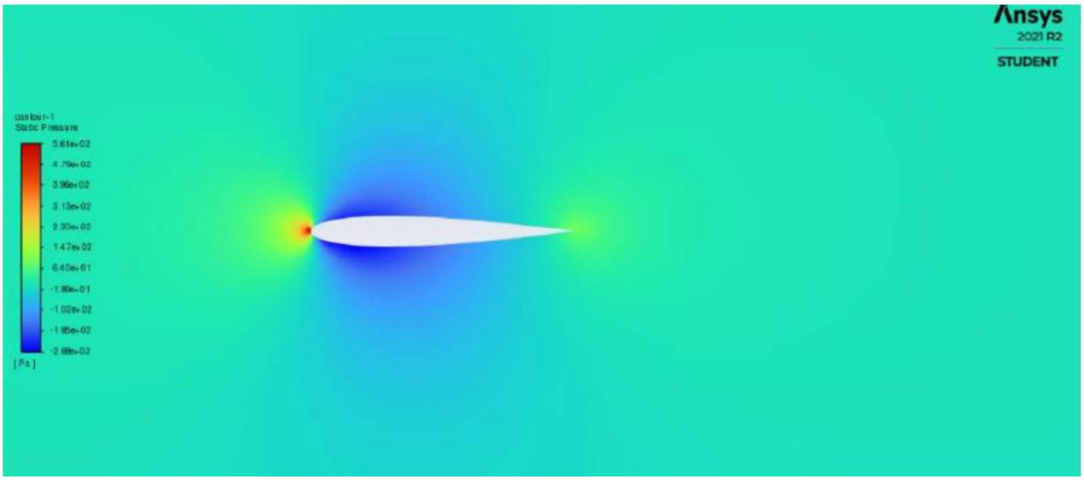

Figure 42: The Contours of Pressure at 0^0 Angle of Attack (Khalid 2022)

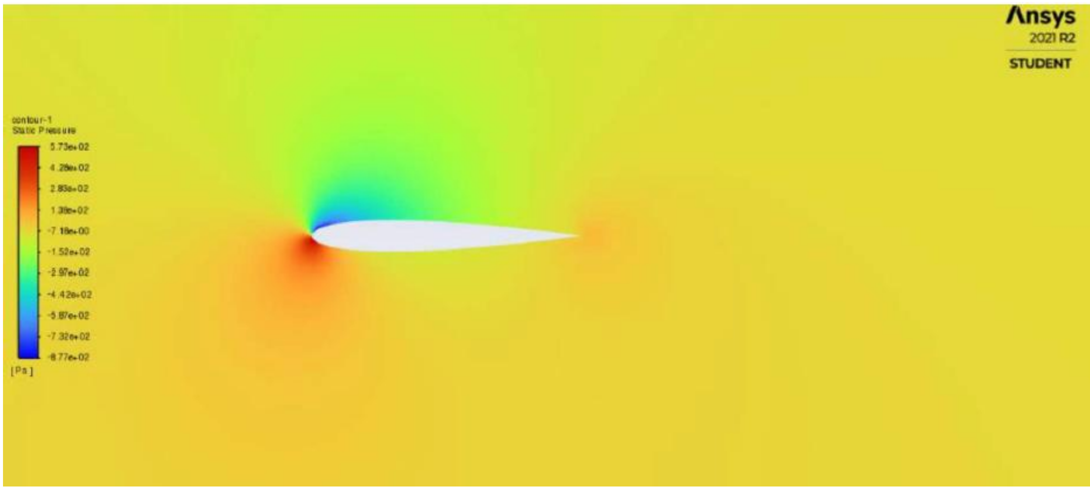

Figure 43: The Contours of Pressure at 5^0 Angle of Attack (Khalid 2022)

Figure 44: The Contours of Pressure at 10^0 Angle of Attack (Khalid 2022)

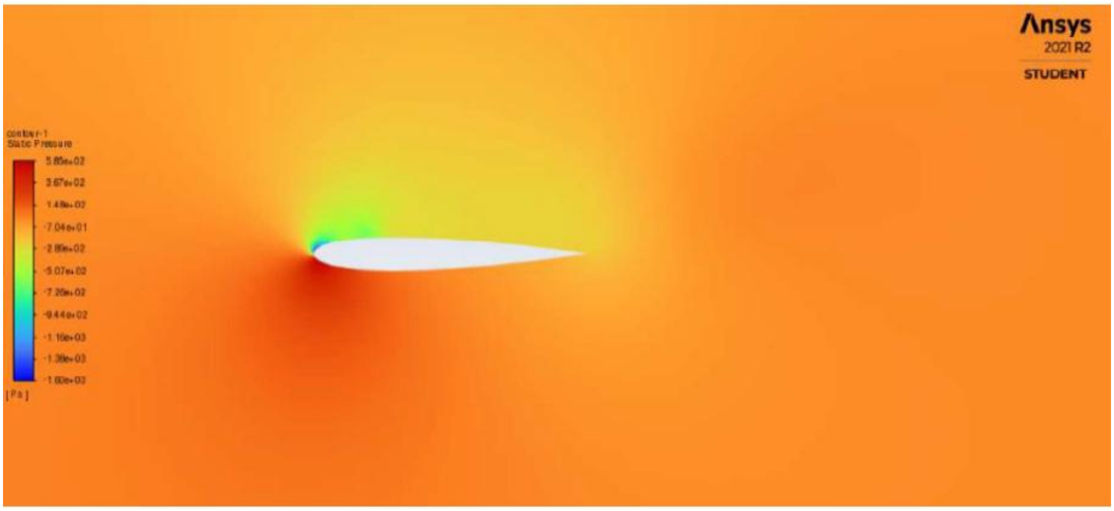

Figure 45: The Contours of Pressure at 15^0 Angle of Attack (Khalid 2022)

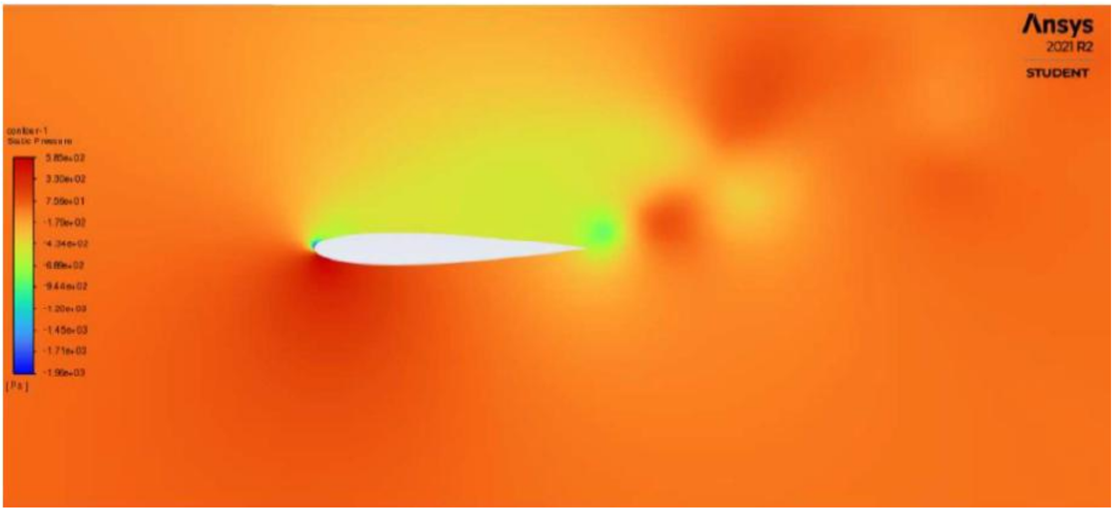

Figure 46: The Contours of Pressure at 20^0 Angle of Attack (Khalid 2022)

The aerodynamic performance of the NACA0012 airfoil was analyzed using ANSYS Fluent CFD software at various angles of attack from 0^0 to 20^0, with a constant velocity of 32 m/s. The airflow around the airfoil was illustrated by pressure and velocity contours. CL was evaluated from all conceivable attack vectors utilizing Fluent (Khalid 2022). The graph indicates that the lift coefficient (CL) grows with the angle of attack until flow separation occurs, after which it declines as the angle of attack continues to rise. The results were validated by comparing them with the literature (Khalid 2022).

2.13. The impact of inlet velocities on the aerodynamic coefficients

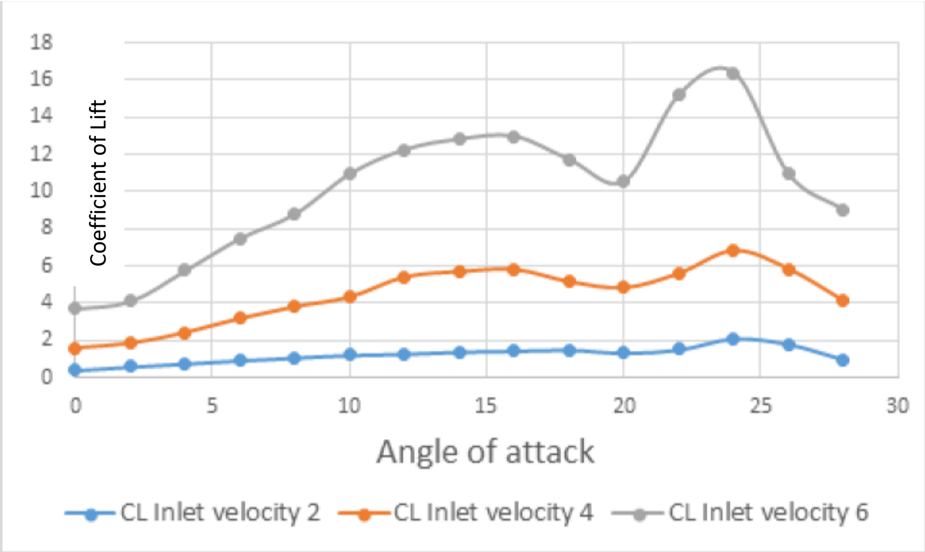

Figure 47: Coefficient of Lift vs Angle of Attack against Inlet Velocities of 2,4 and 6m/s (Iqbal et al. 2025)

The impact of inlet velocities on aerodynamic coefficients and its ratios is something that has shown patterns that one can be able to observe. The coefficient of lift (CL) is presented relative to angle of attack (α) at an input velocity of 2 m/s, 4 m/s, and 6 m/s in Figure 47 (Iqbal et al. 2025) . From 0 to 24^0, we see that the CL rises linearly from 0 to 2.1 in relation to α. Plotting the CL against α is done with an entrance velocity of 4 m/s (Iqbal et al. 2025). The CL rises to 5.8 in opposition to α=24^0.A further increase in α causes CL to decrease. Plotting the CL against α is done at an entrance velocity of 6 m/s (Iqbal et al. 2025). It can be noted that the CL rises linearly from 0 to 16.3 in relation to α from 0^0 to 24^0.

Figure 48 shows that the CD rises marginally from 0^0 to 14^0 in relation to the α. The CD curve's slope then rapidly increases and continues to do so until it reaches 24^0 α (Iqbal et al. 2025). The curve reduces (i.e., the slope becomes constant) after α=24^0, and the CD continues to rise linearly for the remaining values of α. At α=24^0, the CD achieves a value of 2.7. A pattern like this may be seen in the other graphs (Iqbal et al. 2025).

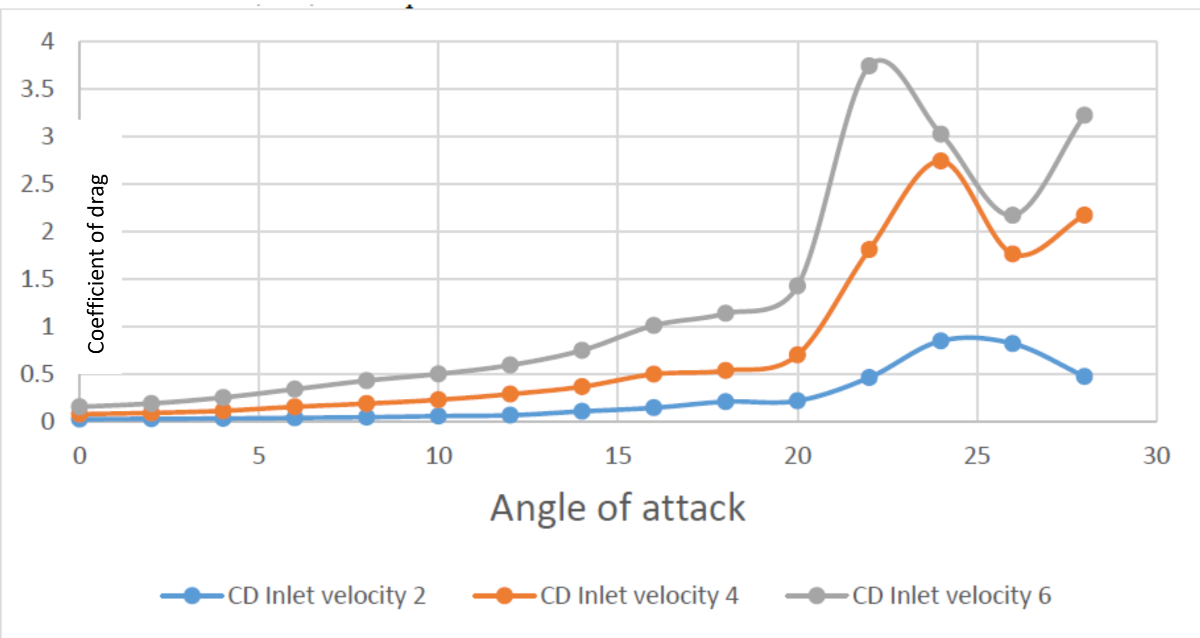

Figure 48: Coefficient of drag vs Angle of Attack against Inlet Velocities (Iqbal et al. 2025).

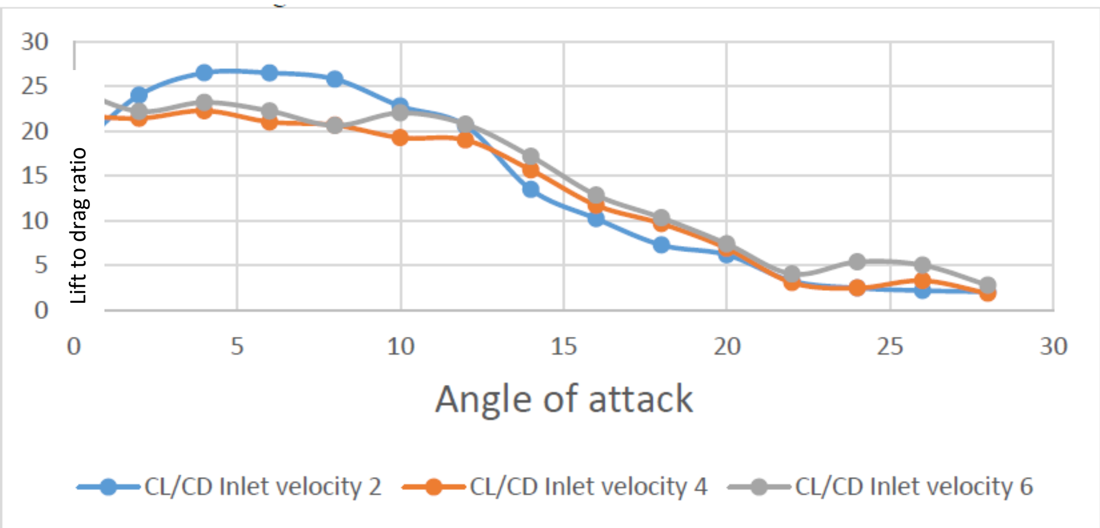

Figure 49: Cl/Cd vs AoA for Inlet Velocities of 2m/s, 4m/s and 6m/s (Iqbal et al. 2025).

The correlation between the aerodynamic forces of lift and drag is denoted by the lift-to-drag ratio which is utilized to evaluate an aerodynamic performance. The term "lift-to-drag ratio"is employed by geodynamicists to quantify this relationship. An object with a high lift-to-drag (L/D) ratio exhibits substantial lift and minimal drag. At α=4^0 in Figure 49 shows the ratio CL/CD increases rapidly and reaches a maximum of 26.4877. The CL/CD curve declines after α=4^0 due to a significant increase in CD and a decrease in CL. Consequently, for any velocity, the maxima of the CL/CD curves occur at α=4^0. The CL/CD curve levels off and demonstrates asymptotic behavior after α=22^0. The analysis indicates that the airfoil achieves optimal performance at α=4^0. A comparable trend is evident in the other graphs (Iqbal et al. 2025).

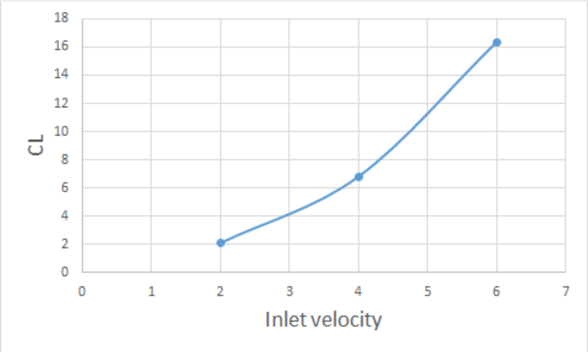

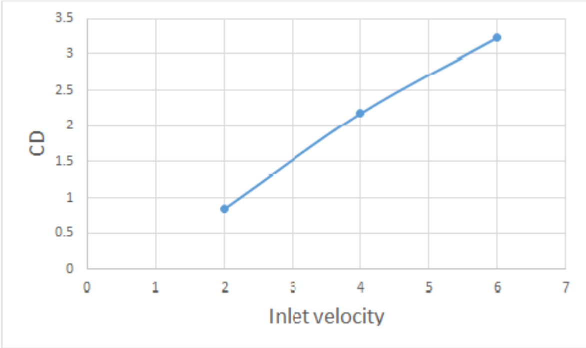

Figure 50: (a) Lift coefficient (Cl) vs inlet velocity at an angle of attack (AoA) of 40^0 and (b) Drag coefficient (Cd) versus inlet velocity at an AoA of 4^0 (Iqbal et al. 2025).

The CL and CD are shown against inlet velocity at α=4^0 in Figs. 50a) and (b). This parameter \alpha=40 is critical for the CL/CD curve. Both figures exhibit a parabolic shape, i.e. curves (CL and Cd) do grow and do so at a fast rate as mentioned by Iqbal et al. (2025).

2.14. The turbulence models

The k-ω Shear Stress Transport (SST) model is distinguished among turbulence models for its efficacy in airfoil design, especially in applications such as wind turbines and airplanes (Badran et al. 2025). Its capacity to manage intricate flow situations, including flow separation, reattachment, adverse pressure gradients, and vortex shedding, renders it a favored option by Badran et al. (2025). In comparison to models such as Spalart-Allmaras and ordinary k-Epsilon, the k-ω SST model yields more dependable forecasts for lift and drag coefficients, particularly in post-stall conditions (Adeel-Ur-Rehman et al. 2024). Also, the model can be fine-tuned with alterations of parameters like as turbulence constants to better anticipate specific airfoil shapes however the results might vary with designs. The k-ω SST model is very beneficial to investigate the NACA 65-421 airfoil because it can capture precisely the high-pressure gradients and adverse pressure areas, which are needed for accurate aerodynamic predictions byBadran et al. (2025). The relationship between angle of attack and aerodynamic efficiency for high lift coefficient development is studied in this research by using CFD and wind tunnel tests. The airfoil data is from the NACA database for an albatross inspired profile.

2.15. Annual energy production (AEP) and Coefficient of power Cp

Wind turbines convert the kinetic energy of wind to the rotating motion of turbine blades, driving the shaft of an electrical generator to generate electricity (Biswas & Chen 2025). The energy in the wind is proportional to the cube of the wind velocity. Understanding the attributes of wind resources is essential for any aspect of wind energy utilization, including site selection, economic feasibility assessment of wind farm initiatives, turbine design, and their impact on electricity distribution systems and consumers.

The power output, P,(as denoted in equation 5) from a wind turbine is given by the well-known expression(Wang et. al 2016):

$$P = \frac{1}{2} C_p \rho A v^3 \qquad (5)$$

where Cp is the power coefficient, A is the rotor swept area, ρ is the air density, and v is the wind speed. When the wind falls below a safe working maximum wind speed (cut-out) or at a minimum wind speed (cut-in), a wind turbine typically starts producing electricity. Naturally, a wind turbine's power performance during its operational period—from cut-in wind to cut-out wind determines its energy production. The wind turbine's output and operating characteristics are reflected in the power curve. A Weibull or user-defined distribution of hourly mean wind speeds is integrated with the turbine's power curve to determine the annual energy yield. It is assumed that the power curve varies linearly between a number of distinct wind speeds.

Biswas & Chen (2025) mentioned that the well-known Betz limit (Cp = 59.3%) offers the aerodynamic maximum of the power that can be taken from wind under the assumption that the wind speed in a rotor disk is constant, however, depending on the turbine design, the actual extracted power may be less. The classical Betz limit of the power coefficient (Cp = 16/27) is established under optimal aerodynamic conditions of a steady, incompressible flow at a constant velocity over the blade disk, featuring a non-rotating wake downstream and the absence of frictional drag (Biswas & Chen 2025).

Horizontal-axis wind turbines are employed extensively in wind farms due to their larger power coefficient, however vertical-axis wind turbines (VAWTs) possess several merits such as low manufacturing cost, structural simplicity and convenience of applications in urban areas (Kimiti et al. 2024). However, VAWTs have numerous disadvantages despite of their advantages, such as low power coefficient, poor self-starting capability, negative torque, and the corresponding cycle stress at particular azimuth angles. A good interpretation of the curve in figure 51 will show that when the wind has lost some of its total kinetic energy, a power of 0.59 may be obtained at one-third of the undisturbed wind, as contrasted with a power of 0.5(Kimiti et al. 2024). This is a contradiction in its own terms. The maximum real power coefficient varies from 0.45 to 0.50 (Kimiti et al. 2024).

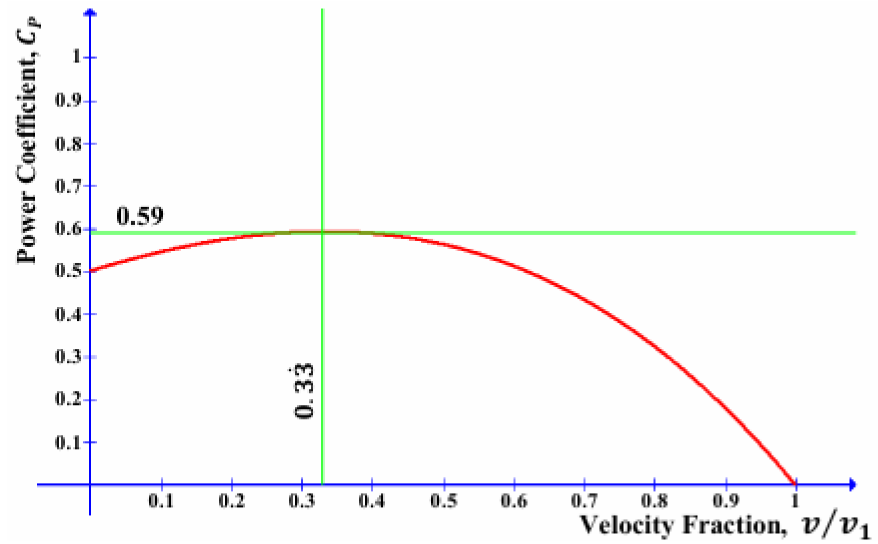

Figure 51: Power coefficient against velocity fraction (Kimiti et. al 2024)

2.16. Research gaps

a) Gap 1: AoA Range in Literature is Limited. The previous investigations considered mostly minor angles of attack whereas this study will focus on the -600 to 600 AoA. The severe flow conditions were not studied.
b) Gap 2: Velocity scope is limited. Most of the studies have been performed at low wind speeds and little is known about the performance at higher velocities (up to 5.36 m/s).
c) Gap 3: Corrugation location limited study of corrugation impacts on the upper surface layer, this work fills that gap with CFD and wind tunnel testing.
d) Gap 4: Validation across methods. Few studies coupled CFD calculations with wind tunnel tests under the same conditions, therefore lowering confidence in the practical applicability.
e) Gap 5: Behaviour of stall and flow separation. Lack of data on stall inception and flow separation over a wide range of angles of attack for bio-inspired blades.

CHAPTER 3: RESEARCH METHODOLOGY

3.1. Introduction

The present chapter is based on the literature review presented in Chapter 2 and covers the methodology employed to study the aerodynamic performance of a bio-inspired Horizontal Axis Wind Turbine (HAWT) blade. This work uses the NACA database airfoil data of an albatross-inspired profile to investigate the relationship between angle of attack and aerodynamic efficiency, especially the development of high lift coefficients using CFD and wind tunnel experimentation.

Five main components form the technique and are briefly detailed below for simplicity of reference following number:

1) Airfoil Selection and Data Acquisition: A specific NACA airfoil was selected for its ability to improve lift characteristics, due to the structure of an albatross wing. The 2D profile coordinates were extracted from the NACA repository (Airfoil Tools n.d.) and plotted in Microsoft Excel for geometry visualization.
2) Modelling Tools and Simulation Setup: The airfoil data imported to Solid Edge for the three-dimensional corrugated shape of the wind turbine blade. The produced 3D geometry was then imported into ANSYS Fluent for fluid-structure interaction simulations to study the aerodynamic performance at different angles of attack.
3) Experimental Procedures: Wind tunnel tests were carried out at uniform operating and boundary conditions at equal angles of attack. The results obtained were collected and used to validate the computational results.
4) Data sampling and analysis. The data sampling techniques used in Excel are explained, including the procedures for interpolation and smoothing. CFD results were compared with experimental findings to evaluate consistency and dependability.
5) Validity, Reliability and Ethical Considerations: The triangulation of data sources, the repeatability of simulations and the maintenance of controlled experimental circumstances are evidence of the methodological rigor of the study. Ethical aspects: Ethical data handling; Transparency of reporting; Acknowledgment of limitations.

The complete research methodology is shown in the form of flowchart in Figure 52.

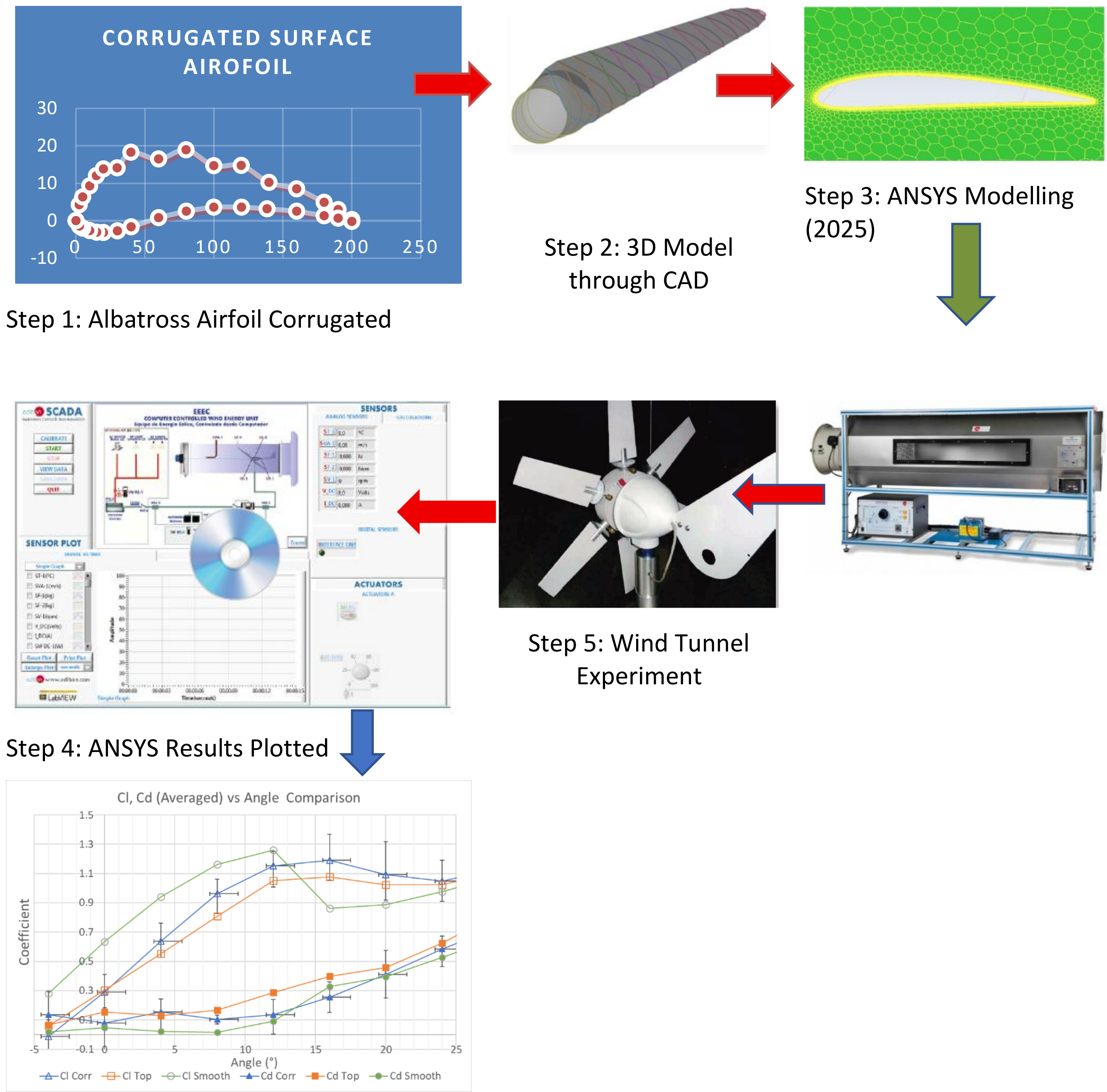

Figure 52: Methodology Flow Diagram

3.2. Research design

The 3D CAD software and ANSYS Fluent simulations created a virtual model of the airfoil from NACA website coordinates. Thereafter, the WT blades were 3D-printed from the generated 3D model which was the used in a wind tunnel to measure the coefficient of lift and drag for various angles of attack. From chapter 2, the literature review has shown various methods that were used to bring out an understanding of how the airfoil performs by altering its aerodynamics. The flow chart in Figure 52 explains in detail the methodology that was used followed in this research.

3.3. The turbulence model used

The k-omega Shear Stress Transport (SST) model is well known for its usefulness in aerodynamic design, especially in wind turbine blades and aircraft airfoils. Computational fluid dynamics extensively uses it because it can cope with the complex flow phenomena such as separation, reattachment, adverse pressure gradients, and vortex shedding. The k-ω SST model was selected for the present airfoil analysis because to its recognized capability of predicting high pressure gradients and adverse pressure areas for credible aerodynamic predictions.

3.4. NACA Airfoil – GOE174 (Ayon Sarkar et. al 2025)

Ayon Sarkar et. al (2025) explained the use of coordinate datasets from NACA website to produce the airfoil geometry. The airfoil that was used was GOE174 because it has a lower pitching moment coefficient which makes it more stable and easier to control. The GOE174 airfoil is an extensively examined profile within the NACA 4-digit family. It is characterized by the maximum camber and thickness parameters shown in Figure 53. The profile in Figure 53 was generated from the NACA coordinates shown in Table 1. Its camber and thickness distribution provided a balance between lift and drag, making it suitable for long-range gliders and it is inspired by the albatross bird.

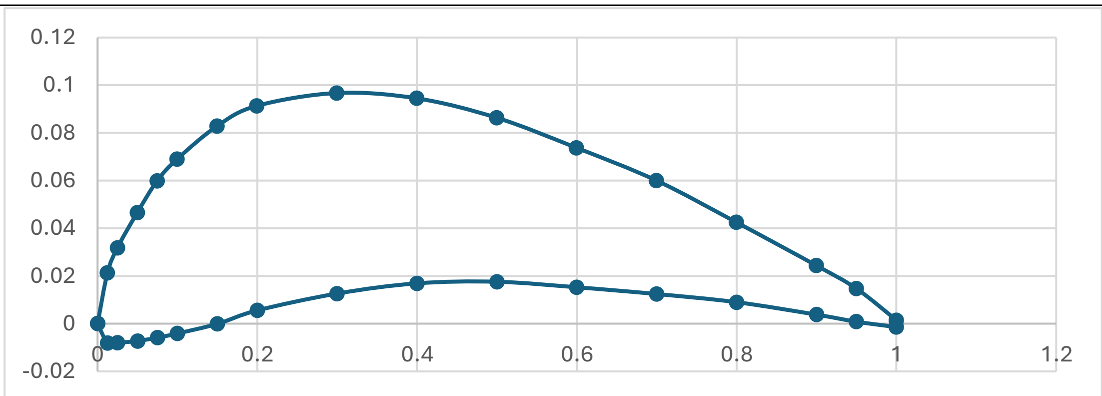

- Maximum camber 5.6% at 39.9% chord and Maximum thickness 8.6% at 19.9% chord.

Figure 53: Smooth GOE 174 Albatross 5020 profile

Table 1: Original Coordinates from NACA website in a “CSV file” of a GOE174

x	y		x	y
0	0		1	-0.00115
0.01236	0.02128		0.9499	0.00324
0.02479	0.03177		0.89984	0.00653
0.04969	0.04654		0.7998	0.01252
0.0746	0.0599		0.69245	0.01582
0.09953	0.06897		0.59971	0.01809
0.14944	0.08281		0.49971	0.01787
0.19938	0.09135		0.3998	0.01246
0.29935	0.09672		0.29994	0.00384
0.39936	0.0945		0.20013	-0.00827
0.49942	0.08637		0.15022	-0.01367
0.5995	0.07375		0.10025	-0.01568
0.69959	0.06002		0.07523	-0.01539
0.79971	0.0425		0.05019	-0.01329
0.89984	0.02437		0.02516	-0.00989
0.9499	0.01471		0.01262	-0.0072
1	0.00145		0	0

3.5. Airfoil sketch from NACA coordinates and corrugation method

The re-arranged coordinates were used to draw up a full 2D corrugated airfoil wing in excel and multiply each point by 200 to enlarge as shown on Table 2 and few points were corrugate only at the top layer.

Table 2: Rearranged Coordinates multiplied by 200 and corrugated upper points

x_upper	y_upper		x_lower	y_lower
0	0		200	-0.23
2.472	4.256		189.98	0.648
4.958	6.354		179.968	1.306
9.938	9.308		159.96	2.504
14.92	11.98		138.49	3.164
19.906	13.794		119.942	3.618
29.888	14.06475	y_{corr}	99.942	3.574
39.876	18.27		79.96	2.492
59.87	16.8405	y_{corr}	59.988	0.768
79.872	18.9		40.026	-1.654
99.884	14.36063	y_{corr}	30.044	-2.734
119.9	14.75		20.05	-3.136
139.918	10.7578	y_{corr}	15.046	-3.078
159.942	8.5		10.038	-2.658
179.968	4.874		5.032	-1.978
189.98	2.942		2.524	-1.44
200	0.29		0	0

An et al. (2021) has introduce a range of approximate numbers as shown on Table 3 and a sinusoidal corrugation formula applied to the GOE174 airfoil upper surface as:

$$y_{corr}(x) = y_u(x) + A.\sin\left(\frac{2\pi}{\lambda}x - \phi\right) \text{ An et al. (2021)} \quad (6)$$

Table 3: Parameters used on corrugation formula of GOE174 (An et al. 2021)

Symbol	**Meaning**	**Typical Range (for GOE 174)**
A	Corrugation amplitude (height of ridges)	0.01c – 0.02c
λ	Corrugation wavelength (spacing along chord)	0.10c – 0.15c
ϕ	Phase shift (alignment of peaks)	0 – 4.6
c	Chord length	Normalized to 1
$y_u(x)$	The smooth original coordinate on the position “y”.	

Symbol	**Minimum range using the modified Data**	**Maximum range using the modified Data**	**Average**
A	2	4	3
λ	20	30	25
ϕ	0	1.570796327	0.785398163
c	200	200	200

Following is the parameter symbol shown as a sketch on figure 54.

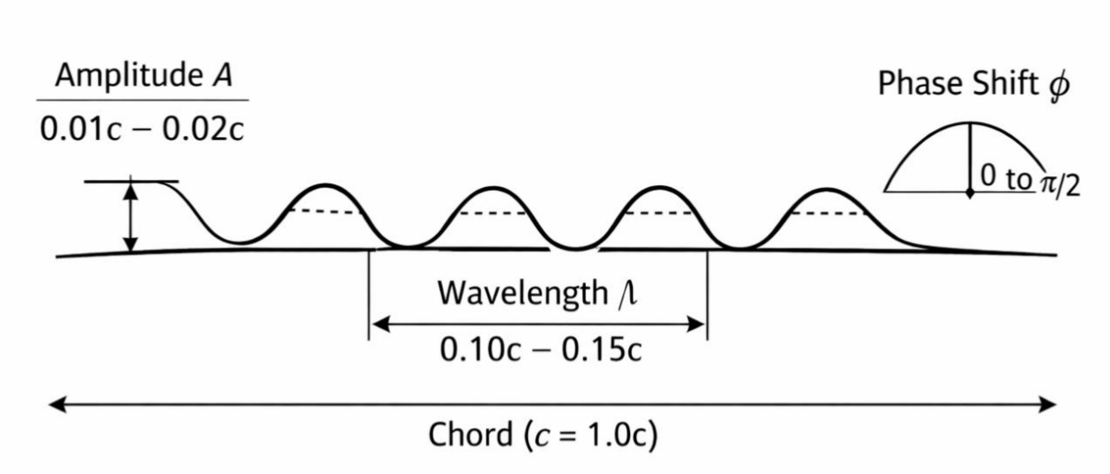

Figure 54: Corrugation Parameter Ranges for GOE174 Airfoil

On this airfoil, few points to corrugate where chosen and the phase shift numbers were manipulated in order to form a sinusoidal wave at the top of the airfoil as shown on figures 54 and 55 as the final corrugated blade.

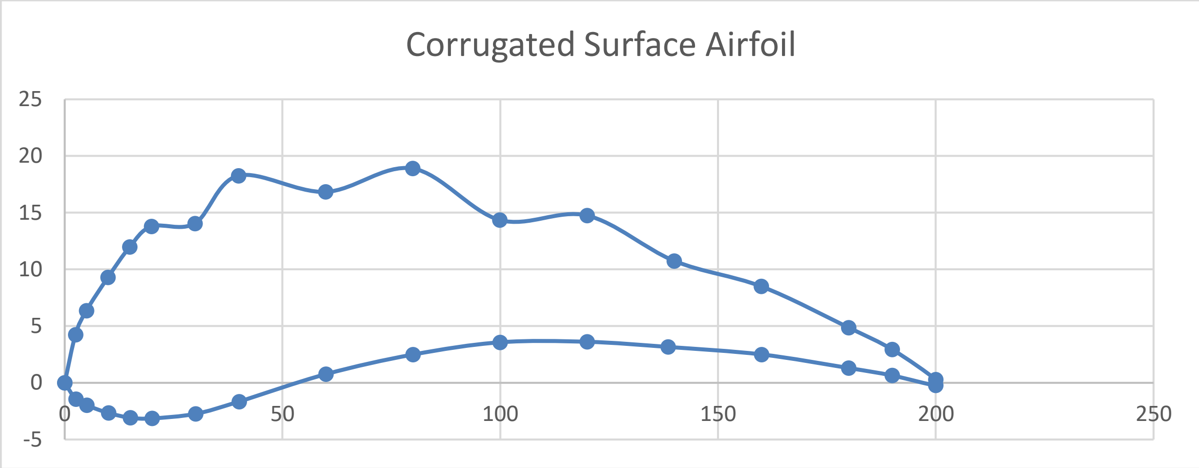

Figure 55: GOE174 Corrugated Airfoil Profile

3.6. 3D model through solid edge

The Solid Edge software was used to generate a 3D WT blade model from the GOE 174 airfoil coordinates which were captured in MS Excel (Khalid 2022). In order to produce a 3D model, the third coordinate was added in MS Excel as "z" and multiply everything by 200 to enlarge the wing. To be able to create a loft or full solid wing in Solid Edge, a feature called "curve by table" was used. Various excel tables were generated by reducing x-y coordinates in 10% intervals till 80%. Z coordinates were increased in intervals of 100 to 1000 apart and the wing on figure 55 was drawn. The z-coordinate represent the length of the wing, y- coordinate the thickness and x -coordinate e the width of the wing. The various excel tables were imported into solid edge software where a "curve by table" feature was used to produce a shape shown in figure 56.

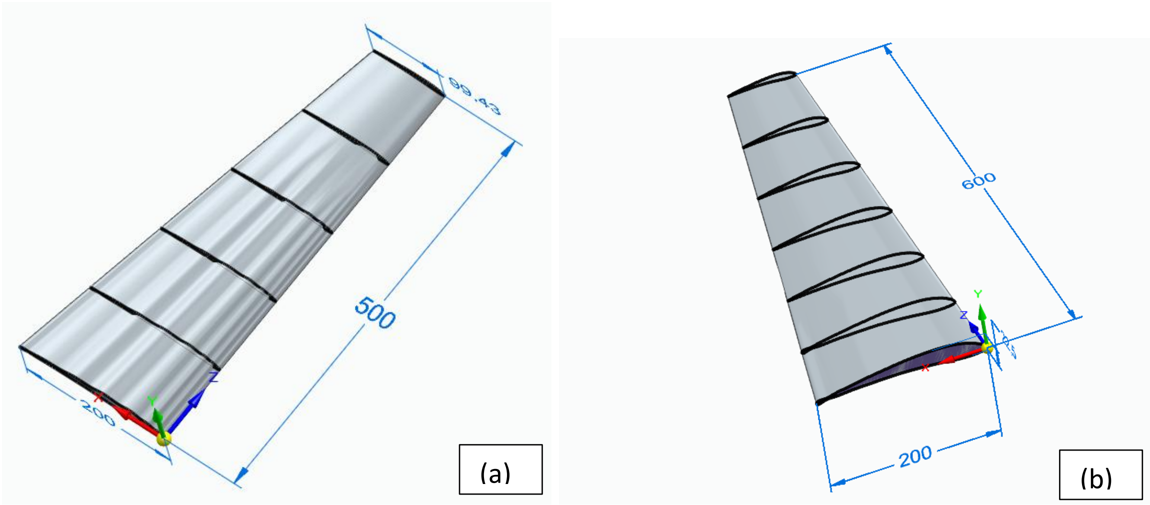

Figure 56: The solid surface (a) corrugated model and (b) smooth model of the wind turbine blades generated with Solid Edge from the GOE 174 coordinates in MS Excel

In order to increase performance, reduce drag, and boost overall efficiency, a corrugated airfoil and smooth model were modelled, figures 56 (a) and (b). For the sake of this study, the coefficients of drag and lift was determined through ANSYS simulation on both corrugated and smooth airfoil and Wind tunnel experiment results. Numerous variables, including the object's shape, the flow's velocity, and the angle of attack affect these results. Advancement in computational technology led to a better result.

3.7. Model development (computational fluid dynamics)

Ayon Sarkar et al. (2025) has used CFD software to model and in this study the same was used in this research which is ANSYS Software 2025R1 Student Version. CFD is a computational simulation that enables fluid dynamics to be analysed around or through an object, allowing for a detailed analysis of the impact on that object.

3.7.1. Geometry creation in design modeler

An Albatross corrugated and smooth airfoil wing was imported into the ANSYS Design. Ayon Sarkar et Al. (2025) has used a rectangular computational domain to simulate the airflow around the corrugated airfoil. The enclosure was created as seen in Figure 57 and 58 for this study. This was instituted to delineate borders for the inlet, outlet and walls conditions, Figure 61. This is to investigate the interaction of the wind turbine with the surrounding air during its dynamic operation.

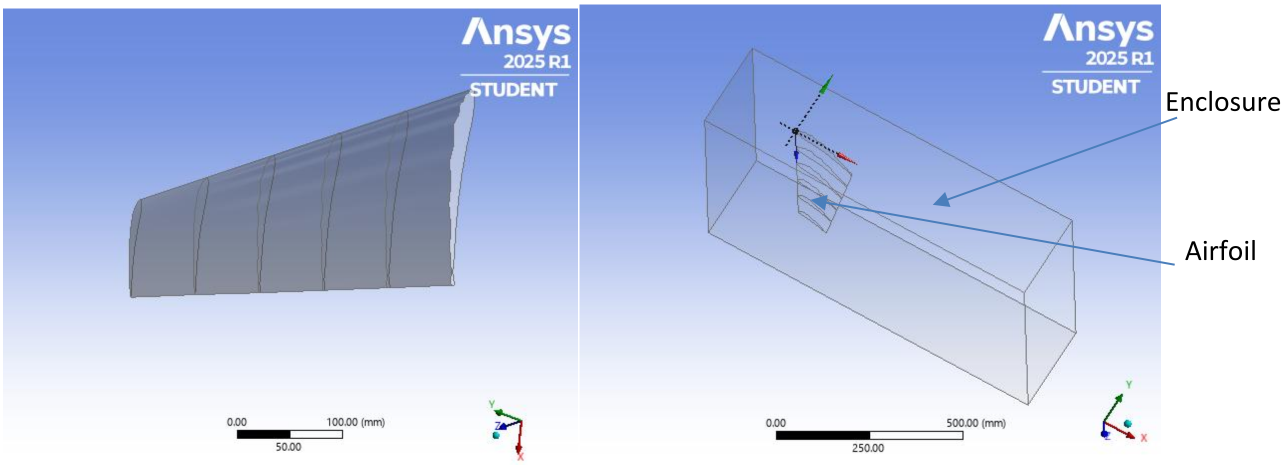

Figure 57: Imported igs. file and the enclosure created on fluent Software

After the enclosure was created, Figure 57, the corrugated airfoil was subtracted from the enclosure by using Boolean operation(Ghose et al. 2024). This subtraction was done to create a surface between corrugated airfoil and the boundary by subtracting the corrugated airfoil from enclosure. The Boolean operation creates the cavity by removing corrugated airfoil from the body. (Ayon et al. 2025) has explained that the domain should have ten times the chord length upstream at the intake to ensure uniform freestream conditions. (Ayon et al. (2025) reiterated that a distance of twenty times the chord length is required downstream (at the outlet) to accommodate wake development. Ensure the chord distance from the corrugated airfoil is a minimum of 10 times to mitigate the effects of wall interference.

3.7.2. Body transformation (rotating airfoil)

The results of coefficients of lift and drag are based on the body transformation of the wing, which is in a form of changing the Angle of attack. Various angles of attack were used, this is shown in Figure 58 before continuing to the meshing process. This is done in preparation of the calculation of the coefficients of lift and drag in relation to the angle of attack.

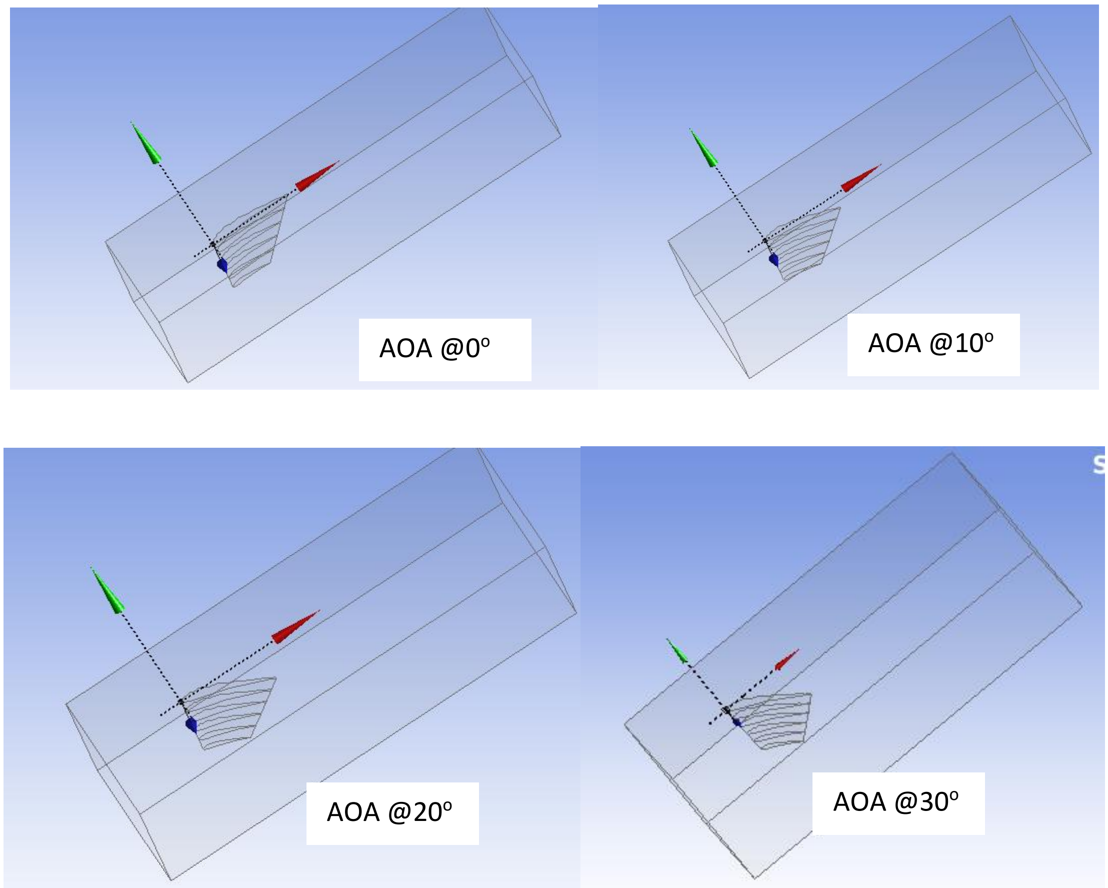

Figure 58: Various Angle of Attacks on ANSYS

Ayon et al (2025) has mentioned the importance of mesh quality on the precision and consistency of findings, making it a crucial aspect of CFD simulation. A refined mesh was generated over the corrugated airfoil body and an enclosure (fluid domain) as discussed in section, 3.7.3.

3.7.3. Mesh generation

In order to ensure a better problem-solving capabilities and accurate simulation; meshing should be done properly (Khalid 2022). To replicate fluid flow around the corrugated airfoil, a rectangular domain was used to create the structured mesh. The accuracy of the CFD solutions and the effectiveness of mesh generation are both impacted by the type of mesh (Animasaun et al. 2025; Aqilah et al. 2018). The 13mm cell size was the more accurate and more satisfactory on the production of the nodes and elements that were allowed in ANSYS 2025R1 student version software. The mesh shown in figure 59 has 13mm cell size. The breakdown of the mesh statistics shows 984 468 elements having 210 288 nodes. The cell size progressively grows outside the border layer, guaranteeing computing efficiency without compromising the precision required in the crucial areas. This hierarchical approach to mesh generation optimizes the use of computational resources by allowing coarser cells in remote areas with less sensitive flow behavior and more refined resolution in areas where flow features are critical. This systematic mesh with minimum cell gap around the airfoil helps to complete the simulations faster and also gives reliable data for aerodynamic analysis. Looking at Table 4, the meshing used has an acceptable minimum orthogonal quality of 0.21369 which is greater than 0.1 for better simulation results.

Ayon Sarkar et al. (2025) has incorporated a seamless transition illustrated by inflating layers adjacent to the corrugated airfoil surface to address boundary layer issues with enhanced accuracy. Looking at the Figure 59, inflation layers can be seen on the mesh structure.

Table 4: Data about the Mesh

Description	Quality of Elements	Orthogonal Quality	Aspect Ratio
Min.	0.057548	0.21369	1.1673
Max.	0.99979	0.99478	18.493
Average	0.77544	0.72872	2.2991
Element Size	13mm		
Nodes points	210 288		
Elements	984 468		

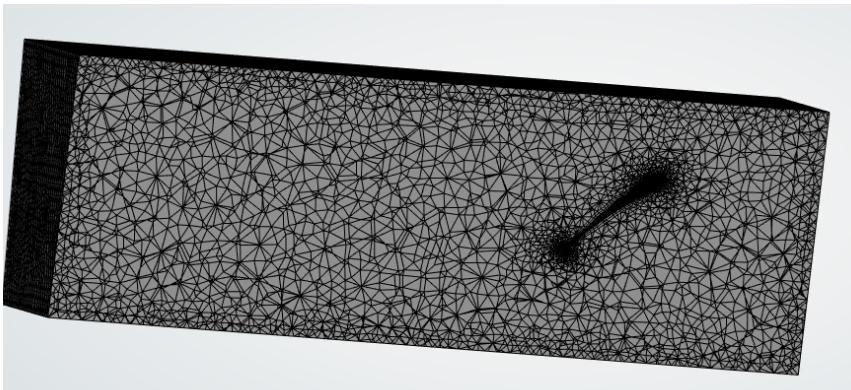

(a)

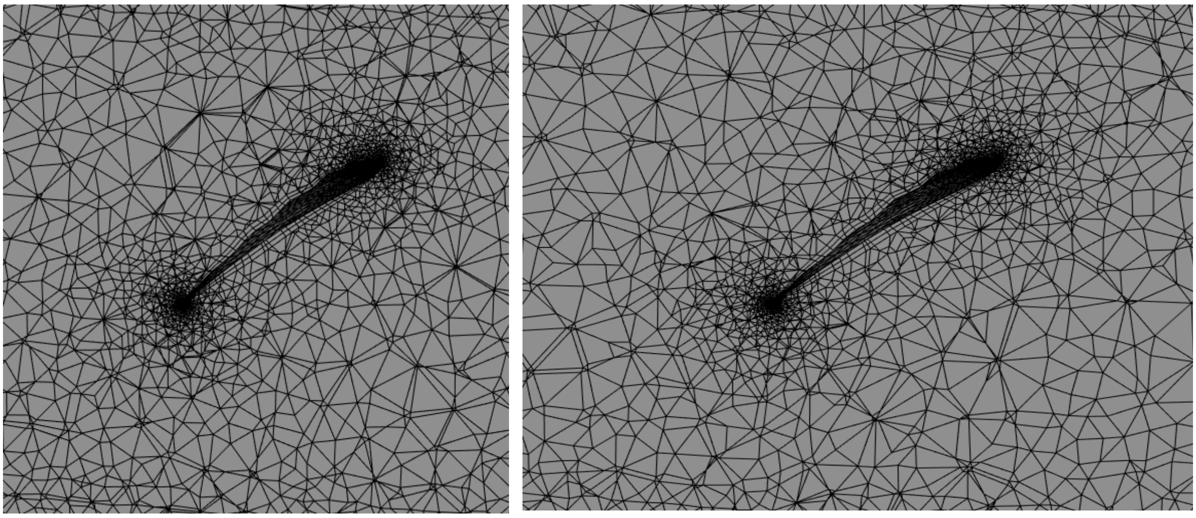

(b) (c)

Figure 59: Structured mesh of corrugated GOE174 Airfoil at 40° AOA (a) meshing at 13mm element size, (b)meshing at 14mm element size, and (c) Meshing at 15mm element size

3.7.4. Mesh convergence check

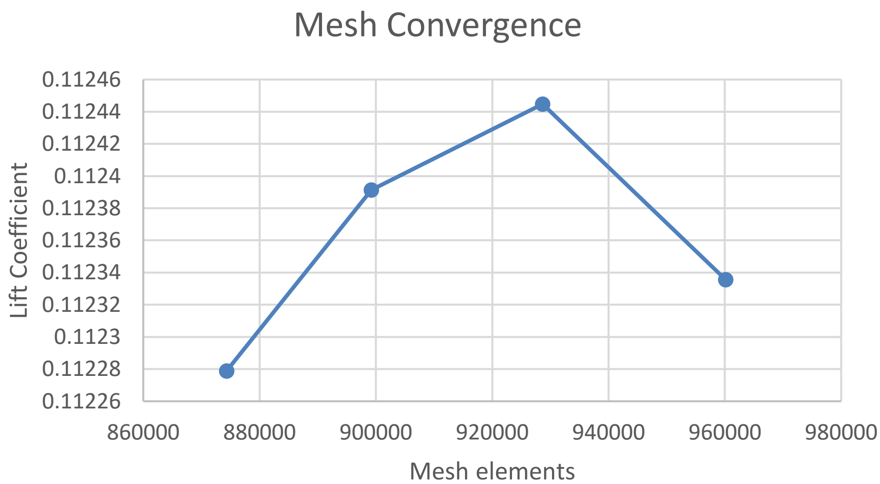

Figure 60: Mesh Convergence tested at a 40^0 angle of attack

To ensure numerical accuracy and mesh independence of the CFD results, a mesh convergence study was done by systematically refining the mesh and monitoring changes in the lift coefficient (ANSYS Inc 2024). Four mesh configurations ranging from 874,319 to 960,139 elements were evaluated. The lift coefficient varied marginally from 0.11227882 to 0.11244475 across the refinement range, with less than 0.0002 difference between the final three meshes, on figure 60. This systematic mesh with minimum cell gap around the airfoil helps to complete the simulations faster and also gives reliable data for aerodynamic analysis. Thus, for the remaining simulations, the mesh with about 928,694 elements was chosen, as it provides a trade-off between computing efficiency and numerical quality. The convergence behaviour confirms that the solution is sufficiently independent from mesh resolution for aerodynamic analysis (Lu et al. 2021; Aqilah et al. 2018; Muruga et al. 2021).

3.7.5. Set-up of boundary conditions

According to Patel et al. (2014), to consider a flow around corrugated airfoil, there must be initial inputs and boundary conditions to be used. To guarantee precise and realistic results, suitable boundary conditions were established for the fluid flow simulation surrounding the corrugated GOE174 airfoil (Asadi Ali 2026). Boundary conditions were prescribed to replicate the physical environment of the airfoil in flow(Asadi Ali 2026). The input was specified by uniform velocity condition and the outflow by static pressure condition. The intake boundary condition was set to have the same speed at all sites of the incoming flow. This boundary characterizes the variation of the free-stream circumstances as they get closer to the corrugated airfoil. The corrugated airfoil surface was turned into a wall that doesn't slip so that the corrugated airfoil and the boundary layer could interact properly. This signifies that the fluid moves at a speed of zero at the surface. The exit, where the flow can leave at a particular static pressure (typically adjusted to atmospheric conditions), was named the outer domain limits. It was named domain limits to make sure that the flow goes out smoothly and doesn't come back in. Finally, the walls of the surrounding domain were identified as having no-slip conditions, the walls (Ayon et al. 2025), which prevented fluid from flowing through the boundaries, with the exception of the corrugated airfoil surface. Together, these boundary conditions as shown in Table 5 guarantee that the solver converges to precise aerodynamic results by enabling a realistic modelling of the airflow surrounding the corrugated GOE174 airfoil.

Table 5: Boundary Conditions and element properties

Inlet boundary conditions	
Inlet	Velocity-outlet
Temperature	288.17K
Outlet boundary conditions	

Outlet type	Pressure -Outlet
Gauge Pressure	0 Pa
Wall boundaries	
Wall motion	Stationary wall
Initialization Method	Hybrid Initialization
Properties of Flowing Fluid	
Fluid	Air
Density	1.225 kg/m3
Viscosity	1.7894e-05 kg/m-s

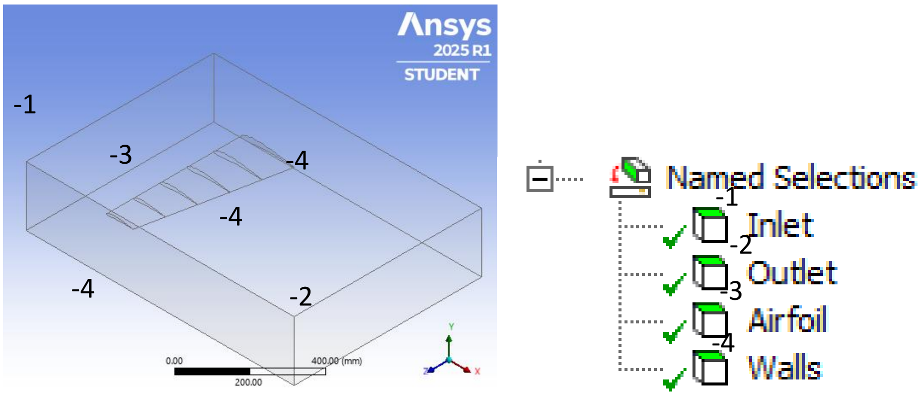

Figure 61: Boundary name selection applied to the fluid domain and airfoil

The aerodynamic performance of the corrugated GOE174 model was determined through simulations. It is often expedient in ANSYS Fluent to group certain entities with similar attributes and give them a specific name to avoid unnecessary repetition when assigning their properties. These are called “named selections” in ANSYS fluent. The faces that made up the boundary of the fluid domain were selected and assigned a specific name before exporting the mesh into the FLUENT solver(Isyaku Kunya et al. 2024) to facilitate the prescription of boundary conditions. These faces are the airfoil surface, the inlet, the outlet, and the symmetry boundaries(Isyaku Kunya et al. 2024). Named selections such as inlet –uniform velocity condition, outlet – static pressure condition, airfoil – no-slip condition, and wall were applied in this study, as shown in Figure 61.

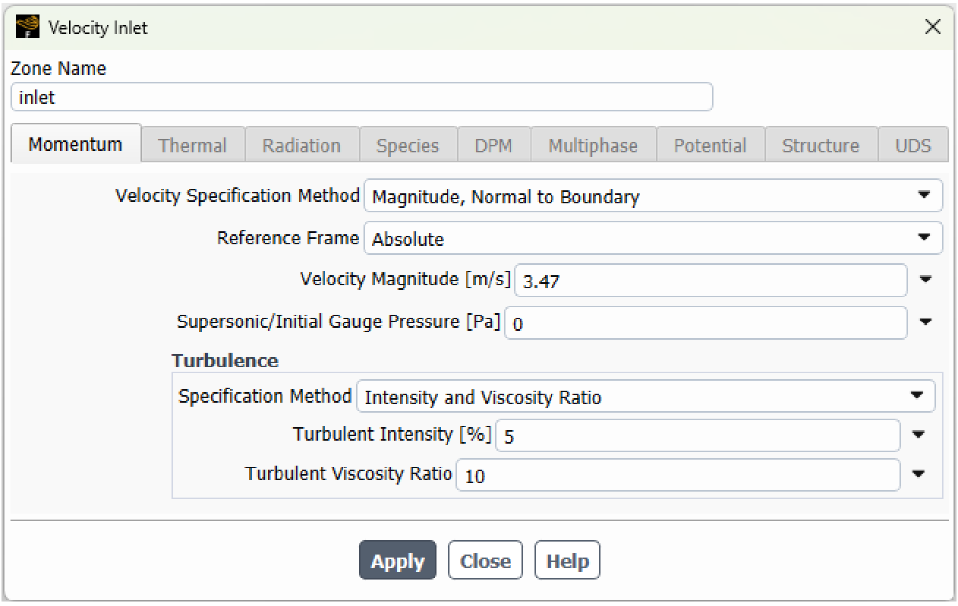

Figure 62: Velocity Inlet Input during Simulations at 40^0

Khalid (2022) stresses how important it is to find the horizontal and vertical parts of velocity at every angle of attack. In this study, rotation was previously completed under geometry configuration. The input speed is 3.47 m/s at an angle of attack of 40^0, as shown in Figure 62.

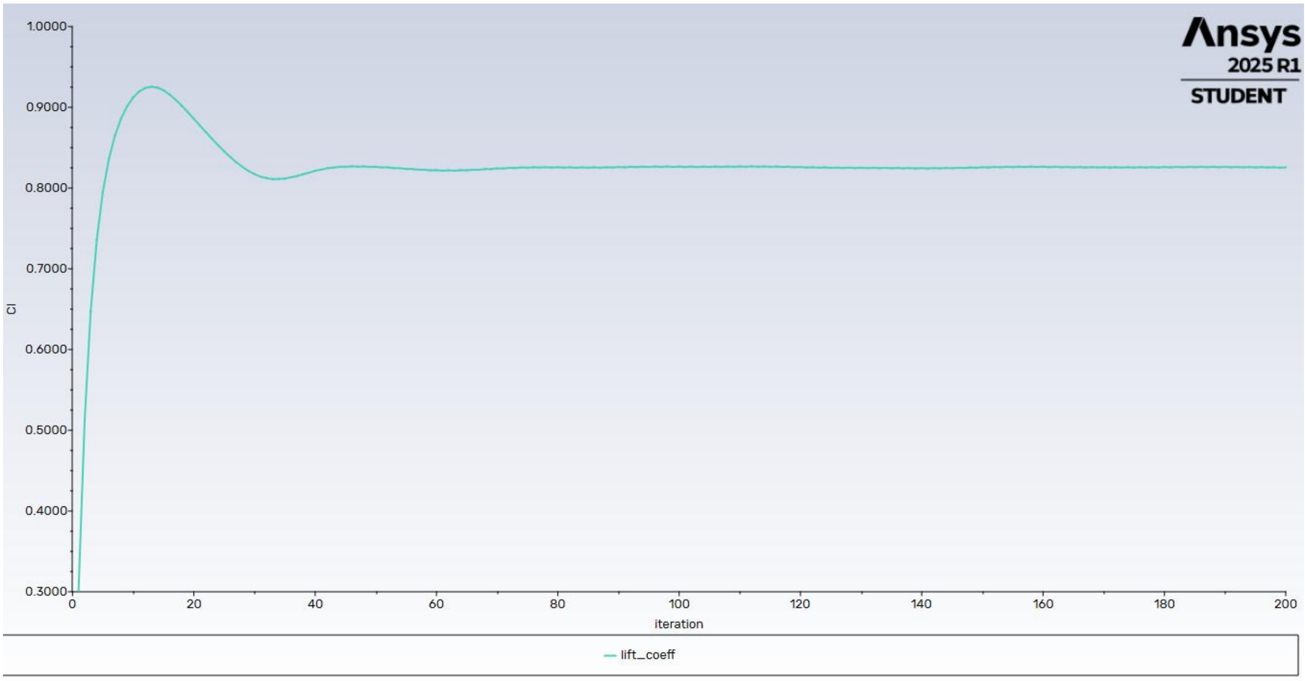

Figure 63: Lift Coefficient Iteration during Simulation at 10^0 Angle of Attack

The early surge in figure 63 above indicates that the flow is swiftly clustering around the corrugated airfoil, most likely creating high circulation and pressure differentials. This surge is indicated by the sharp spike in C_L. This trend is common in simulations with complex geometries or turbulent flow, where the original guess is distant from the ultimate result. The slight dip that follows the peak, which occurs between 10 and 20 iterations, may be a sign of temporary flow modifications, such as vortex shedding or turbulence model recalibration (Zhang et al. 2025). This behaviour is typical of the k-ω SST model. Excellent convergence is demonstrated by the near-constant C_L value, which is little less than 0.9, after iteration 50. This near-constant line indicates that the solver is no longer making noticeable corrections and that the flow field has stabilized. Patel et al. (2014) also demonstrated the iterations on coefficients of lift and drag graphs.

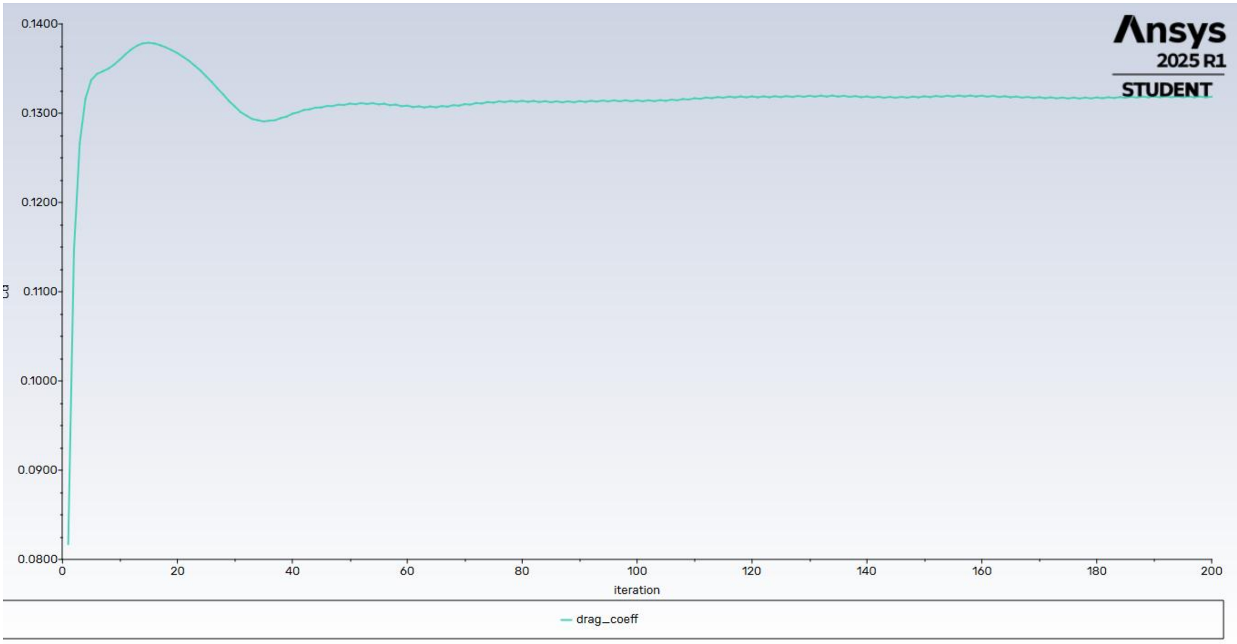

Figure 64: Drag Coefficient Iteration during Simulation at 10^0 Angle of Attack

As shown in Figure 64, the solver overshoots and starts to settle into a more physically realistic flow field when the peak around 10 is followed by a decrease.

The curve flattens out at 50 interactions, indicating that the drag coefficient is convergent, indicating low residuals and little change in the flow field. The flat line indicates that the simulation is getting close to steady state (Ayon Sarkar et al. 2025).

3.8. Wind tunnel experiment

3.8.1. Production of the wind turbine blade

The corrugated blade geometry from Solid Edge software was saved as “stl” file. The “stl” file was done in order to open it on Preform software for 3D printing purposes as shown in Figure 65. The Preform software helped to scale the corrugated airfoil in order to produce the size that was able to fit into the wind tunnel for experimental purposes. The material that was used for 3D printing is Tough 1500 resin material with Ultimate tensile strength of 26MPA, elongation at break of 69% and Tensile modulus of 0.94GPa. The specimen size was 62mm x 155mm size as shown on figure 64. The experiments were carried out using various velocities ranging from 2 – 6 m/s in an open circuit, suction type, low-speed wind tunnel. The weight of the specimen was also measure on figure 66. The weight was used to calculate the final coefficient of drag and lifts after the experiment.

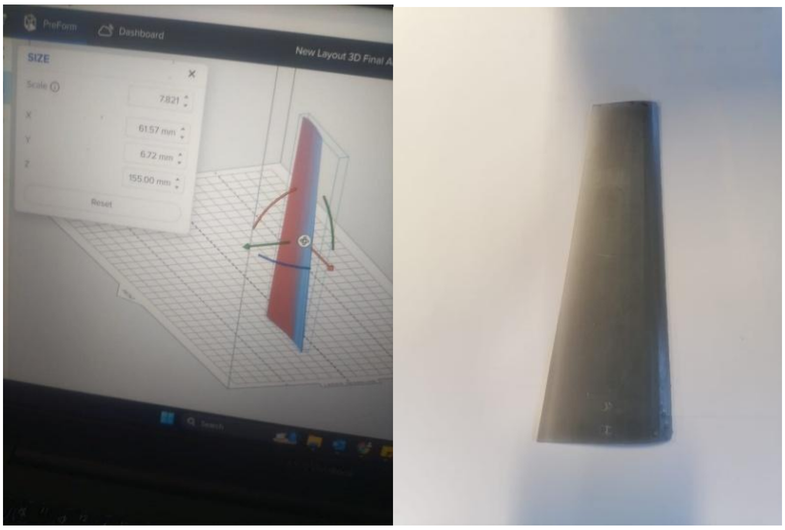

Figure 65: Preform Software to scale the airfoil vs the final product printed out

Figure 66: A digital scale used to weigh the 3D printed blades

3.8.2. Wind tunnel setup

A wind tunnel in figure 67 is an instrument used in aerodynamic research to look at how air traveling past solid objects affects them (Thakkar et al.). Changing the speed of the axial fan's rotation changes the speed of the air (Sreedevi KNV et al. 2020). This fan makes the air flow that is needed to turn the rotor of the wind energy unit.

Figure 67: Wind Tunnel Machine

The parameters measured are air temperature, airspeed, rotor speed, voltage, and current. A temperature sensor is located before the rotor of the aerogenerator (*Practical Exercises Manual 2013)*. All the sensors are shown on figure 68. The airspeed is monitored using a sensor positioned in the tunnel, and the rotational speed of the aerogenerator is also determined (in rpm). A voltage and current sensor enable the measurement of voltage and current that can be used to further calculate the generated power using the expressions given by equations on page 23-24. All acquired data was recorded in an Excel file and analyzed to derive the lift and drag forces, subsequently determining these forces using the angle of attack.

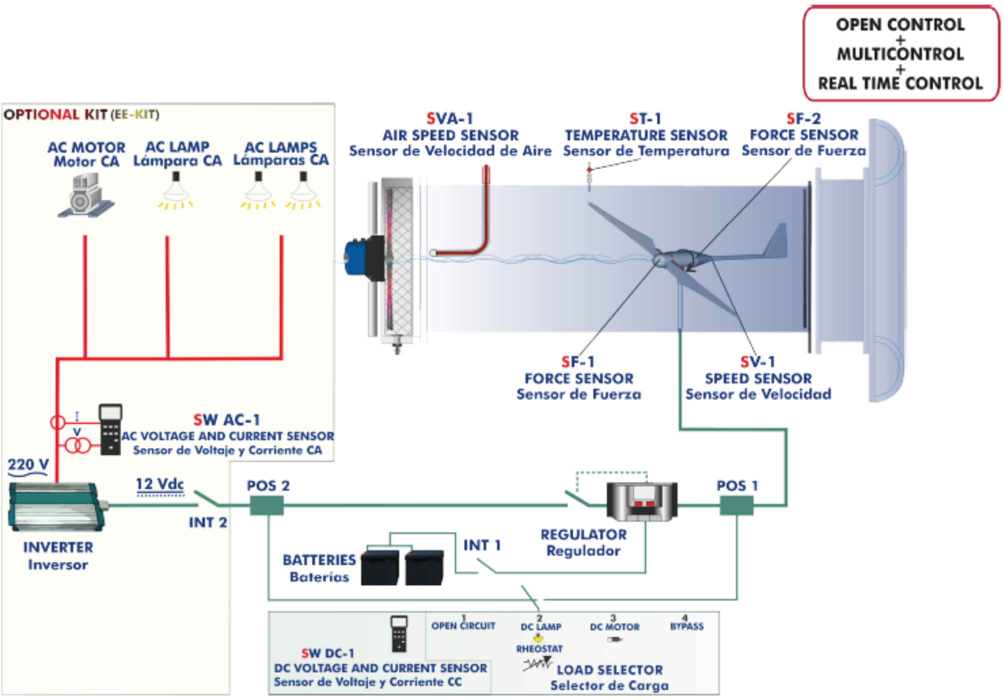

Figure 68: Process Diagram and Unit Elements Allocation of Wind Tunnel

To assess the efficacy of tiny wind turbines, a well-equipped wind tunnel system is required, comprising several essential components (Animasaun et al. 2025). The major source of the air flow is the air generator fan, which is an axial fan with a speed control, with the maximum air flow of 10,650 m^3/h and 1.5 kW of power. The air tunnel is made of stainless steel and has the size of about 2000x550x550 mm. The glass window of 1100x200 mm allows visual viewing of experiments and taking of measurements. The turbine and generator assembly was designed to work satisfactorily from wind velocities of 2 m/s. The safety turbine was built with six blades joined at their tips, for better structural stability. The system is a low-friction alternator with fixed shaft, for smooth and silent operation, and can produce power up to 60 W. Additionally, a battery charger and load regulator are incorporated to store and control the electrical output, ensuring stable and efficient performance during testing.

3.8.3. Wind tunnel experimental method

The tests were conducted at low speeds ranging from 2 to 6 m/s in an open-circuit, suction-type wind tunnel. The tunnel's airflow was supplied by a thyristor DC motor and a single-stage axial flow fan with a maximum speed of 2800 rpm. The size of the test section is 2000 x 550 x 550 mm and the velocity can be increased progressively from 5 m/s to 40 m/s as shown on figure 69. While the aerogenerator's rotational speed is measured in revolutions per minute (rpm), the airspeed inside the tunnel is measured using an anemometer (Thakkar et al. 2013). Air temperature, airspeed, rotor speed, voltage, and current are among the parameters that are recorded. In front of the rotor of the aerogenerator is a temperature sensor. Furthermore, power consumption can be calculated thanks to a voltage and current sensor that measures both voltage and current. There is a Perspex window in the test area that measures about 1000 x 130 mm. The pitot tube and the hot-wire anemometer probe can move along the test section's length thanks to a traversing mechanism that is placed above it. Air is allowed to freely enter the settling chamber through a bell-mouthed entrance section.

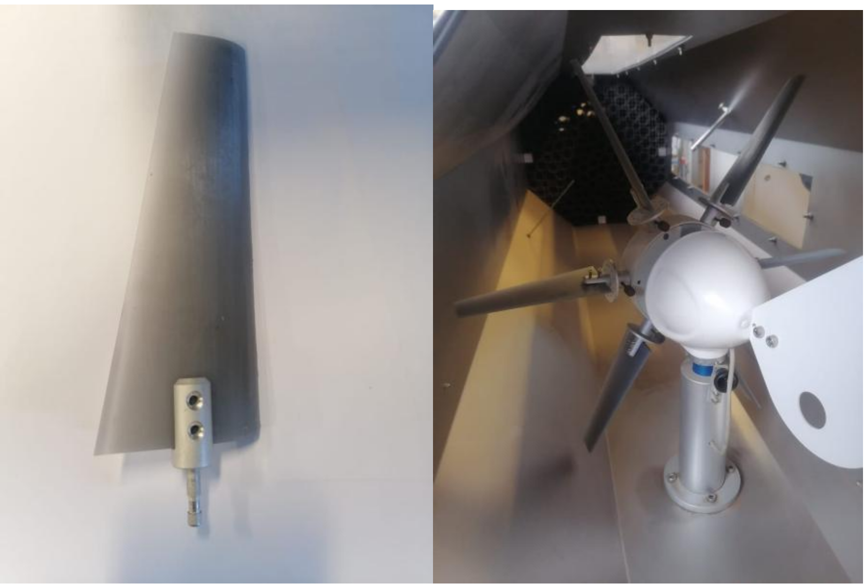

Figure 69: Corrugated Airfoil in a jig to hold it together and fitted in a wind tunnel

The impact of surface corrugation on airfoil performance was evaluated in a wind tunnel. The airfoil was held by a force gauge rig to avoid it from moving or falling off during experiment. The primary idea behind it is that air flow is let to pass through the test object in order to collect data on aerodynamic forces**.** Fan, intake, settling the chamber, test section, and diffuser make up a standard wind tunnel. When power is applied, the fan spins and draws air in**.** In order to create laminar flow, the turbulent air drawn in from the intake is forced to pass through a succession of flow straighteners in the settling chamber. The angles of attack were engraved on a protractor when operated manually by turning an airfoil to suit the chosen angle.

3.8.4. Experimental protocol

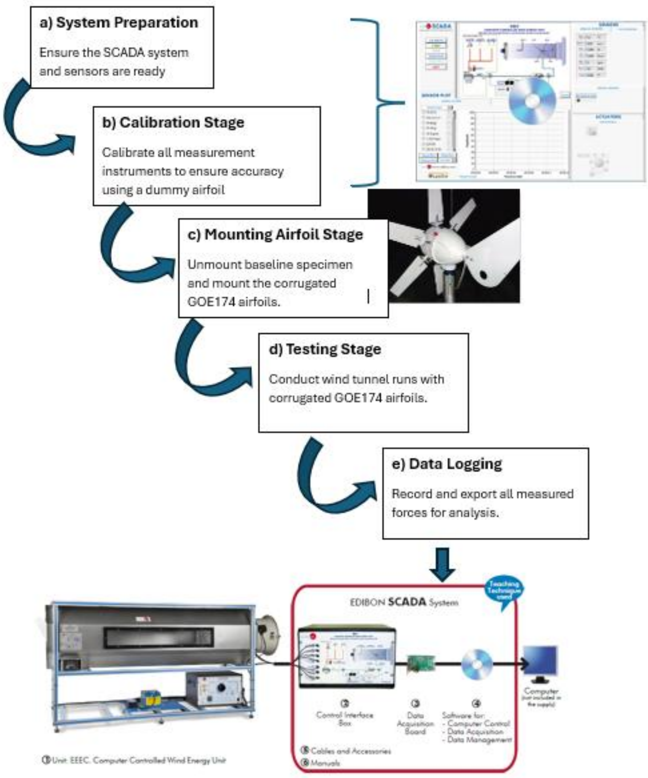

Figure 70: Wind Tunnel Experiment Flow Diagram

Figure 70 shows the flow diagram of the wind tunnel experiment.

Test was conducted as follows:

i) Wind speed ranges from 2m/s to 6m/s

ii) Each test was done for 5 minutes per wind speed and angle of attack

iii) The airfoil is manually adjusted to place it on the desired angle of attack on the protractor.

3.8.5. Blockage ratio check

The blockage ratio is a key parameter in wind tunnel testing that quantifies how much of the tunnel's cross-sectional area is occupied by the test model. It matters because the presence of the model alters the flow field, potentially distorting aerodynamic measurements if not accounted for.

Airfoil area = L*span = 0,155m *0,062m = 0,00961m^2

Cross-sectional area of a Wind Tunnel test section = 0,55m*0,55m = 0,3025m^2

Blockage ratio = Area of Airfoil / Area of the wind tunnel = (0,00961/0,3025) *100 = 3,18%

According to Wang et al. (2022), blockage ratios below 5 % produce negligible interference effects in closed-section wind tunnels; therefore, no correction was applied.

3.8.6. Generating lift and drag coefficient from scada -data processing

$$F = ma = N \quad (7)$$

As the airflow passes over airfoil, pressure difference generates aerodynamic forces, signals are amplified and transmitted to the SCADA for real-time monitoring. The wind tunnel system records lift (L) and drag (D) values at various angles of attack and wind speeds. This is the force (Khalid 2022),shown on equation 7, page 72, the product of the mass and accelerarion that was applied on the airfoil in order to compute the non-dimensional coefficients. It is measured in Newtons (N). Mass of a 3D corrugated airfoil = $m = 0.0257\ kg$. It was used in the wind tunnel for an experiment.

$$a = \frac{v}{t} = \left(\frac{m}{s^2}\right) \quad (8)$$

Density of air $\rho = 1.2\ kg/m^3$ is the mass of air per unit volume, usually denoted in kilograms per cubic meter (kg/m³). It plays a crucial role in aerodynamic calculations, especially in Sri et al. (2023).

Velocity (shown in equation 8, page 72) of air ranges from 2m/s to 6m/s = $v = m/s$ refers to the speed and direction of airflow relative to a surface or object, such as an airfoil. It's an important factor in determining aerodynamic forces such as lift and drag as used in equation 8, page 72.

The angle of attack α in degrees varies from 0° to 60° and from -20° to -60°. The angle of attack is the angle between the direction of the oncoming airflow (relative wind) and the chord line of an airfoil. This is an important parameter in the assessment of aerodynamic properties of wings and airfoils.

This airfoil has a breadth of 0.069 m, which is the linear distance between the leading edge and the trailing edge, denoted as b. It defines the "width" of the airfoil in proportion to the flow direction. It is used in the calculation of Reynolds number.

Zhang et al. (2025) pointed out that the length of the airfoil $L = 0.155\ m$

Zhang et al. (2025) defines drag Force = $F_D = F * \cos\alpha\ (in\ radians)$ (9)

as the aerodynamic resistance experienced by an item traversing a fluid (such as air). It operates contrary to the direction of motion and is a key factor in airfoil performance as equation 9, page73 explained.

Zhang et al. (2025) defines Lift Force = $F_L = F * \sin\ \alpha\ (in\ radians)$ (10)

as the aerodynamic force that acts perpendicular to the direction of the oncoming airflow. It enables wings and airfoils to overcome gravity and is a central focus in aerodynamic design and analysis

$$C_L = \frac{F_L}{0.5\rho A v^2} \quad (11)$$

(Khalid 2022) define the coefficient of lift shown on equation 11, page 73, as a dimensionless quantity that relates the lift of an airfoil to the density of the fluid surrounding the airfoil's shape.

Coefficient of Lift = is a dimensionless number that quantifies how effectively an airfoil generates lift relative to the dynamic pressure and reference area. A represents airfoil area (Khalid 2022) and v represents air velocity (Khalid 2022). F_L represents the force of drag (Khalid 2022).

$$C_D = \frac{F_D}{0.5\rho A v^2} \quad (12)$$

Coefficient of Drag as shown on equation 12, page 73 = is a dimensionless number that quantifies the drag force acting on an object relative to the dynamic pressure and reference area (Khalid 2022). The ρ represents the density of air (Khalid 2022). F_D represents the force of drag (Khalid 2022).

3.9. Summary

In order to assess the aerodynamic performance of a bio-inspired airfoil, this chapter described a mixed-methods technique that included computational and experimental research. CFD and wind tunnel testing setup are the two primary stages of the process.

While wind tunnel testing physically analyzes aerodynamic forces and flow behavior under controlled conditions, CFD uses discretized governing equations to numerically simulate fluid flow.

Zhang et al. (2025) stated that comparing the CFD calculation results with the wind tunnel test results is required to confirm the accuracy of the aforementioned simulation method. Chapters 4 and 5 will address this.

CHAPTER 4: COMPUTATIONAL FLUID DYNAMIC RESULTS AND DISCUSSION

4.1. Introduction

Chapter three explored the methodology used to arrive at the CFD results that is being discussed on this chapter. The following chapter will be focusing mainly on the results found through CFD modelling. The boundary conditions of the CFD modelling were made to resemble that of wind tunnel experiment by Zhang et al. (2025). A thorough examination of the airfoil's performance is performed by simulating a range of angles of attack from -60^0 to 60^0 to clarify the impacts on lift and drag coefficients, along with other essential flow characteristics, with the results presented. This section demonstrates the influence of $\boldsymbol{\alpha}$ and inlet velocity on the coefficient of lift (C_L), coefficient of drag (C_D), and their ratio (C_L/C_D) as discussed in this chapter as mentioned by Zhang et al. (2025). The $\boldsymbol{\alpha}$ varies from -60^0 to 60^0 with a gap of 10^0 was investigated through CFD.

Chapter 4 is organized into five key sections to present and discuss the results of the CFD simulation. First section details the data results collected during simulation followed by a discussion of their implications. The second section examines the velocity and pressure contours at varying angles of attack, highlighting flow behaviour and pressure distribution across the corrugated airfoil surface. The third section presents graphical results illustrating the variation of lift and drag coefficient with respect to the angle of attack, proving insights into aerodynamic performance. The influence of inlet velocity on aerodynamic characteristic across angle of attack will be highlighted on section four of this chapter. Lastly the analyzation of smooth vs corrugated airfoil lift-to-drag coefficient ratio as a function of angle of attack, pwer coefficient and effect on annual energy production offering a comparative metric for aerodynamic efficiency (Zhang et al. 2025).

4.2. CFD simulation data results and discussion

4.2.1. Corrugated airfoil data results and discussion

The following angle of attack were used with constant inlet velocities of 2.081; 2.71; 3.47; 4.08 and 5.36 m/s. The CFD was used to simulate corrugated airfoil performance analysis to produce C_l, C_d vs AoA. The following tables are the results found on the CFD simulations.

Table 6: Corrugated CFD Simulation Data Results of Cl, Cd and Cl/Cd vs various AoA @ Inlet Velocity of (a) 2.081m/s; (b) 2.71 m/s, (c) 3.47m/s, (d) 4.08 m/s

CFD Velocity (m/s)		2.08 m/s	
Degree	**Cl**	**Cd**	**Cl/Cd**
-60	-0.340	0.607	-0.560
-50	-0.369	0.476	-0.775
-40	-0.322	0.312	-1.033
-30	-0.258	0.189	-1.363
-20	-0.201	0.110	-1.817
-10	-0.112	0.045	-2.499
0	0.092	0.037	2.475
10	0.308	0.047	6.518
20	0.373	0.465	0.802
30	0.399	0.226	1.761
40	0.433	0.359	1.205
50	0.495	0.580	0.853
60	0.479	0.810	0.591

CFD Velocity (m/s)		2.71 m/s	
Degree	**Cl**	**Cd**	**Cl/Cd**
-60	-0.643	1.145	-0.561
-50	-0.638	0.822	-0.776
-40	-0.594	0.573	-1.036
-30	-0.481	0.351	-1.368
-20	-0.342	0.187	-1.828
-10	-0.191	0.076	-2.528
0	0.175	0.028	6.169
10	0.574	0.083	6.897
20	0.687	0.223	3.087
30	0.784	0.444	1.764
40	0.865	0.717	1.207
50	0.886	1.039	0.853
60	0.786	1.330	0.591

CFD Velocity (m/s)		3.47 m/s	
Degree	**Cl**	**Cd**	**Cl/Cd**
-60	-1.023	1.820	-0.562
-50	-1.032	1.329	-0.777
-40	-0.942	0.908	-1.037
-30	-0.790	0.576	-1.372
-20	-0.562	0.306	-1.837
-10	-0.313	0.123	-2.550
0	0.264	0.040	6.552
10	0.854	0.119	7.172
20	1.010	0.326	3.104
30	1.164	0.659	1.766
40	1.351	1.119	1.207
50	1.393	1.631	0.854
60	1.220	2.062	0.591

CFD Velocity (m/s)		4.08 m/s	
Degree	**Cl**	**Cd**	**Cl/Cd**
-60	-1.456	2.587	-0.563
-50	-1.456	1.873	-0.777
-40	-1.343	1.295	-1.038
-30	-1.094	0.796	-1.374
-20	-0.779	0.423	-1.842
-10	-0.431	0.168	-2.563
0	0.405	0.058	6.937
10	1.297	0.177	7.347
20	1.517	0.489	3.104
30	1.744	0.987	1.767
40	1.973	1.633	1.208
50	1.926	2.255	0.854
60	1.663	2.811	0.591

Looking at the CFD data table 6, at 3.47 m/s gives a detailed look at how lift (Cl) and drag (Cd) vary with angle of attack (AOA) from – 60° to +60°. Looking at negative angle of attack, which is -60^0 to -10^0, the coefficient of lift is strongly negative reaching a minimum of -1.032 at -50^0. This negative value on the lift results indicates the reverse lift, typically of an inverted flow or post stall behaviour.

When looking at the positive angle of attack, which is from 0^0 to 60^0, the coefficient of lift increases sharply, peaking at 1.393 at $+50^0$. After 50^0 AoA, the coefficient of lift starts to decline, indicating stall onset or flow separation. The peak of coefficient of lift at 50^0 shows strong lift generation, possibly due to vortex lift or delayed separation from surface geometry which is corrugation (Zhang et al. 2025).

The coefficient of drag is high, peaking at 2.062 at 60^0, then decreasing towards 0^0. This reflects flow resistance due to reversed flow and separation. The coefficient of drag starts low at 0.040 at 0^0 and increase steadily, reaching 2.062 at 60^0. The sharp rise after 30^0 suggests significant flow separation, increasing pressure drag.

It can be seen that at angle of attack of 10^0, there is the best balance of lift and drag, these can be seen by a high Cl/Cd ratio ranging from 6.518 to 7.347 which is the highest. The efficiency drops sharply beyond AoA of 30^0 due to drag rise.

4.2.2. Comparative aerodynamic performance of smooth and corrugated airfoils

The CFD simulations at inflow velocities of 2.71 m/s and 3.47 m/s show a continuous superiority of the corrugated airfoil over the smooth airfoil at positive angles of attack. For both speeds, the corrugated geometry shows much larger lift coefficients, especially in the range of 10°-50° AoA, where the enhancement is of the order of magnitude compared to the smooth profile. For example, the corrugated airfoil gets a lift coefficient of 1.35 at 3.47 m/s and 40° AoA, while the smooth section only reaches 0.13. With more negative lift coefficients, the corrugated airfoil indicates more significant suction effects at negative angles of attack, which may imply more instability at reverse flow. However, the corrugated profile shows significant lift as soon as the angle of attack becomes positive and delays the stall until well beyond 50° keeping a lift coefficient above unity even at 60°. On the other hand, the smooth airfoil exhibits an early stall and restricted lift generation, plateauing near Cl of 0.13.

Table 7: Corrugated vs Smooth Simulation Data Results of Cl vs various AoA @ Inlet Velocity of (a) 2.71 m/s; (b) 3.47m/s

(a) CFD Velocity (m/s)		2.71m/s	(b) CFD Velocity (m/s)		3.47 m/s
Degree	Smooth_Cl	Corrugated_Cl	Degree	Smooth_Cl	Corrugated_Cl
-60	-0.095107204	-0.64257371	-60	-0.095172611	-1.0232802
-50	-0.098678047	-0.63755933	-50	-0.098668656	-1.0322646
-40	-0.088925466	-0.59371281	-40	-0.088715092	-0.94197267
-30	-0.070208926	-0.48078147	-30	-0.069807596	-0.79001967
-20	-0.047691477	-0.34212317	-20	-0.047189793	-0.56228755
-10	-0.023455389	-0.19095611	-10	-0.023114581	-0.31264477
0	0.026256041	0.17485048	0	0.026671683	0.26421975
10	0.094972023	0.57412273	10	0.08295365	0.85443818
20	0.094972023	0.68684928	20	0.095321352	1.0104618
30	0.1125257	0.78384436	30	0.11234681	1.1644396
40	0.12745195	0.86532596	40	0.12741142	1.3512598
50	0.13187887	0.88594058	50	0.13199514	1.392791
60	0.12179117	0.78628504	60	0.12189175	1.219548

The results presented in table 7 illustrate the stall-resistant character of corrugated shapes, which enhance boundary-layer mixing and suppress flow separation. For a higher inflow velocity of 3.47m/s the aerodynamic advantage is further enhanced, since the corrugated airfoil yields a continuously higher lift over the full positive AoA range. This enhanced performance indicates high potential energy capture efficiency for small scale wind turbine applications and implications for better power coefficient (Cp) and annual energy production (AEP).

Table 8: Corrugated vs Smooth Simulation Data Results of Cd and Cl/Cd vs various AoA @ Inlet Velocity of 2.71 m/s

CFD Velocity (m/s)		2.71m/s	Smooth Cl/Cd	Corrugated Cl/Cd
Degree	Smooth_Cd	Corrugated_Cd		
-60	0.17693856	1.144581	-0.538	-0.561
-50	0.13318614	0.82153625	-0.741	-0.776
-40	0.09027798	0.57333725	-0.985	-1.036
-30	0.05497693	0.35132676	-1.277	-1.368
-20	0.02929195	0.18715253	-1.628	-1.828
-10	0.01262744	0.075523679	-1.857	-2.528
0	0.00420493	0.028345237	6.244	6.169
10	0.0312313	0.083243366	3.041	6.897
20	0.0312313	0.22252885	3.041	3.087
30	0.06375846	0.44434929	1.765	1.764
40	0.10462702	0.71711289	1.218	1.207
50	0.15304425	1.0385374	0.862	0.853
60	0.20413645	1.3299519	0.597	0.591

Table 9: Corrugated vs Smooth Simulation Data Results of Cd and Cl/Cd vs various AoA @ Inlet Velocity of 3.47m/s

CFD Velocity (m/s)		3.47 m/s	Smooth Cl/Cd	Corrugated Cl/Cd
Degree	Smooth_Cd	Corrugated_Cd		
-60	0.17685585	1.8199362	-0.538	-0.562
-50	0.13297447	1.3287078	-0.742	-0.777
-40	0.08992176	0.9084426	-0.987	-1.037
-30	0.05459364	0.57592819	-1.279	-1.372
-20	0.02897436	0.30617037	-1.629	-1.837
-10	0.01242264	0.12258412	-1.861	-2.550
0	0.00396184	0.040325788	6.732	6.552
10	0.01145321	0.11913775	7.243	7.172
20	0.03114825	0.32555745	3.060	3.104
30	0.06357245	0.65947464	1.767	1.766
40	0.10448592	1.1190834	1.219	1.207
50	0.1530368	1.6312089	0.863	0.854
60	0.20414488	2.0621581	0.597	0.591

The findings of CFD show the different aerodynamic characteristics of smooth and corrugated airfoils at 2.71 m/s and 3.47 m/s velocities as shown in tables 8 and 9. The corrugated profile always has higher drag coefficients. This leads to higher form drag due to surface imperfections and vortex entrapment. At low angles of attack (0-10°) it provides similar or better lift to drag ratios, which means a delayed stall and a better low speed performance as shown in table 8. The corrugated airfoil reaches a maximum of around 10° at 2.71 m/s, but at 3.47 m/s, the smooth airfoil barely edges it out. Both types are comparably efficient at the moderate angles (20-40°), then drop off precipitously over 50°, where drag is dominant. Both have poor performance at negative angles, with the corrugated surfaces showing worse results. In summary, corrugation can improve the stability of lift and stall resistance at low speeds, but also has a drag cost at high speeds, which makes it suited for small-scale or low-speed wind turbine applications.

4.3. Fluid-structure interaction results

Lift creation through fluid-structure interaction is started in section 4.3. When the air flow approaches the airfoil, figure 71, at different angles of attack, it becomes faster on the top side and slower on the bottom side. The difference in velocity produces a difference in pressure, lower above and higher below, that produces aerodynamic loading on the structure. The airfoil deforms elastically a small amount, changing its camber and effective angle of attack. This structural change changes the flow field, increasing the pressure differential and maintaining lift. The continuous interaction between fluid forces and structural response creates the dynamic equilibrium needed to maintain steady lift production in aerodynamic systems. Lift generation in airfoils arises from the coupled dynamics of fluid–structure interaction. Aerodynamic loading in the form of pressure and velocity fields produces structure deformation which in turn affects the flow field. This bidirectional link assures that the lift is a function not only of fluid mechanics, but also that of the structural reaction of the airfoil, especially in the presence of strong pressure gradients, regions of adverse pressure and the beginning of stall.

4.3.1. Velocity contours at various angle of attack

The velocity magnitude contours from CFD simulations for different angles of attack, demonstrating the fluid-structure interaction, are presented in Figure 70. According to (Khalid 2022), the leading edge is where the stagnation point occurs, resulting in zero velocity.

Figure 70 reveals significant insights into the fluid flow above and underneath the corrugated airfoil, as indicated by the velocity contour. It displays the acceleration and deceleration of air around a corrugated airfoil. The velocity fluctuation at various angles of attack is also shown.

The red zone near the top indicates peak velocity which is where the flow is most accelerated due to curvature and angle of attack.

Figure 71 (a) illustrates that at a zero angle of attack, the velocity contours are symmetrical, however at a 10^0 angle of attack, the stagnation point shifts significantly towards the trailing edge along the bottom surface, consistent with the findings of Patel et al. (2014).

However, there is a gradual change in the velocity variation, meaning that the velocity gradually increases as it approaches the upper surface at the leading edge. Fluid flows more quickly on the upper surface, but when the angle of attack increases, the highest velocity is observed nearer the upper surface's leading edge. Higher velocity is achieved the more the angle of attack is raised (Ghose et al. 2024).

Color	Interpretation
	High-speed flow over upper surface
	Moderate flow, possibly near stagnation zones
	Low-speed flow, wake or separation on zones

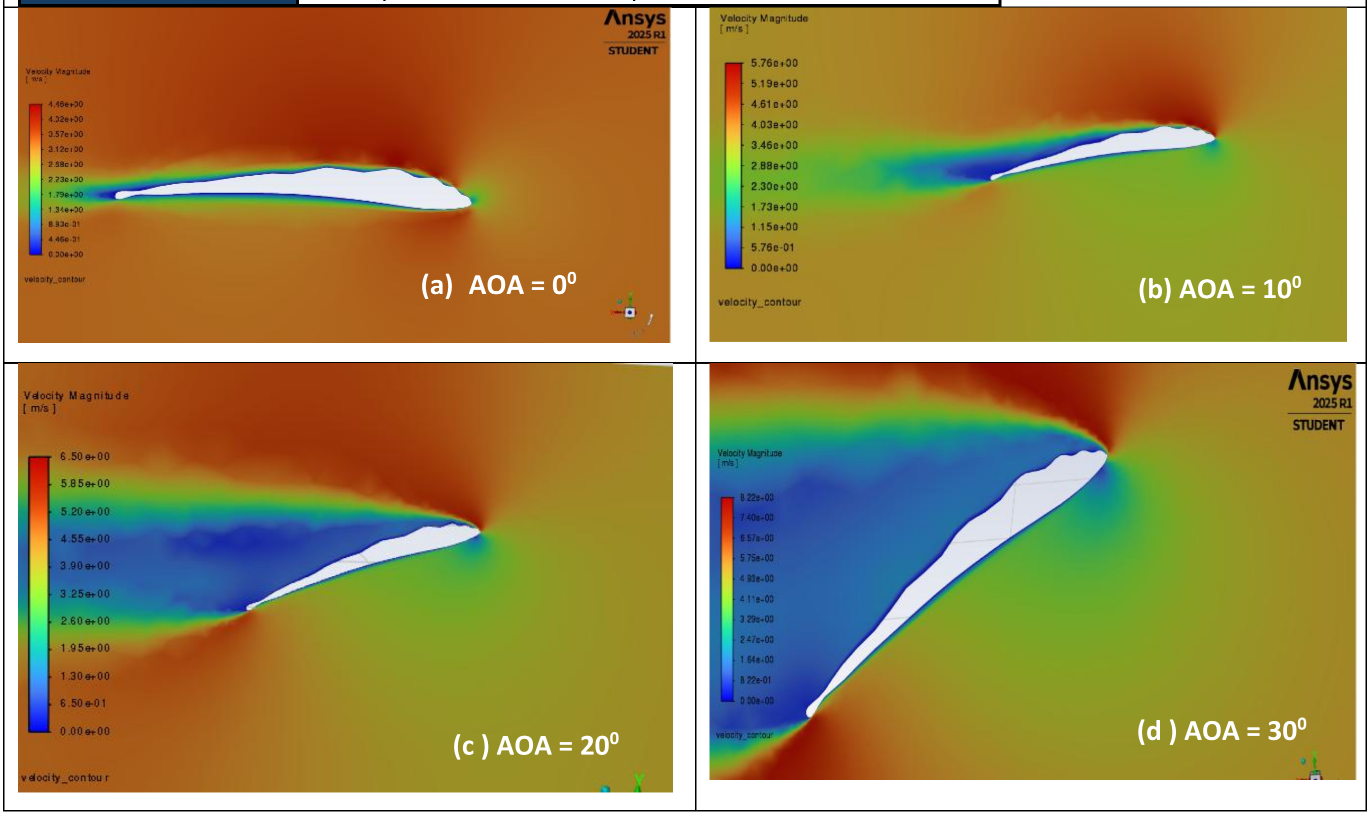

Figure 71: Velocity contour including velocity contour indication at AoA (a) 0^0, (b) 10^0, (c) 20^0 and (d) 30^0

The configuration of the cambered corrugated airfoil is such that the fluid flow over its upper surface is significantly greater than that over its lower surface, even at a zero angle of attack. Nonetheless, the air consistently interacts with the surface at the exact leading edge, where velocity is null, and this position might be described as a stagnation point. The angle of attack influences the stagnation point (Ghose et al. 2024). The stagnation points shift away from the leading edge on the lower surface with increasing positive angles of attack and moves away from the leading edge on the upper surface with increasing negative angles of attack. As the angle of attack increases, according to Ayon Sarkar et al. (2025) the fluid flow across determines that at angle of attack at 5^0 -10^0, velocity vectors show acceleration on the upper surface. At 20^0 angle of attack, Ayon Sarkar et al. (2025) continues to show larger-scale flow separation occurring, leading to stall condition. The same can be experience in this study at the same angle of attack.
However, there is a gradual change in the velocity variation, meaning that the velocity gradually increases as it approaches the upper surface at the leading edge. Fluid flows more quickly on the upper surface, but when the angle of attack increases, the highest velocity is observed nearer the upper surface's leading edge. The lower surface exhibits reduced velocity, causing the stagnation point to shift from the precise leading edge to a position further from the leading edge as the angle of attack rises. An increased angle of attack results in a higher velocity near the leading edge as reported by Ghose et al. (2024).

The trailing edge conforms to the Kutta condition, which asserts that "A body with a sharp trailing edge moving through a fluid generates a circulation of adequate strength to maintain the rear stagnation point at the trailing edge." A stagnation point forms at the trailing edge as the flow pattern converges from both above and below, meets at the corner, and then diverges from the body. The fluid flows less smoothly across the corrugated airfoil's upper surface as the angle of attack rises; that is, the flow's separation point shifts from the trailing edge to the leading edge. Additionally, the flow is separated at the critical angle, or maximum lift condition, and as the critical angle rises, the flow was completely divided, and the lift coefficient will drop even more sharply. Above the crucial angle, the airplane must be in stall. The velocity drop near the trailing edge (especially on the lower surface) could indicate the flow deceleration or mild separation and potential wake formation, which contributes to drag.

The airflow surrounding the corrugated airfoil is shown to accelerate and decelerate from 0.82 m/s (dark blue) to 8.28 m/s (dark red) at a 30-degree angle of attack. On the upper surface (red/orange), the airflow speeds up considerably, peaking close to the leading edge and in the chord's center. Low pressure is seen in the high-speed flow, supporting Bernoulli's theory(Ghose et al. 2024). This demonstrates a significant lift generation.

Higher pressure is indicated by a slower flow on the lower surface of the corrugated airfoil, which is colored blue or green. Upward lift is caused by the pressure difference between the top and bottom surfaces. There are no indications of stall or separation, and the leading edge accelerates smoothly above and decelerates below, suggesting connected flow. In summary, the corrugated airfoil's upper surface exhibits high velocity flow (red), which results in low pressure and suction. Low velocity (blue/green) on the corrugated airfoil's lower surface indicates high pressure, or compression. The trailing edge displays a smooth flow exit with a gradual velocity recovery.

4.3.2. Pressure contours at various angle of attack

Figures 72 show the pressure magnitude contours produced by CFD simulations at various angles of attack. This is an indication of the fluid-structure interaction. Bernoulli's principle states that high velocity correlates with low pressure (Khalid 2022). Similarly, high pressure at the bottom pushes the geometry upward, producing the lift force, while low pressure at the top due to higher velocity.

The operating conditions were set according to the ones of wind tunnel experiments. Pressure was atmospheric, temperature was normal and Reynolds number, inlet velocity and air viscosity of the test was indicated. Visualizing the contours for various parameters is crucial for analysing the current aerodynamic behaviour relative to the corrugated airfoil which is the indication of fluid-structure interaction process. It's critical to observe how air pressure affects the corrugated airfoil.

According to Patel et al. (2014), at 0^0 angle of attack, the pressure contours over an airfoil exhibit symmetry between the upper and lower sections, with stagnation occurring precisely at the leading edge of the corrugated airfoil. At 0^0 AoA shows the leading edge with high static pressures. The red region at the leading edge shows maximum static pressure, where the airflow stagnates and slows down upon impact. This is the stagnation point and is an important region to understand how the corrugated airfoil is redirecting the flow.

Pressure lowers from red to green to deep blue as the flow accelerates over the curved upper surface as demonstrated by Ayon Sarkar et al. (2025). The minimal pressure (blue region at the mid-chord) is important for lift generation (Patel et al. 2014). This pressure reduction is caused by the higher velocity according to Bernoulli's principle. The lower surface retains higher pressure predominantly in green and light blue tones as indicated by Patel et al. (2014).

Color	Interpretation
(red)	Stagnation point, high pressure
(green)	Freestream and lower surface
(dark blue)	Suction peak, low-pressure zone

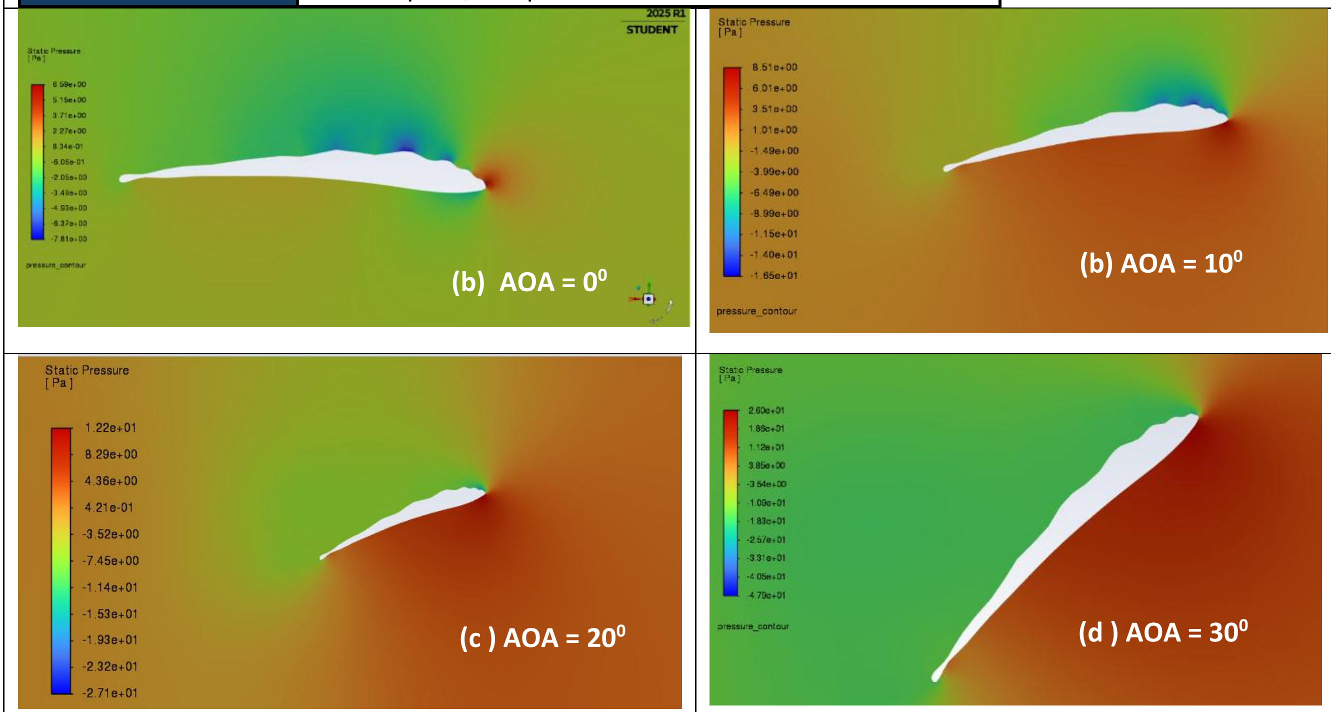

Figure 72: Pressure contour including pressure contour indication at AoA (a) 0^0, (b) 10^0, (c) 20^0 and (d) 30^0

Here the pressure gradient is not as sharp. The boundary layer is more stable and there is less acceleration than the higher surface. The wake at the trailing edge indicates a minor pressure recovery in the region behind the airfoil with the greenish yellow hues. These trends indicate slower flow and perhaps moderate separation that causes pressure drag. In the near future the camber, thickness or leading-edge radius will be altered in order to optimize the pressure distribution and decrease the drag for best results.

High pressures of about 26 Pa are found close to the leading edge on the bottom area at 10^0 angle of attack. This trend suggests a severe standstill in which airflow slows down and constricts. By pressing upward on the airfoil, this area makes a substantial contribution to positive lift. There is a low-pressure area of around 0.47 Pa and lower at the upper surface, particularly close to the chord's center and leading edge. The airfoil is drawn upward by this suction effect, which increases lift. The airfoil itself, which serves as the border between the high- and low-pressure zones, is the white area. Lift is produced by the abrupt pressure differential across the surface. The main source of lift is the pressure difference between the higher and lower surfaces. Smooth tapering of pressure gradients indicates minimal wake turbulence on the trailing edge and effective flow departure.

This pressure contour from your CFD simulation shows how a pressure differential at a 20-degree angle of attack produces lift. Dark red (+12.2 Pa) and dark blue (-27.1 Pa) are at opposite ends of the color spectrum. This wide range reveals a notable pressure differential throughout the corrugated airfoil. Low pressure predominates on the upper surface (Blue/Green), particularly in the vicinity of the leading edge. This differential pressure shows that the air flow is accelerated in accordance with Bernoulli's principle. A major factor in positive lift is the suction effect. Higher pressure is visible on the bottom surface (red/orange), particularly close to the leading edge's stagnation point. Here the air slows down and compresses, shoving the airfoil upwards. Clearly the pressure field is not symmetrical with compression below and extra suction above. The difference in pressure indicates that the airfoil is producing net upward lift. No indications of stalling. The constant and smooth pressure contours imply connected flow.

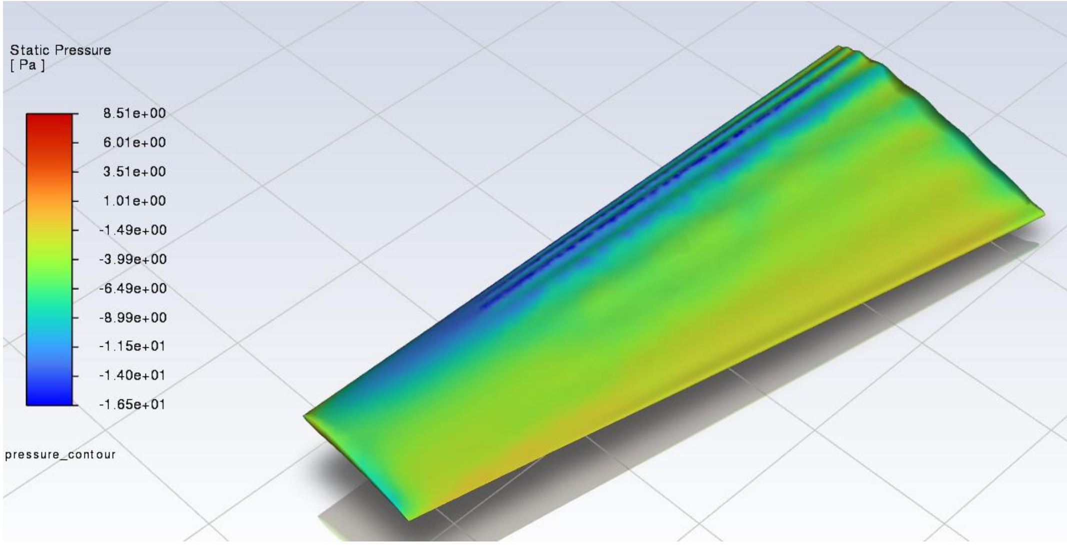

Figure 73: Pressure Contour at 10^0 on the corrugated Airfoil

Looking closely at the corrugated surface on figure 73, it can be shown that the corrugated surface causes low pressure. It creates localized acceleration zones. The valleys and ridges of the corrugation act like mini ducts. As air flows over these undulations, it gets channelled and squeezed, which increases its velocity as reported by Zhang et al. (2025). According to Bernoulli's principle, higher velocity leads to lower static pressure. Corrugations can trap small vortices in the valleys. These vortices help energize the boundary layer, delaying separation and maintaining attached flow as reported by Zhang et al. (2025). The effect on corrugation surface was summarized on the table 10. The swirling motion also contributes to local pressure reduction, especially near the suction peaks. The structural compliance ensures the surface adapts to these pressure fluctuations rather than resisting them rigidly. The alternating curvature of the corrugated surface causes pressure gradients that mimic the effects of camber. On the upper surface, this enhances the suction effect, further reducing pressure as noted by Zhang et al. (2025).

Table 10: The Corrugation Effect and Benefits on the Airfoil Surface (Zhang et al. 2025)

Features	Effect	Benefits
Corrugation valleys	Accelerated flow → low pressure	Increased lift
Vortex trapping	Stabilized boundary layer	Reduced drag, delayed separation
Pressure gradient shaping	Enhanced suction	Better aerodynamic efficiency

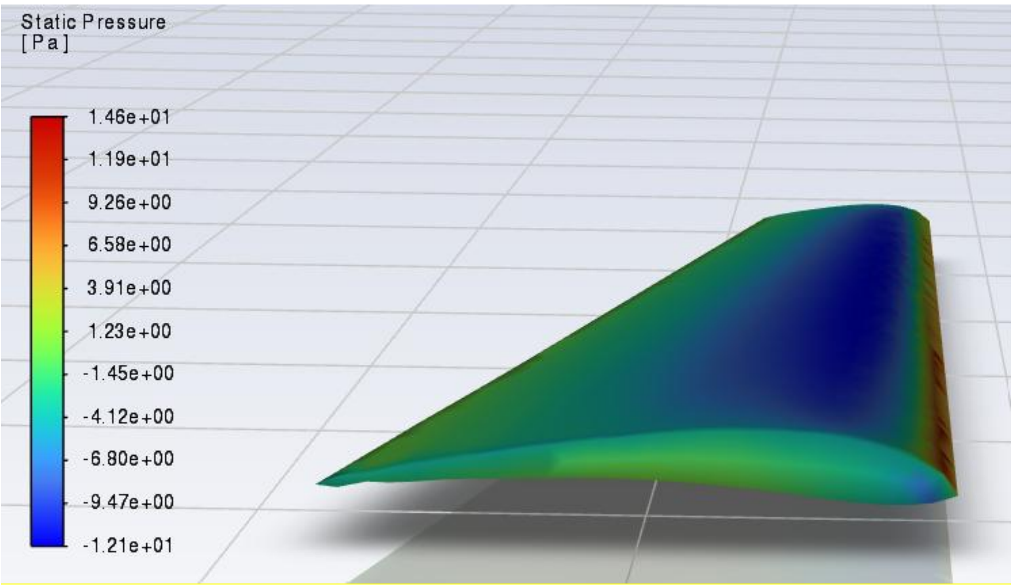

Figure 74: Pressure Contour at 0^0 on the smooth Airfoil

The corrugated airfoil has a peculiar pressure distribution which allows it to act adaptively aerodynamically. Alternating high- and low-pressure zones along the upper surface excite the boundary layer, delaying flow separation and stabilizing lift. The lower surface has a more uniform pressure with small elevations around the corrugation valleys increasing lift. This geometry causes micro vortices which allow for flow attachment and aerodynamic efficiency of the airfoil at greater angles of attack. The smooth airfoil on figure 74 on the other hand has a much simpler pressure gradient with a strong low-pressure region near the leading edge and a gradual recovery towards the trailing edge. Its lower surface pressure is not dynamic but quiescent. The smooth profile on figure 74 is predictable, but less flexible and leads to earlier stall and greater drag after the onset of separation. The corrugation generally enhances the lift stability and delays stall due to fluid-structure interaction, while the smooth airfoil gives steady but less efficient performance.

4.4. Lift and drag coefficients against angle of attack

The computed lift coefficients for an angle of attack between -60^0 and 60^0 are displayed in Figure 75. The graph suggests that CL increases in tandem with an increase in the angle of attack. However, after 50^0, the CL decreases as the angle of attack increases. Fluid separation occurs as a result of pressure forces overcoming the fluid's inertial forces due to the high-pressure gradient. The drop in CL with an increase in AoA is caused by this fluid separation.

Khalid (2022) shows the same pattern of increase Cl with increase in AoA but certainly decreases as the angle of attack increases.

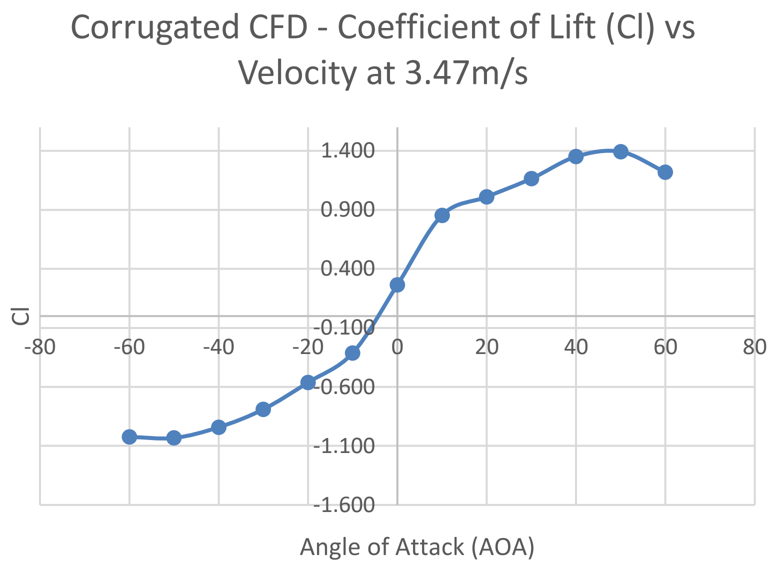

Figure 75: CFD Lift Coefficient values at different angles of attack

The computed drag coefficients for an angle of attack between -60^0 and 60^0 are displayed in Figure 76. The graph suggests that CL increases in tandem with an increase in the angle of attack. However, after 50^0, the CL decreases as the angle of attack increases. Fluid separation occurs as a result of pressure forces overcoming the fluid's inertial forces due to the high-pressure gradient. The drop in CL with an increase in AoA is caused by this fluid separation. Khalid (2022) shows the same pattern of increase Cl with increase in AoA but certainly decreases as the angle of attack increases.

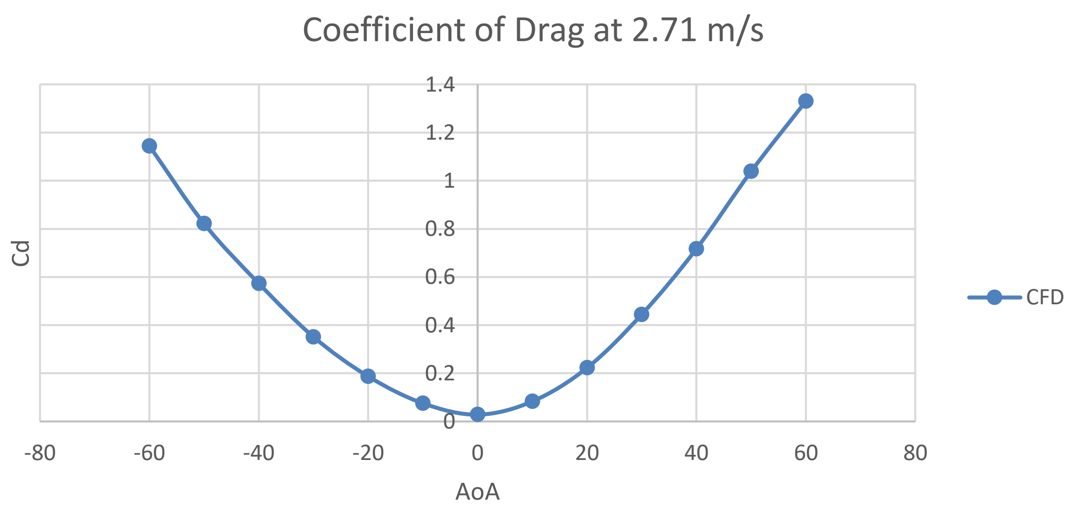

Figure 76: CFD Drag Coefficient values at different angles of attack

According to Isyaku Kunya et al. (2024), the drag curve of the traditional airfoil drag coefficient rises with angle of attack up to 15^0 and then continues to rise in a straight line up to the final angle (25^0). The bumpy airfoil model's drag curve exhibits a similar tendency to the conventional one, with the exception that the bumpy airfoil has higher drag coefficients between 5^0 and 20^0 AoA. For both models, the lowest and maximum drag coefficients are roughly 0.03 at 0^0 AoA and 0.44 at 25^0 AoA, respectively. Following (figure 76) drag curve, the similar trend can be seen but with higher anger of attack, the drag coefficient keeps on rising.

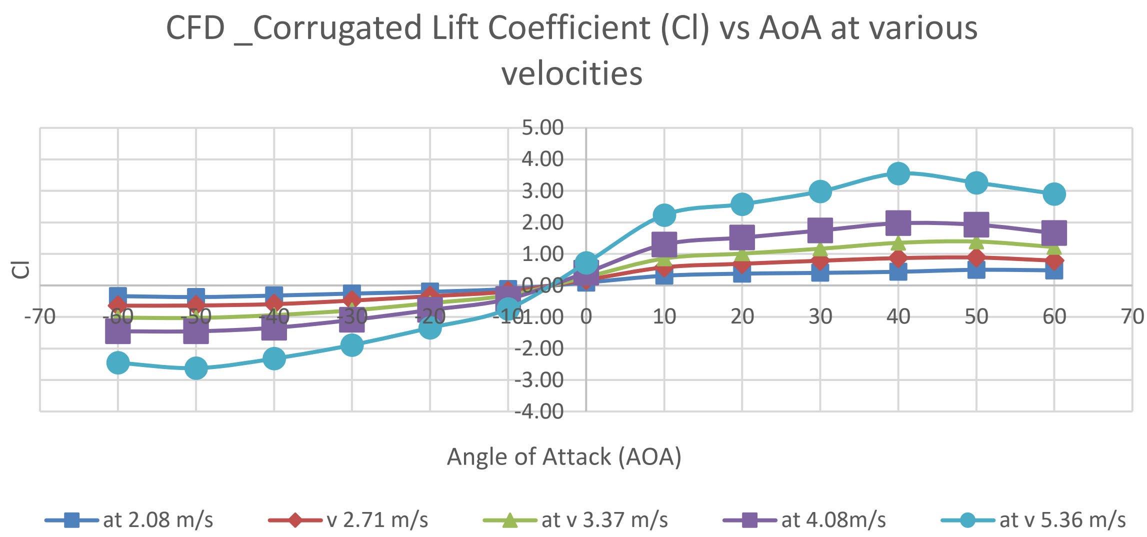

Figure 77: Summary of all Coefficients of Lift against Angle of Attack

Table 11: Velocity behaviour against coefficient of lift vs angle of attack

Velocity (m/s)	Maximum Coefficient of lift	Angle of attack at max Cl	Post stall behavior	Comment
2.08	0.495	50	Gradual	Low Reynolds number; smoother separation
2.71	0.89	50	Moderate	Slight increase in lift and sharper drop
3.47	1.39	50	Steeper	More pronounced peak and stall
4.08	1.97	40	Abrupt	High lift, aggressive post-stall decline
5.36	3.6	40	Very Abrupt	Highest lift; sharpest stall behavior

The lift coefficient data on figure 77 of CFD at velocities of 2.00 m/s to 5.36 m/s is consistent with the aerodynamics pattern: Cl increases with angle of attack (AOA) to a maximum at 40 degrees, then drops after stall. The peak Cl values increase drastically with increasing velocity reaching almost 4.0 at 5.36 m/s . This tendency is caused by an increase in lift at higher Reynolds numbers, probably because of larger pressure differentials and delayed separation. However, the post-stall behaviour becomes more and more abrupt with velocity, which indicates that the flow separation becomes more and more important and might be beyond the resolution capability of the turbulence treatment in the CFD model (Isyaku Kunya et al. 2024).

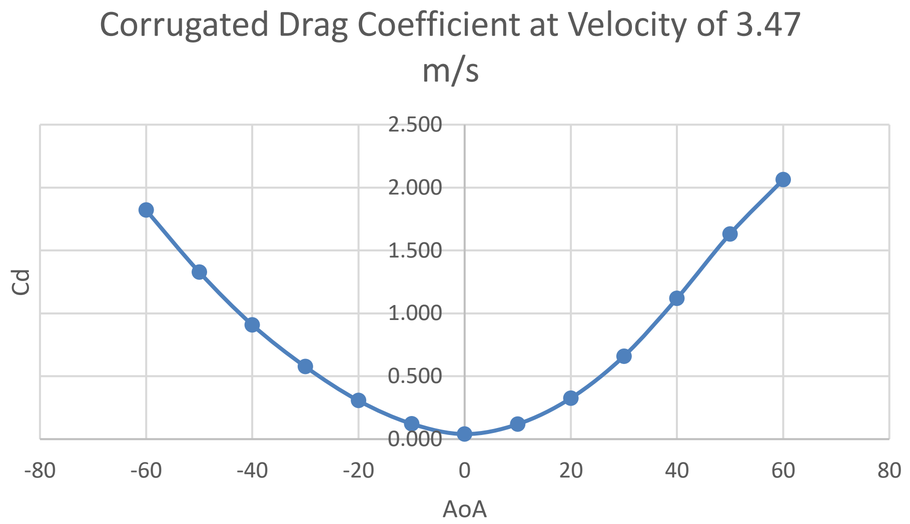

Figure 78: Drag Coefficient against angles of attack

According to Patel et al. (2014) , similarly, the drag coefficient is 0 at zero AOA, increases gradually until the stall state, and then increases quickly both during and after the stall, as Figure 78 illustrates.

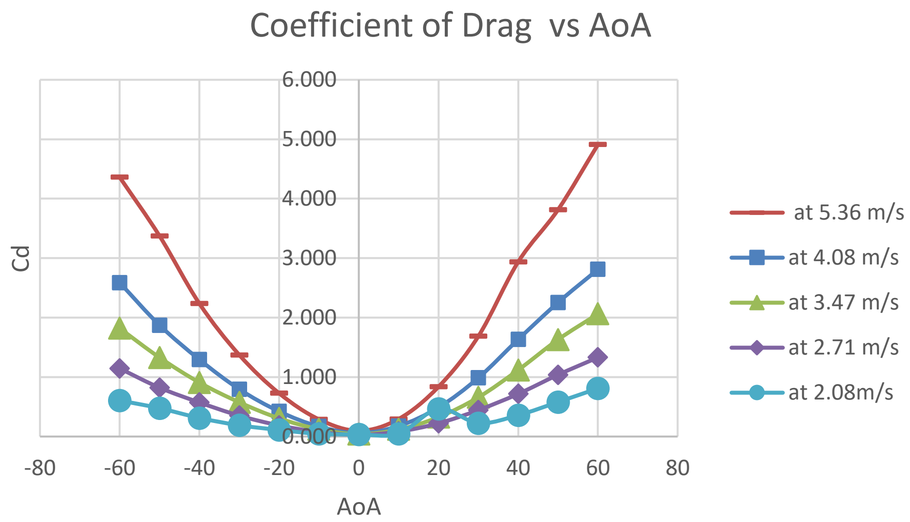

Figure 79: Overall Drag Coefficient values against angles of attack for various velocities

Figure 79, all curves are symmetric about 0° AoA, confirming expected pressure drag behaviour. As velocity rises, both the minimum and maximum Cd values increase, reflecting the growing influence of pressure drag and turbulent wake formation. This scaling behavior underscores the aerodynamic cost of operating at high AoA under high-speed conditions and highlights the importance of modelling corrugated airfoil geometry to balance lift generation with drag penalties. Ayon Sarkar et al. (2025) demonstrate that after 20^0 angle of attack, lift drastically decreases and drag increases.

4.5. Inlet velocity on aerodynamic characteristic across angle of attack

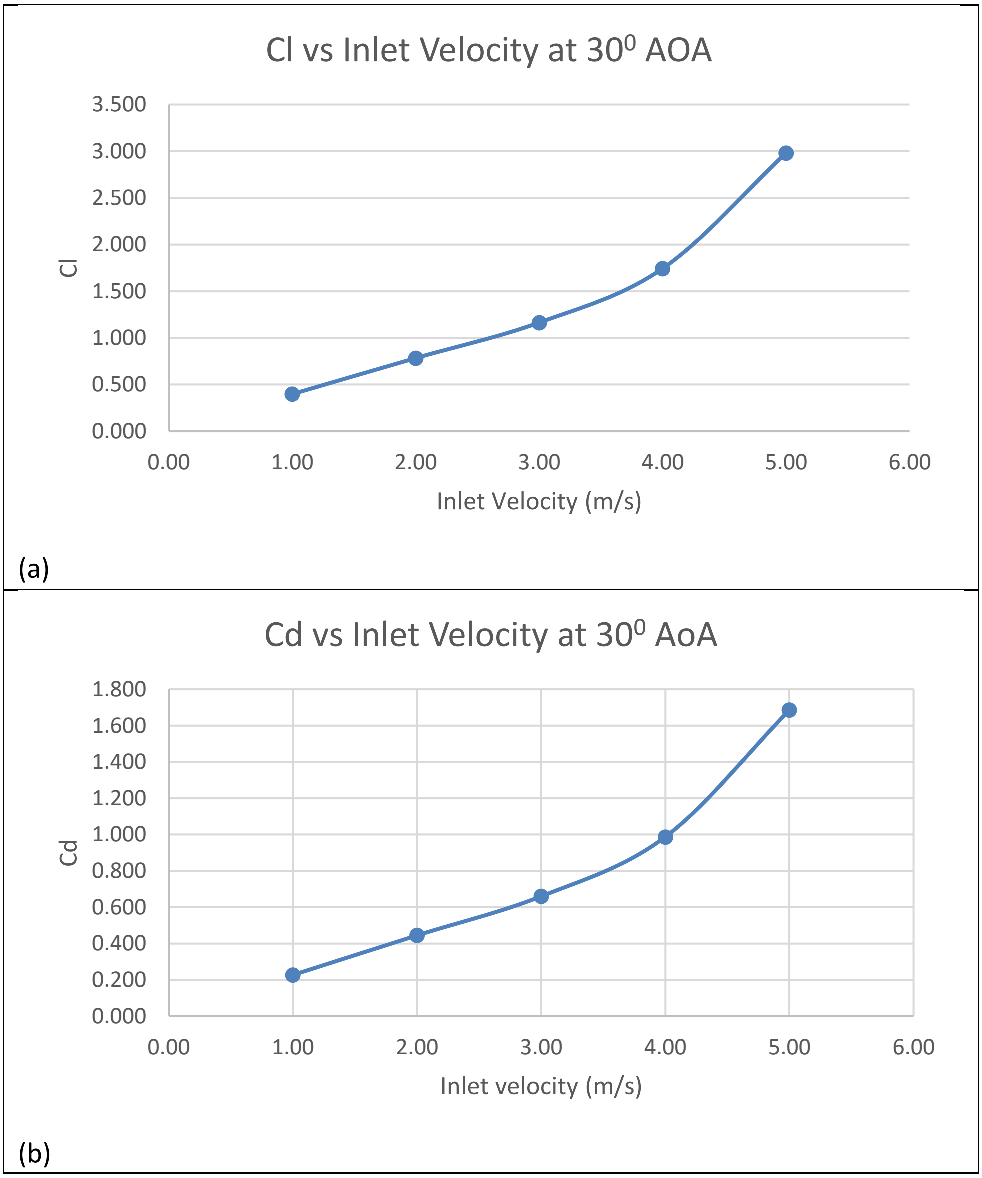

Figure 80: (a) Cl against inlet velocity at AoA of 30 and (b) Cd against Inlet Velocity at Aoa of 30^0

Iqbal et al. (2025) shows that Cl and Cd increase as inlet velocity. The lift coefficient (Cl) increases nonlinearly with inlet velocity at a constant AOA of 30°. Cd increases nonlinearly with inlet velocity. Higher velocities intensify pressure drag and flow separation, especially at high AOA as shown on figure 80.

Both graphs have a parabolic shape, meaning that the curves (CL and Cd) increase and do so at a fast rate as shown in Iqbal et al. (2025).

4.6. Discussion on lift-to-drag coefficient ratio as a function of angle of attack

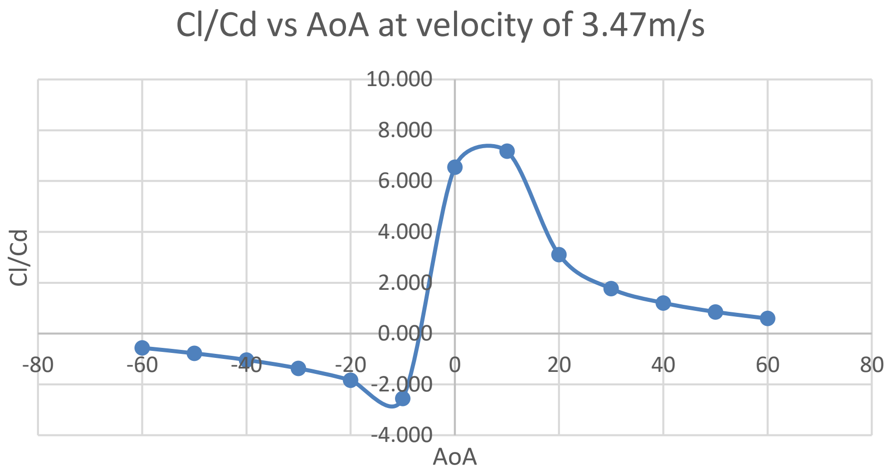

Figure 81: Cl/Cd ratio against AoA at inlet velocity of 3.47 m/s

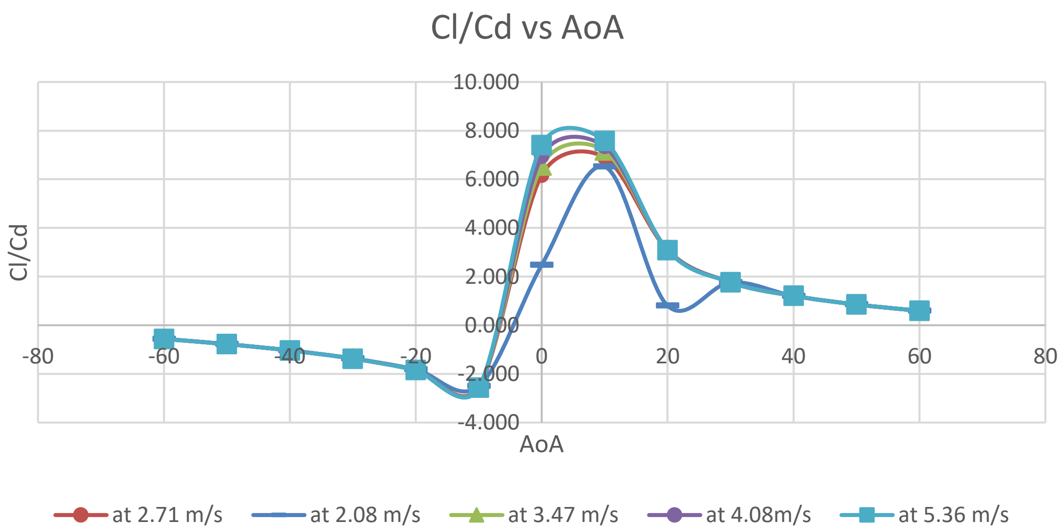

Figure 82: Cl/Cd ratio against AoA at various inlet velocities

Looking at figures 81 and 82, all curves peak between 10^0 – 20^0 angle of attack, confirming this as the optimal operating range. As velocity increases, peak Cl/Cd decreases lift gains are offset by rising drag, especially at higher Reynolds numbers. These graphs shows that the corrugated airfoil operating near 15^0 angle of attack at lower velocities yields the best lift-to-drag ratio.

4.7. Smooth vs Corrugated airfoil Lift and Drag Comparisons

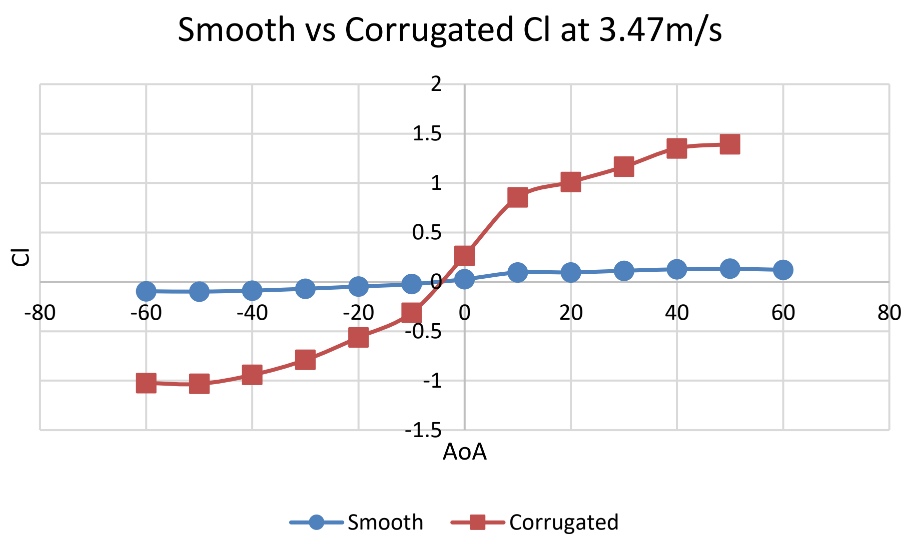

Figure 83: Smooth and Corrugated Cl against AoA at 3.47m/s

Looking at figure 83, the corrugated surface introduces micro-vortices that energize the boundary layer, keeping the flow attached longer. The delayed stall is evident from the extended lift curve before decline the airfoil maintains lift up to higher angles of attack. The smooth airfoil, by contrast, shows limited lift generation and no adaptive. The corrugated airfoil delayed stall and enhanced lift at low velocity as shown by a flattening curve of the smooth airfoil. Its adaptive geometry through fluid–structure interaction allows better aerodynamic efficiency, especially useful for low Reynolds number applications like micro air vehicles or small wind turbines response to flow changes.

4.8. Airfoil effect on annual energy production

4.8.1. Power Coefficient Cp results of smooth against corrugated airfoil at 2.71m/s and 3.47m/s

Table 12: Power Coefficient Cp results of smooth against corrugated airfoil at 2.71m/s and 3.47m/s

			CFD Velocity (m/s)		2.71m/s	
CFD Velocity (m/s)		2.71m/s	Smooth Cl/Cd	Corrugated Cl/Cd	Smooth Cp	Corrugated Cp
Degree	Smooth_Cd	Corrugated_Cd				
-60	0.17693856	1.144581	-0.538	-0.561	-0.081	-0.084
-50	0.13318614	0.82153625	-0.741	-0.776	-0.111	-0.116
-40	0.090277982	0.57333725	-0.985	-1.036	-0.148	-0.155
-30	0.054976925	0.35132676	-1.277	-1.368	-0.192	-0.205
-20	0.029291952	0.18715253	-1.628	-1.828	-0.244	-0.274
-10	0.012627437	0.075523679	-1.857	-2.528	-0.279	-0.379
0	0.004204932	0.028345237	6.244	6.169	0.937	0.925
10	0.031231298	0.083243366	3.041	6.897	0.456	1.035
20	0.031231298	0.22252885	3.041	3.087	0.456	0.463
30	0.063758464	0.44434929	1.765	1.764	0.265	0.265
40	0.10462702	0.71711289	1.218	1.207	0.183	0.181
50	0.15304425	1.0385374	0.862	0.853	0.129	0.128
60	0.20413645	1.3299519	0.597	0.591	0.089	0.089

			CFD Velocity (m/s)		3.47 m/s	
CFD Velocity (m/s)		3.47 m/s	Smooth Cl/Cd	Corrugated Cl/Cd	Smooth Cp	Corrugated Cp
Degree	Smooth_Cd	Corrugated_Cd				
-60	0.17685585	1.8199362	-0.538	-0.562	-0.081	-0.084
-50	0.13297447	1.3287078	-0.742	-0.777	-0.111	-0.117
-40	0.089921759	0.9084426	-0.987	-1.037	-0.148	-0.156
-30	0.054593635	0.57592819	-1.279	-1.372	-0.192	-0.206
-20	0.028974357	0.30617037	-1.629	-1.837	-0.244	-0.275
-10	0.012422639	0.12258412	-1.861	-2.550	-0.279	-0.383
0	0.003961836	0.040325788	6.732	6.552	1.010	0.983
10	0.011453213	0.11913775	7.243	7.172	1.086	1.076
20	0.031148254	0.32555745	3.060	3.104	0.459	0.466
30	0.063572454	0.65947464	1.767	1.766	0.265	0.265
40	0.10448592	1.1190834	1.219	1.207	0.183	0.181
50	0.1530368	1.6312089	0.863	0.854	0.129	0.128
60	0.20414488	2.0621581	0.597	0.591	0.090	0.089

Looking at the table 12, The calculated Cp of greater than 0.593 will be regarded as non-physical. Kimiti et al. (2024) mentioned that the Betz limit states that the maximum theoretical power coefficient $C_p$for a wind turbine is about 0.593 (59.3%), meaning no turbine can extract more than 59% of the kinetic energy from wind. Both the corrugated and smooth airfoil achieved their peak power at 20^0 AoA. The corrugated airfoil Cp outperformed the smooth airfoil in both 2.71m/s and 3.47m/s speed. This confirms that corrugation improves stall resistance, lift generation and energy capture efficiency.

4.8.2. Power output and Annual Energy Production (AEP)

Equation 5 on page 50 shows the power output equation as $P(v) = \frac{1}{2}\rho A v^3 C_p$, with 1.225kg/m3 air density, 3.47m/s and T = total hours in a year = 24*365 = 8760 hours

Swept are = $A = \pi R^2 = \pi(0.5)^2 = 0.785\ \text{m}^2$ (13)

For Smooth Airfoil is $P(v) = \frac{1}{2}\rho A v^3 C_p$ = 0.5*1.225*0.785*3.47^3*0.459 = 9.36W

For Corrugated Airfoil is $P(v) = \frac{1}{2}\rho A v^3 C_p$ = 0.5*1.225*0.785*3.47^3*0.466 = 9.36W

$$AEP = \int_0^\infty P(v) \cdot f(v)\, dv \cdot T \quad (14)$$

(Verma 2020; Seguro & Lambert 2000) has given an estimated Weibull parameters k (shape factor) = 2 and c (scale factor) = 4 shown in equation 15, to demonstrate AEP.

The probability density at 3.47m/s is $\boldsymbol{f(v)} = \frac{\boldsymbol{k}}{\boldsymbol{c}}\left(\frac{v}{c}\right)^{\boldsymbol{k-1}} \boldsymbol{e}^{-(v/c)^{\boldsymbol{k}}}$ = 0.21 (15)

Table 13: Power Coefficient Cp results and AEP of smooth against corrugated airfoil at 3.47m/s

Velocity m/s	AoA	Smooth Cp	Corrugated Cp	Smooth Power output P(v) (W)	Corrugated Power output P(v) (W)	Smooth AEP (kWh/year)	Corrugated AEP (kWh/year)
3.47	20^0	0.459	0.466	9.226	9.358	16.518	16.753

Table 13 shows the comparison of the aerodynamics and power output of smooth and corrugated airfoils at 3.47 m/s velocity and 20° angle of attack demonstrates the effect of the blade shape. The streamlined airfoil gave a power coefficient (Cp) of 0.459, with a power output of 9.226 W and an annual energy production (AEP) (equation 14) of 16.518 kWh/year. The corrugated airfoil had a higher somewhat C p of 0.466, which resulted in 9.358 W and annual energy production (AEP) of 16.753 kWh/year. The difference in AEP is small (1.4%) however the corrugated profile always harvests the better energy. This incremental advantage is essential over a long-time horizon, because small efficiency gains translate into large annual production increases. The results demonstrate the viability of using corrugated shapes to improve performance at low to moderate wind speeds, suggesting a practical technique to optimize small-scale wind turbine designs within the theoretical limits imposed by the Betz limit.

4.9. Summary of chapter 4

In this chapter, corrugated and smooth GOE174 airfoil aerodynamic performance results were discussed using CFD software ANSYS Fluent at various angles of attack from -60^0 to 60^0 with a constant velocity ranging from 2 – 5.36m/s. The smooth airfoil results are lower than the corrugated ones. The same goes to the Cl/Cd results at 3.47 m/s of corrugated airfoil against smooth airfoil.

CHAPTER 5: WIND TUNNEL EXPERIMENTAL RESULTS VALIDATION AGAINST CFD RESULTS

5.1. Introduction

Chapter four explored the CFD results and its discussion in detail. The use of CFD simulation was validated by smooth airfoil and it has to be validated by the wind tunnel experiment results in this chapter. This chapter compares CFD results of the corrugated airfoil with those of Wind Tunnel experiment for validation. The coefficients of lift, drag vs angle of attack graphs on both CFD and wind tunnel results are presented and discussed on this chapter.

Chapter 5 is organized into four key sections to present and discuss the comparison on the CFD and wind tunnel experiment results.

First section details the data results collected during experiment followed by a discussion of their implications. The second section presents graphical results illustrating the variation of lift and drag coefficient with respect to the angle of attack, proving insights into aerodynamic performance between CFD and wind tunnel experiment. The influence of inlet velocity on aerodynamic characteristic across angle of attack as compared to CFD behaviour is highlighted on section three of this chapter.

Lastly the analyzation of the lift-to-drag coefficient ratio as a function of angle of attack, offering a comparative metric for aerodynamic efficiency between CFD and wind tunnel experiment.

5.2. Wind tunnel coefficient of lift results

(Ansari et al. 2022)defined lift as a force generated by pressure distribution around the airfoil, whereas drag is described as an aerodynamic force that is parallel to the fluid flow and opposes the object's motion. The preceding chapter indicated that the wind tunnel used has some of the limitations on the angle of attack (AoA) ranges from -20^0 to 20^0.

5.2.1. Coefficient of lift versus angle of attack in wind tunnel experiments

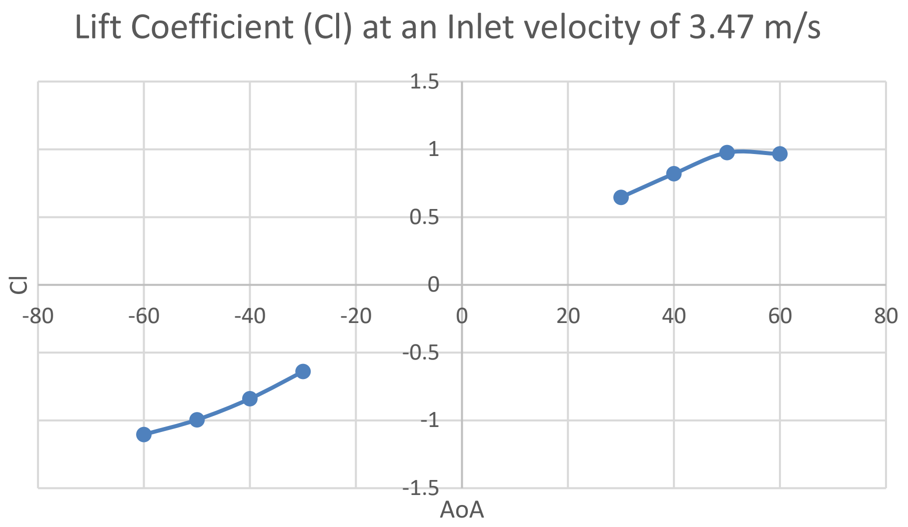

Figure 84: Wind Tunnel Experiment Coefficient of Lift vs AoA at 3.47 m/s

The lift coefficients against angle of attack between -60^0 and 60^0 are displayed in Figure 84. The graph indicates that the coefficient of lift (CL) rises with an increase in the angle of attack. Nonetheless, beyond 50^0, the coefficient of lift diminishes as the angle of attack escalates. Fluid separation occurs as a result of pressure forces overcoming the fluid's inertial forces due to the high-pressure gradient. The drop in CL with an increase in AoA is caused by this fluid separation. A similar study by Khalid (2022) shows the same pattern of increase Cl with increase in AoA but certainly decreases as the angle of attack increases.

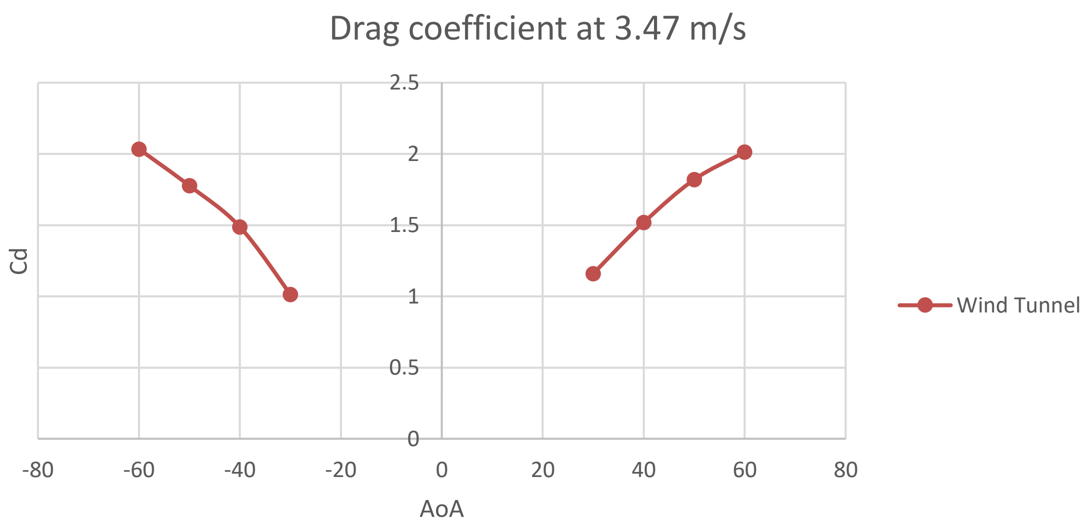

Figure 85: Wind Tunnel Experiment Coefficient of drag vs AoA at 3.47 m/s

Figures 84 and 85 demonstrate that when the angle of attack of the corrugated airfoil increases, both CL and CD rise, consistent with the findings of Ghose et al. (2024). As per Ghose et al. (2024), the drag coefficient (CD) escalates exponentially after 10^0, while the lift coefficient (CL) diminishes after 10^0. The ideal CL to CD ratio occurs at an angle of attack of 5^0. With an increase in the angle of attack, a pronounced backflow across the upper surface near the trailing edge is noted. The stagnation spots shift towards the lower surface from the tip as the angle of attack increases as reported by Ghose et al. (2024). In examining figures 84 and 85, both Cl and Cd consistently exhibit an upward trend. The constraint of the wind tunnel's angle of attack, ranging from -20^0 to 20^0, presents a gap that can be addressed in future research.

5.3. Comparison of lift coefficients versus angle of attack

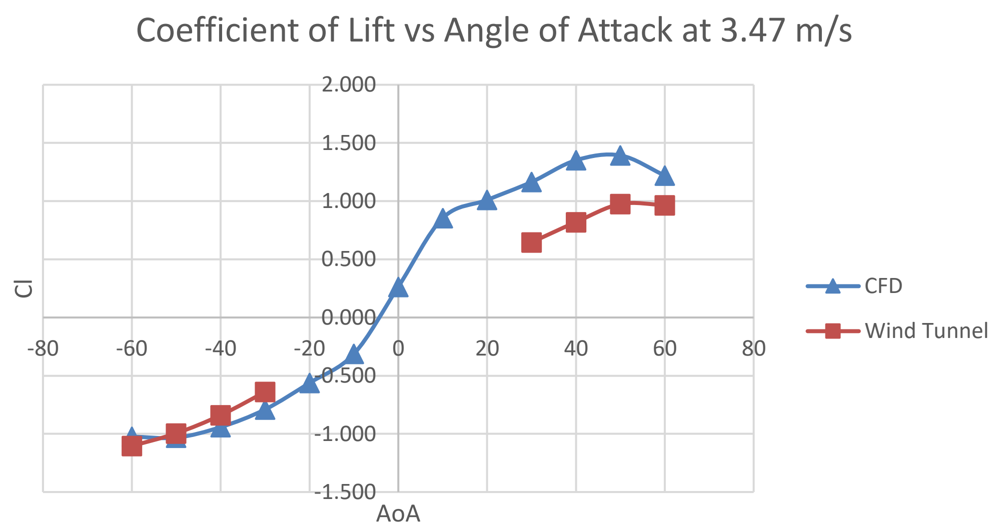

Figure 86: Comparison of CFD and Wind Tunnel Coefficient of Lifts against Angle of Attack at 3.47 m/s

Figure 86 illustrates the comparison between simulation outcomes and wind tunnel experimental findings. Both results are showing an expected trend. The experimental findings corroborate the outcomes derived from the simulation in this study. Looking at figure 84, it compares the results of CFD simulations (blue colour) with real data from wind tunnels (red colour) to illustrate how the lift coefficient (Cl) changes with angle of attack (AOA) at a speed of 3.47 m/s. It is evident that CFD produces a gradual rise in Cl with a positive AoA, peaking at 1.39 at an AoA of roughly 50^0, this could be due to idealised boundary conditions and absence

of real-world surface effects. At AoA -60^0, the Cl exhibits a comparatively straight trend, dropping to roughly -1.004. The CFD captures more data while the wind tunnel is limited due to limitations in the channel mentioned in chapter 1 of this study. A simplified flow model with few stall or separation effects is depicted by the symmetric, progressive CFD curve.
The wind tunnel data show that Cl increases to 0.975 at AOA 50^0 at positive AOA, albeit with less steepness and more scatter than CFD. Stronger negative lift and more noticeable flow separation are indicated by the significant reduction in Cl to about -1.104 at a negative AOA which is almost the same as CFD results. Turbulence, stalls, and vortex shedding are examples of real-world complications that are reflected in the wind tunnel data presented by Zhang et al. (2025). The validation or summary of the results are displayed on table 14.

Table 14: Validation on CFD results vs Wind Tunnel Experiment at 3.47 m/s

Description	CFD Results	Wind Tunnel Results	Comment
Maximum Coefficient Cl	1.393	0.975	CFD overpredicts by approximately 0.4; typical due to idealized flow assumptions
Angle of Attack and Max Cl (degrees)	50	50	Good agreement in stall onset location
Post- stall Cl drop	sharp	gradual	CFD shows more abrupt stall; wind tunnel reflects real flow separation
Low angle of attack behavior (less than -50)	More negative	Less negative	CFD predicts stronger reverse lift; may reflect turbulence model limits
Overall trend agreement	strong	strong	Both shows expected Cl vs AOA curve shape

5.4. Comparison coefficient of drag against angle of attack

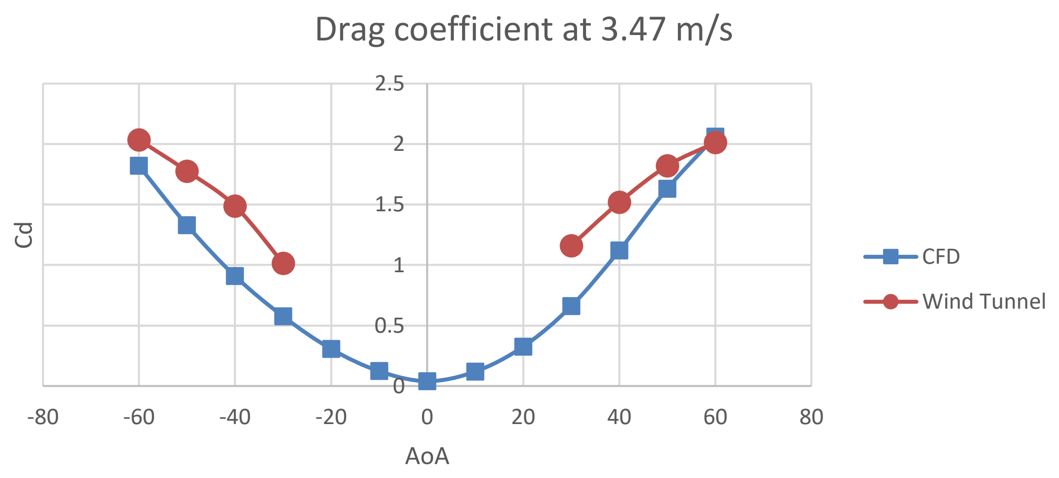

Figure 87: Coefficient of Drag vs AoA at 3.47 m/s

Looking at figure 87, with a speed of 3.47 m/s, the drag coefficient (Cd) distribution throughout the angles of attack (AOA) is still asymmetric parabolas for both CFD and wind tunnel data, which is consistent with the aerodynamic theory. The CFD model predicts decreased drag for low angles and much higher peak drag especially for extreme angles. These inconsistencies are probably due to idealized flow conditions and limits in turbulence models, in particular the ability to capture flow separation and wake dynamics. The CFD model, although quantitatively different, reproduces the overall drag trend and confirms its usefulness for preliminary aerodynamic assessments when experimental data are not available. The rapid increase of CD is mainly caused by the strong backflow at the trailing edge of the corrugated airfoil, which increases abruptly with an increase of angle of attack. Consequently, after a specific angle of attack, the CL increment rate drops as observed by Ghose et al. (2024).

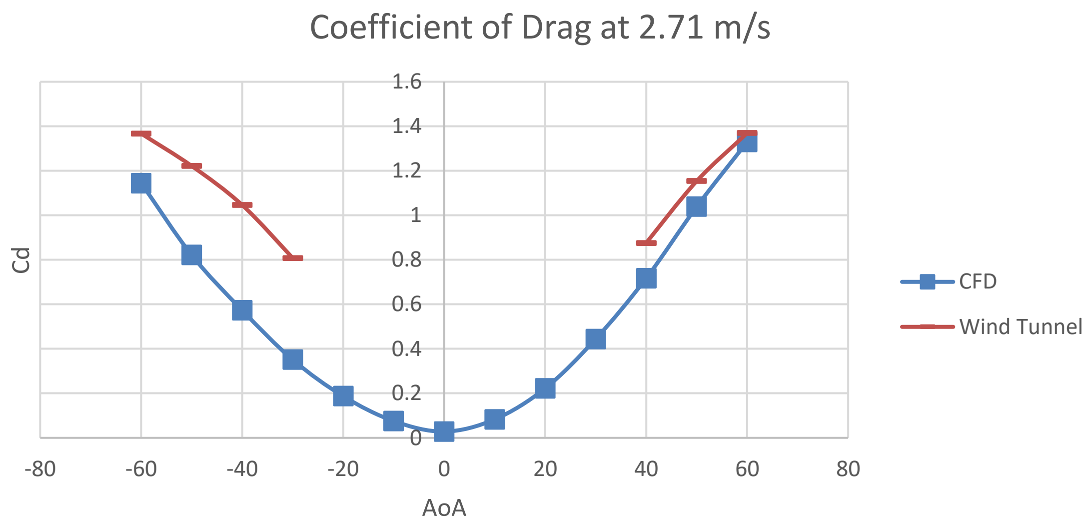

Figure 88: Coefficient of Drag vs AoA at 2.71 m/s

Figure 88, at a test velocity of 2.71 m/s, the drag coefficient (Cd) variation with angle of attack (AOA) shows strong qualitative agreement between CFD and wind tunnel data. Both datasets exhibit a symmetric parabolic trend cantered around 0°, consistent with expected aerodynamic behaviour. The CFD model predicts slightly lower drag at lower AOA and overestimates peak drag values at higher AoA which may stem from idealized surface conditions, and the absence of flow disturbances present in experimental setups.

At extreme AoA, CFD underpredicts drag more noticeably than at lower speeds, which could be attributed to increased Reynolds number effects and limitations in turbulence modelling (e.g., RANS smoothing out unsteady separation).

According to Akbari (2022) the lift coefficient increases with the angle of attack from 0^0 to 15^0 but drops from 15^0 to 20^0 as the angle of attack increases. Akbari 2022 mentioned that, for negative attack angles ranging from 0^0 to -15^0, increasing the angle of attack results in a decrease in the lift coefficient, which subsequently stabilizes at a constant value. Figure 86 illustrates that the drag coefficient consistently rises with increasing angles of attack from 0^0 to 20^0 and from 0^0 to -20^0. Akbari (2022) illustrates a comparable trend in both lift and drag coefficients relative to angle of attack, as depicted in figures 15 (page 28) and 19 (page 30) of the literature review chapter.

5.4.1. Validation of wind tunnel cl/cd vs angle of attack against CFD results

Wind tunnel testing is essential for confirming aerodynamic enhancements realized through novel blade profiles and design attributes as reported by Animasaun & Adeniran (2025). Researchers can set up controlled airflow conditions to study aerodynamic forces such as lift and drag on scaled or full-size blade components or complete rotors (Animasaun & Adeniran 2025). These experimental results provide a baseline for the validation of CFD models (Animasaun et al. 2025). Figures 89-93 show the comparison of CFD and wind tunnel data for the lift-to-drag coefficient ratio change with the angle of attack for the inlet velocities ranging from 2.081 m/s to 5.36 m/s. Initially, the Cl/Cd curve seems to ascend as the angle of attack rises. At the apex, the slope transitions from growing to zero, thereafter commencing a descent. The comparison indicates that the Cl/Cd plot exhibits peaks at a ratio of around 7 for an angle of attack between 0^0-20^0, thereby affirming the best angle for aerodynamic efficiency. Ayon Sarkar et al. (2025) present the results of a simulation illustrating the impact of varying angles of attack on the aerodynamic characteristics of an airfoil. Ayon Sarkar et al. (2025) continue to demonstrate that at an angle of attack between 5^0 and 10^0, substantial lift is generated due to a favourable pressure gradient, with the boundary layer remaining attached and exhibiting minimal flow deviation. This resembles the present study.

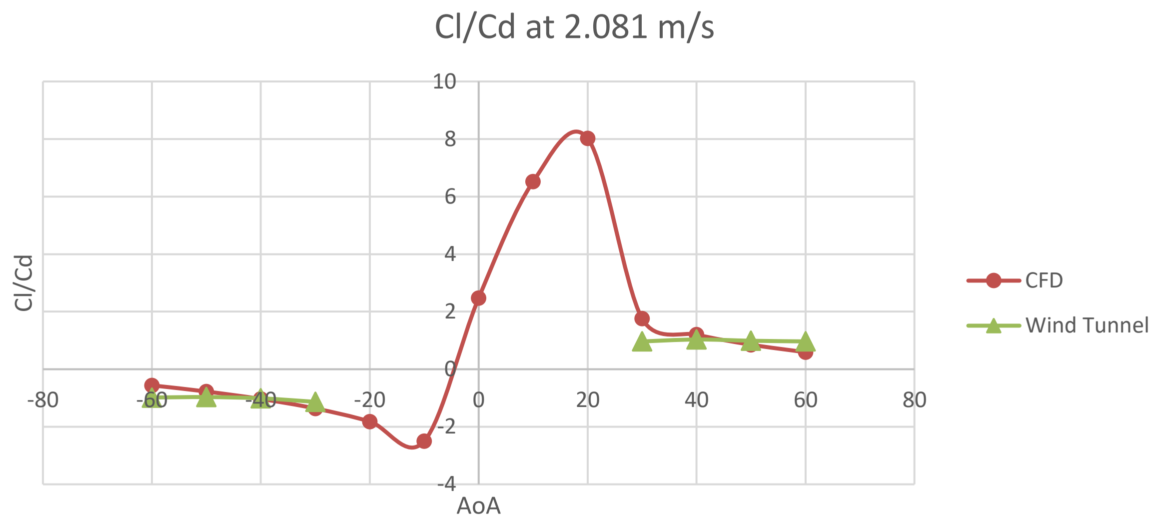

Figure 89: Cl/Cd vs AoA at 2.081 m/s

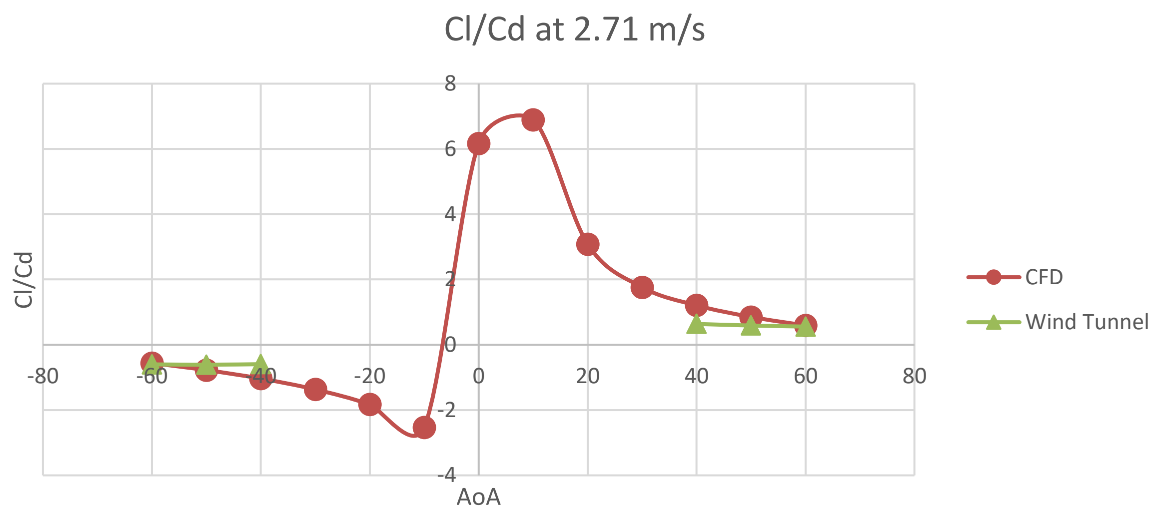

Figure 90: Cl/Cd vs AoA at 2.71 m/s

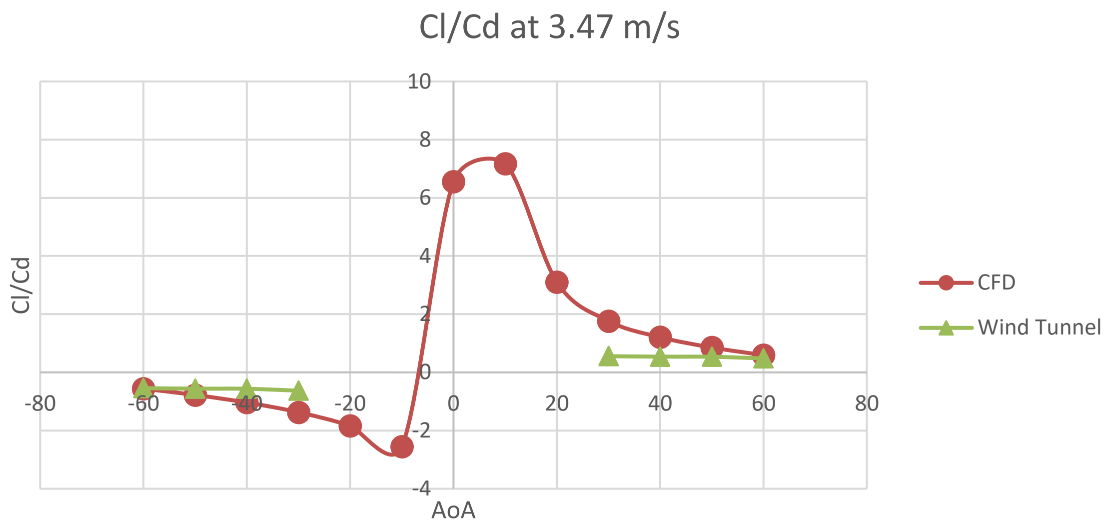

Figure 91: Cl/Cd vs AoA at 3.47 m/s

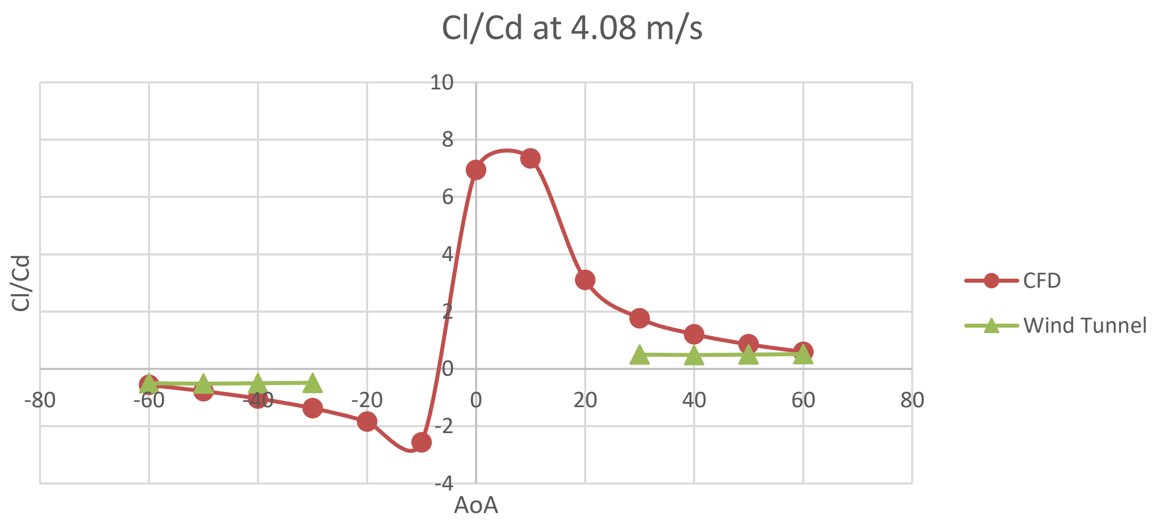

Figure 92: Cl/Cd vs AoA at 4 m/s

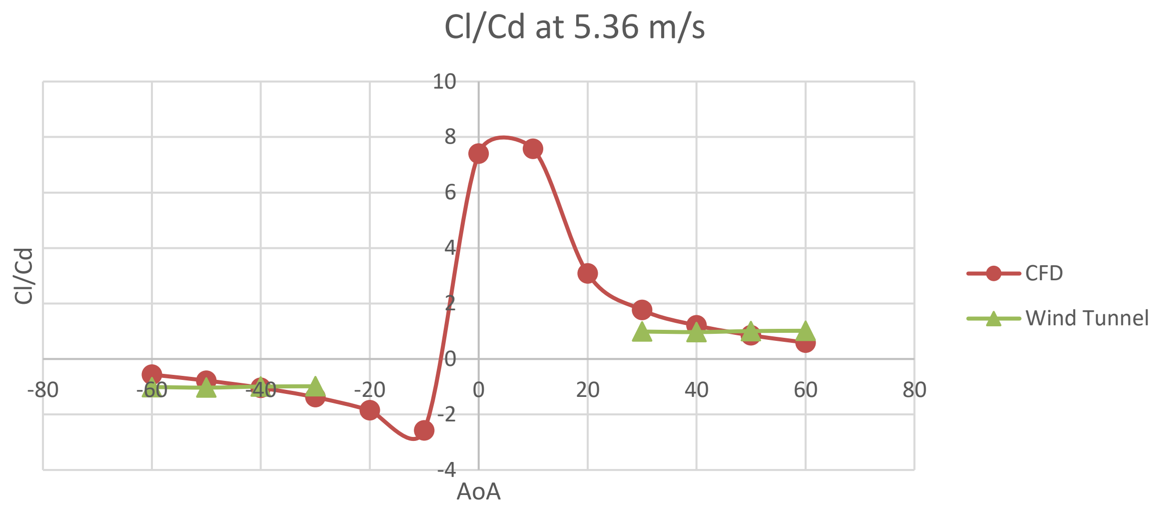

Figure 93: Cl/Cd vs AoA at 5.36 m/s

Wind Tunnel data lacks the pronounced peak due to measurement limitations. More data results are shown on Annexure A and B of this study.

5.4.2. Quantified error analysis

Following tables 15 -17 are the CFD and Wind tunnel coefficient of lift results were used to calculate variance and standard deviation in order to quantify the error.

n	CFD_{CL}	WT_{Cl}	$(WT_{Cl}-CFD_{Cl})$	$(WT_{Cl}-CFD_{Cl})^2$
1	-0.647	-0.340	-0.306798241	0.094125161
2	-0.561	-0.369	-0.191921024	0.036833679
3	-0.480	-0.322	-0.157711999	0.024873075
4	-0.376	-0.258	-0.117466583	0.013798398
5	0.360	0.399	-0.038371409	0.001472365
6	0.487	0.433	0.053680138	0.002881557
7	0.566	0.495	0.071201389	0.005069638
8	0.607	0.479	0.128025064	0.016390417

Table 15: CFD and Wind Tunnel Coefficients of lifts at v=2.08m/s

n	CFD_{CL}	WT_{Cl}	$(WT_{Cl}-CFD_{Cl})$	$(WT_{Cl}-CFD_{Cl})^2$
1	-1.0232802	-1.10441	-0.08113	0.006582788
2	-1.0322646	-0.99521	0.037054	0.001372967
3	-0.94197267	-0.83984	0.102134	0.010431437
4	-0.79001967	-0.63915	0.15087	0.022761787
5	1.1644396	0.646099	-0.51834	0.268676664
6	1.3512598	0.820025	-0.53124	0.282210818
7	1.392791	0.975394	-0.4174	0.174220516
8	1.219548	0.965758	-0.25379	0.064409428

Table 16: CFD and Wind Tunnel Coefficients of lifts at v=3.47m/s

n	CFD_{CL}	WT_{Cl}	(WT_{Cl}-CFD_{Cl})	(WT_{Cl}-CFD_{Cl})^2
1	-2.4551	-2.58132	-0.12622	0.015930461
2	-2.62374	-2.26209	0.361654	0.130793471
3	-2.32282	-1.93272	0.390106	0.152183045
4	-1.88921	-1.50217	0.387036	0.149797015
5	2.981369	1.475541	-1.50583	2.26751966
6	3.551597	1.841112	-1.71049	2.925759843
7	3.260163	2.319406	-0.94076	0.885022708
8	2.905136	2.647966	-0.25717	0.066136063

Table 17: CFD and Wind Tunnel Coefficients of lifts at v=5.36m/s

Where variance of errors can be computed as:

$$\boldsymbol{\sigma^2} = \frac{\sum(\boldsymbol{WT_{C_L}} - \boldsymbol{CFD_{C_L}})^2}{\boldsymbol{n}} \quad (16)$$

And Standard deviation will be $\sqrt{\sigma^2}$

The following table 18 is the summary of variance and standard deviation among the three velocities 2.08 m/s, 3.47m/s and 5.36m/s

Velocity (m/s)	**Variance**	**Standard Deviation**
2.08	0.0244	0.156
3.47	0.104	0.322
5.36	0.824	0.908

Table 18: Summary of the variance of errors with standard deviation for velocities 2.08 m/s, 3.47 m/s and 5.36m/s

Both variance and standard deviation increase with velocity, showing greater divergence between CFD and wind tunnel results at higher speeds. The models align closely for a low velocity of 2.08 m/s. At 5.36 m/s the differences are more pronounced, possibly due to turbulence, flow separation or experimental sensitivity.

Analysis of variance and standard deviation of lift coefficient data from CFD and wind tunnel for velocities of 2.08 m/s, 3.47 m/s and 5.36 m/s. The results indicate increasing scatter with velocity, suggesting a larger discrepancy between numerical predictions and experimental evidence at high flow speeds. This tendency indicates that the aerodynamic performance is quite sensitive to turbulence and flow separation effects, especially for velocities higher than 3 m/s. The comparison of the CFD and wind tunnel lift coefficient data for the three test velocities shows a clear rise in variability with increasing flow speed. At 2.08 m/s, the variation and standard deviation are minimal, indicating a strong alignment between numerical predictions and experimental outcomes. At 3.47 m/s the deviation grows, showing a significant divergence indicating the appearance of flow instabilities or sensitivity to boundary conditions. With a velocity of 5.36 m/s the variance and standard deviation increase rapidly. This shows the large differences that are probably caused by turbulence, flow separation and experimental uncertainty. The progressive increase shows the limited ability of the CFD models to capture the complex aerodynamic phenomena at higher velocities and highlights the significance of experimental validation for credible forecasts of performance.

5.5. Summary of chapter 5

From these data, the large velocity differential between the higher and lower surfaces validates the effective lift. All curves show the same form trend of Cl versus AoA: lift increases with AoA up to a maximum and then drops off due to stall. The stall point moves somewhat with velocity, while the peak Cl increases with speed. The constant trend in speed indicates that the CFD setup (mesh, turbulence model, boundary conditions) is stable and well calibrated. As velocity increases, so does Reynolds number, which stabilizes the boundary layer and delays stall reflected in higher peak Cl and smoother post-stall curves. The consistent trend across speeds suggests that CFD setup (mesh, turbulence model, boundary conditions) is stable and well-tuned.

CHAPTER 6: CONCLUSION AND RECOMMENDATIONS FOR FURTHER RESEARCH

The last chapter presents the conclusion of the research investigation. Includes limitations of the study, outcomes, and recommendations for future investigation.

6.1. Conclusion

The work presented in this study has enhanced the aerodynamic performance of a Horizontal Axis Wind Turbine (HAWT) through the design and testing of a bio-inspired corrugated airfoil, based on the albatross wing profile and compare it with the smooth one. The basic goals of identification of suitable blade geometry, development and simulation of 3D corrugated model and validation of the results through computational and experimental means have been achieved. Results indicate that corrugated NACA GOE174 airfoil inspired by avian wing structures has better aerodynamic performance for a variety of angles of attack as compared to the smooth airfoil.

The corrugated airfoil has a small efficiency advantage over the smooth profile at 3.47 m/s wind speed and 20° angle of attack. The smooth blade yields a power coefficient (Cp) of 0.459 with a matching power output of 9.226 W. The corrugated blade yields Cp = 0.466 and 9.358 W. Annualized for a realistic wind distribution, this corresponds to an Annual Energy Production (AEP) of roughly 16.518 kWh/year for the smooth airfoil and 16.753 kWh/year for the corrugated airfoil. The corrugated geometry shows consistently higher energy collection, although the absolute difference is minor (1.4%), indicating its potential to remain aerodynamically effective at moderate wind speeds. The benefit is minor but incremental and important for long-term operation as fractional improvements in Cp can add up to large gains in annual production. These results improve the chances of corrugated designs to enhance performance in low to moderate wind regimes.

In summary, the research achieves its aims by showing that corrugated bio-inspired airfoil designs have a favorable impact on HAWT performance by boosting lift, delaying stall and maintaining aerodynamic stability as compared to the smooth airfoil. The key practical implication is that such bio-inspired designs could be implemented in real-world wind turbine blades, potentially leading to increased energy capture and operational efficiency, especially under variable wind conditions.

6.1 Recommendation and future work

For better findings in CFD models, following future studies should be included:

a) Investigate performance in larger wind tunnel and field experiments using 3D-printed corrugated blades
b) Incorporate aeroelastic modelling to assess deformation effects on lift and Cp
c) Further studies on the CFD setup and refinement on the Meshing could bring more better results.
d) Investigate the large-scale application of bio-inspired, corrugated blades on working wind turbines, to evaluate real-world advantages, including enhanced structural robustness and longevity under varying wind conditions.

Further investigation of these issues in future work will contribute to a better understanding and realization of the practical importance and greater applicability of bio-inspired, corrugated airfoil concepts for wind energy.

REFERENCE

Adeel-Ur-Rehman, A, Theron, JN, Kassem, H, Stoevesandt, B & Peinke, J. 2024. Improved performance of k - ω SST turbulence model in predicting airfoil characteristics for a wide range of airfoil thicknesses. In: *Journal of Physics: Conference Series*. V. 2767. Institute of Physics. doi.org/10.1088/1742-6596/2767/2/022064.

Akbari, P. 2021. Study of NACA 6212 Airfoil and Investigation of its Aerodynamic Properties in Different Angles of Attack. *10.37628/IJMDA*. 7. doi.org/10.37628/IJMDA.

Amjith, LR & Bavanish, B. 2020. Design and analysis of 5 MW horizontal axis wind turbine. In: *Materials Today: Proceedings*. V. 37. Elsevier Ltd. 3338–3342. doi.org/10.1016/j.matpr.2020.09.202.

An, W, Shi, F, He, S, Wang, W, Zhang, H & Liu, L. 2021. Aerodynamic Design and Optimization of Bionic Wing Based on Wandering Albatross. In: *Proceedings of the International Conference on Aerospace System Science and Engineering 2020*. Z. Jing & X. Zhan, Eds. Singapore: Springer Singapore. 517–535.

Animasaun, A & Adeniran, AO. 2025. Optimization of Wind Turbine Performance through Advanced Materials and Design. doi.org/10.22105/opt.v2i1.69.

Ansari, SA, Kohar, N, Karthik, K & Bishwakarma, S. 2022. *Design and Analysis of Fluid Flow and Aerodynamic Forces on NACA 4412 Airfoil Using CFD*. Available from: http://ymerdigital.com.

ANSYS Inc. 2024. *Fluent theory guide*. Available from: https://ansyshelp.ansys.com/public/account/secured?returnurl=////Views/Secured/corp/v242/en/flu_th/flu_th.html.

Aqilah, F, Islam, M, Juretic, F, Guerrero, J, Wood, D & Ani, FN. 2018. Study of mesh quality improvement for CFD analysis of an airfoil. *IIUM Engineering Journal*. 19(2):203–212. doi.org/10.31436/iiumej.v19i2.905.

Asadi Ali. 2016. *CFD Workflow: How to Set Up a Fluid Dynamics Analysis_SimScale*. Available from: https://www.simscale.com/blog/cfd-workflow-quick-guide/ [Accessed 27 February 2026].

Ayon Sarkar & Vikash Kumar Mahto. 2025a. Computational_Analysis_of_Flow_Character. (July).

Ayon Sarkar & Vikash Kumar Mahto. 2025b. Computational Analysis of Flow Characteristics over NACA4412 Airfoil using CFD simulation at varying Angles of Attack. *IJIRT 182929*. 12 Issue 2(ISSN: 2349-6002).

Badran, O, Azad, Z, Virk, M, Masalha, I & Alahmer, A. 2025. Aerodynamic Performance Evaluation of the NACA 65-421 Airfoil Using CFD and the k-ω SST Turbulence Mode. In: *Proceedings of the*

SSDM 2025 SME Aerospace Structures, Structural Dynamics, and Materials Conference. The Westin Houston, Memorial City Houston, TX, USA. 1–10.

Biswas, S & Chen, JSJ. 2025. Power Coefficient for Large Wind Turbines Considering Wind Gradient Along Height. *Energies*. 18(3). doi.org/10.3390/en18030740.

Cabanillas Sánchez, V. 2013. Blade performance analysis and design improvement of a small wind turbine for rural areas. UPC, Escola Universitària d'Enginyeria Tècnica Industrial de Terrassa. Available from: https://upcommons.upc.edu/entities/publication/9a205d25-ead5-4aad-870b-cf5237495ce5.

Dwivedi, YD & Vashishta, B. 2023. *Bio-inspired green concept of albatross bird wing for high fuel efficiency*. Available from: https://www.researchgate.net/publication/375746957.

Edibon. 2013. *PRACTICAL EXERCISES MANUAL*. Available from: https://www.edibon.com/en/computer-controlled-wind-energy-turbine-fundamentals-unit [Accessed 21 May 2026].

Faraihan Zulkefli, N, Fathin Adlina Syed Abdullah, S, Mohd Nur, N & Yet Heng, J. 2016. *Wind Tunnel Evaluation on the Performance of Blown Airfoil*. Available from: www.ireee.net.

Gaitan-Aroca, J, Sierra, F & Contreras, JUC. 2020. Bio-inspired rotor design characterization of a horizontal axis wind turbine. *Energies*. 13(14). doi.org/10.3390/en13143515.

Gao, R, Chen, K, Li, Y & Yao, W. 2021. Investigation on aerodynamic performance of wind turbine blades coupled with airfoil and herringbone groove structure. *Journal of Renewable and Sustainable Energy*. 13(5). doi.org/10.1063/5.0051729.

Ghose, P, Kumar Sahoo, T, Kumar Patel, J, Kumar Nayak, S & Kumar Rana, B. 2024. Drag lift characteristics of a NACA 4412 airfoil with angle of attack. In: *Journal of Physics: Conference Series*. V. 2818. Institute of Physics. doi.org/10.1088/1742-6596/2818/1/012002.

Airfoil Tools. n.d. *GOE 174 (Albatros 5020) airfoil (goe174-il)*. Available from: http://www.airfoiltools.com/airfoil/details?airfoil=goe174-il.

Gray, A, Singh, B & Singh, S. 2021. Low wind speed airfoil design for horizontal axis wind turbine. In: *Materials Today: Proceedings*. V. 45. Elsevier Ltd. 3000–3004. doi.org/10.1016/j.matpr.2020.11.999.

Iqbal, MR, Asif, I, Rashid, M, Faiz, MD & Naeem, MisM. 2025. Investigating the lift and drag coefficients of NACA4412 airfoil using cfd simulations. *International Journal of Trendy Research in Engineering and Technology*. 09(04):22–29. doi.org/10.54473/ijtret.2025.9403.

Isyaku Kunya, B, Alhassan, Y, Balarabe, F, Alhaji Ibrahim, M, Isyaku Kunya, S & History, A. 2024. *Numerical Study of Performance of Airfoil with Sinusoidal-Shaped Leading Edge at Low Wind*

Speed ARTICLE INFO ABSTRACT Keywords: Angle of attack · lift coefficient · drag coefficient · bumps · NACA 4412. Available from: www.joset.com.ng.

Jacobs Eastman et al. 1937. *National advisory committee for aeronautics airfoil section characteristics as affected by variations of the reynolds number national i inform a technical*. Available from: https://ntrs.nasa.gov/citations/19930091662 [Accessed 21 May 2026].

Jureczko, M, Pawlak, M & Mężyk, A. 2005. Optimisation of wind turbine blades. *Journal of Materials Processing Technology*. 167(2–3):463–471. doi.org/10.1016/j.jmatprotec.2005.06.055.

Khalid, MH. 2022. CFD Analysis of NACA 0012 Aerofoil to Investigate the Effect of Increasing Angle of Attack on Coefficient of Lift and Coefficient of Drag. *Journal of Studies in Science and Engineering*. 2(1):74–86. doi.org/10.53898/josse2022216.

Khan, MA & Padhy, C. 2021. Aerodynamic characterization of bio-mimicked pleated dragonfly aerofoil. *International Journal of Aviation, Aeronautics, and Aerospace*. 8(2):1–24. doi.org/10.15394/ijaaa.2021.1562.

Khan, SA, Bashir, M, Baig, MAA & Ali, FAGM. 2020. Comparing the effect of different turbulence models on the CFD predictions of NACA0018 airfoil aerodynamics. *CFD Letters*. 12(3):1–10. doi.org/10.37934/cfdl.12.3.110.

Kimiti, RM, Kariuki, FN, Kamau, JN & Soitah, TN. 2024. Theoretical and Empirical Limits: Reexamining Betz’s Upper Limit towards a Practical Power Coefficients in Wind Turbines[*]. *World Journal of Engineering and Technology*. 12(04):851–866. doi.org/10.4236/wjet.2024.124052.

Liu, Y, Li, P, He, W & Jiang, K. 2020. Numerical study of the effect of surface grooves on the aerodynamic performance of a NACA 4415 airfoil for small wind turbines. *Journal of Wind Engineering and Industrial Aerodynamics*. 206. doi.org/10.1016/j.jweia.2020.104263.

Lu, S, Liu, J & Hekkenberg, R. 2021. Mesh properties for rans simulations of airfoil-shaped profiles: A case study of rudder hydrodynamics. *Journal of Marine Science and Engineering*. 9(10). doi.org/10.3390/jmse9101062.

Lundberg Marcus et al. 2015. Aerodynamics of Insect Flight Effects of wind gusts on a rigid flapping NACA 0012 airfoil at Re = 3000. Thesis. Degree Project in Engineering Physics, First Cycle, SA104X at KTH Mechanics, Stockholm, Sweden.

Mamadaminov, U. 2013. Review of Airfoil Structures for Wind Turbine Blades. *REE 515 : Energy Engineering I, Fall, 2013*. (December, 6):1–8. Available from: https://www.researchgate.net/publication/271829785_Review_of_Airfoil_Structure_for_Wind_Turbine_Blades [Accessed 21 May 2026].

Mulligan, R. 2020a. Bio-inspired aerofoils for small wind turbines. In: *Renewable Energy and Power Quality Journal*. V. 18. Granada, Spain: European Association for the Development of

Renewable Energy, Environment and Power Quality (EA4EPQ). 753–758. doi.org/10.24084/repqj18.488.

Mulligan, R. 2020b. Bio-inspired aerofoils for small wind turbines. *Renewable Energy and Power Quality Journal*. 18:753–758. doi.org/10.24084/repqj18.488.

Muruga, J V, Jeyan, L & Mathew, B. 2021. *Albatross and Falcon inspired Bionic UAV: An Aerodynamic Analysis Article in*. Available from: https://www.researchgate.net/publication/352976419.

Osei, EY, Opoku, R, Sunnu, AK & Adaramola, MS. 2020. Development of High Performance Airfoils for Application in Small Wind Turbine Power Generation. *Journal of Energy*. 2020:1–9. doi.org/10.1155/2020/9710189.

Patel, KS, Patel, SB, Patel, UB & Ahuja, AP. 2014. CFD Analysis of an Aerofoil. *International Journal of Engineering Research*. No. 3(No.3):154–158. Available from: www.uvpce.ac.in.

Pellerito, V, Hassanalian, M, Sedaghat, A, Sabri, F, Borvayeh, L & Sadeghi, S. 2019a. Performance analysis of a bioinspired albatross airfoil with heated top wing surface: experimental study. In: *AIAA Propulsion and Energy Forum and Exposition, 2019*. American Institute of Aeronautics and Astronautics Inc, AIAA. doi.org/10.2514/6.2019-4319.

Pellerito, V, Hassanalian, M, Sedaghat, A, Sabri, F, Borvayeh, L & Sadeghi, S. 2019b. Performance analysis of a bioinspired albatross airfoil with heated top wing surface: experimental study. In: *AIAA Propulsion and Energy Forum and Exposition, 2019*. American Institute of Aeronautics and Astronautics Inc, AIAA. doi.org/10.2514/6.2019-4319.

Prasad, SU, Prasad Uppu, S, Manisha, D, Dharani Devi, G, Chengalwa, P & Vaishnavi Devi, B. 2018. Aerodyanmic Analysis of a Dragon Fly Abrasive water jet machining View project CFD Analysis View project Aerodynamic Analysis of a Dragonfly. *Journal of Advanced Research in Fluid Mechanics and Thermal Sciences Journal homepage*. 51:31–41. Available from: www.akademiabaru.com/arfmts.html.

Rao, KS, Chakravarthy, MA, Sreedhara Babu, G, Rajesh, M & Professors, A. 2018. MODELING AND SIMULATION OF AEROFOIL ELEMENT. *International Research Journal of Engineering and Technology*. 5(2). Available from: www.irjet.net.

Sedaghat, A & Mirhosseini, M. 2012. Aerodynamic design of a 300 kW horizontal axis wind turbine for province of Semnan. In: *Energy Conversion and Management*. V. 63. 87–94. doi.org/10.1016/j.enconman.2012.01.033.

Seguro, J V & Lambert, TW. 2000. Modern estimation of the parameters of the Weibull wind speed distribution for wind energy analysis. *Journal of Wind Engineering and Industrial Aerodynamics*. 85:75–84. doi.org/10.1016/S0167-6105(99)00122-1.

Sharma, S. 2016. An Aerodynamic Comparative Analysis of Airfoils for Low-Speed Aircrafts. *international journal of engineering research and Technology*. 5(11):525–529. Available from: www.ijert.org.

Sreedevi KNV et al. 2020. Effect of angle of attack on aerodynamic forces of symmetrical and unsymmetrical airfoil using wind tunnel. *International Journal of Mechanical and Production*. 10(3):5116–5122. Available from: www.tjprc.org.

Thakkar et al. 2013. Performance Analysis on Airfoil Model in Wind Tunnel Testing Machine (WTTM). *International Journal of Engineering Research and Applications (IJERA)*. 3(4):2094–2103. Available from: www.ijera.com.

Verma, M. 2020. Wind Farm Repowering Using WAsP Software – An Approach for Reducing CO2 Emissions in the Environment. In: *Encyclopedia of Renewable and Sustainable Materials*. S. Hashmi & I.A. Choudhury, Eds. Oxford: Elsevier. 844–859. doi.org/https://doi.org/10.1016/B978-0-12-803581-8.11001-X.

Wang, D, Li, H, Wu, F & Wang, L. 2016. *Modelling Analysis of Methods for Wind Turbine Annual Energy Production*.

Wang, L, Shi, F, Wang, Z & Liang, S. 2022. Blockage Effects in Wind Tunnel Tests for Tall Buildings with Surrounding Buildings. *Applied Sciences (Switzerland)*. 12(14). doi.org/10.3390/app12147087.

Xu, M, Xia, W, Zhang, X & Hu, S. 2024. Three-dimensional CFD model and aerodynamic analysis of dragonfly’s corrugated wing during gliding. In: *Journal of Physics: Conference Series*. V. 2879. Institute of Physics. doi.org/10.1088/1742-6596/2879/1/012052.

Zhang, L, Wang, K, Zhang, X, Liu, S, Jing, Z, Lu, J, Cui, X & Liu, Z. 2025. Research on the aerodynamic performance and bionic application of dragonfly wing corrugation. *Bioinspiration and Biomimetics*. 20(3). doi.org/10.1088/1748-3190/adc5bc.

Zhu, W, Liu, J, Sun, Z, Cao, J, Guo, G & Shen, W. 2023. Numerical Study on Flow and Noise Characteristics of an NACA0018 Airfoil with a Porous Trailing Edge. *Sustainability (Switzerland)*. 15(1). doi.org/10.3390/su15010275.

ANNEXURE A: COMPARISON OF WIND TUNNEL & CFD Cl vs VARIOUS ANGLE OF ATTACK

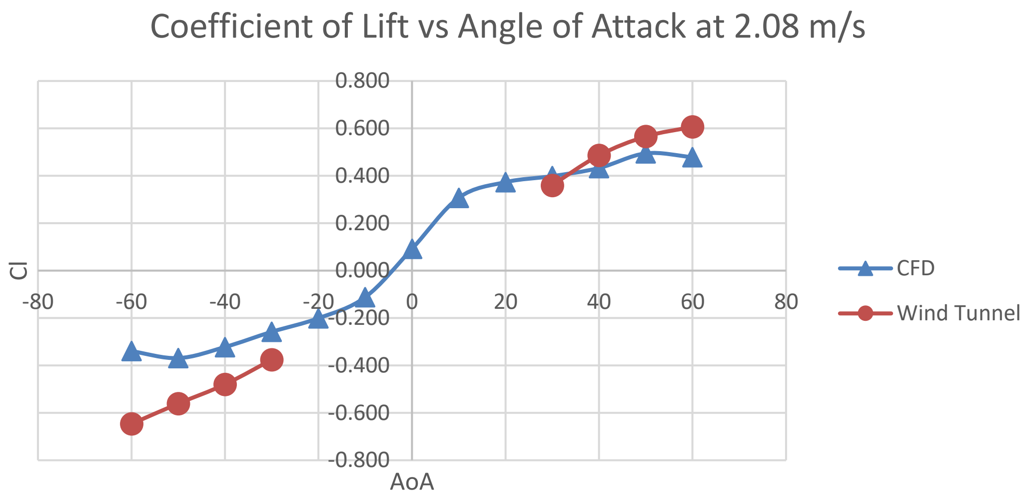

Figure 94: Comparison of CFD and Wind Tunnel Coefficient of Lifts against Angle of Attack at 2.08 m/s

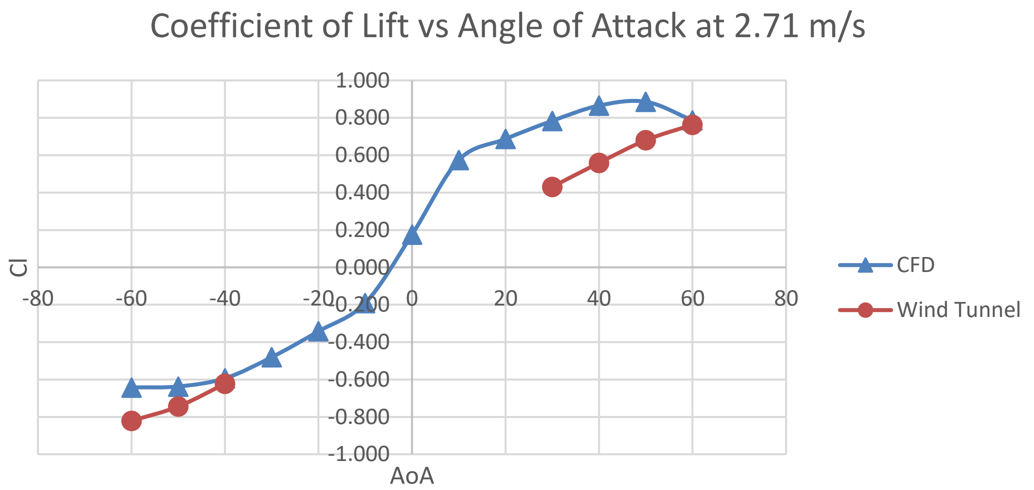

Figure 95: Comparison of CFD and Wind Tunnel Coefficient of Lifts against Angle of Attack at 2.71 m/s

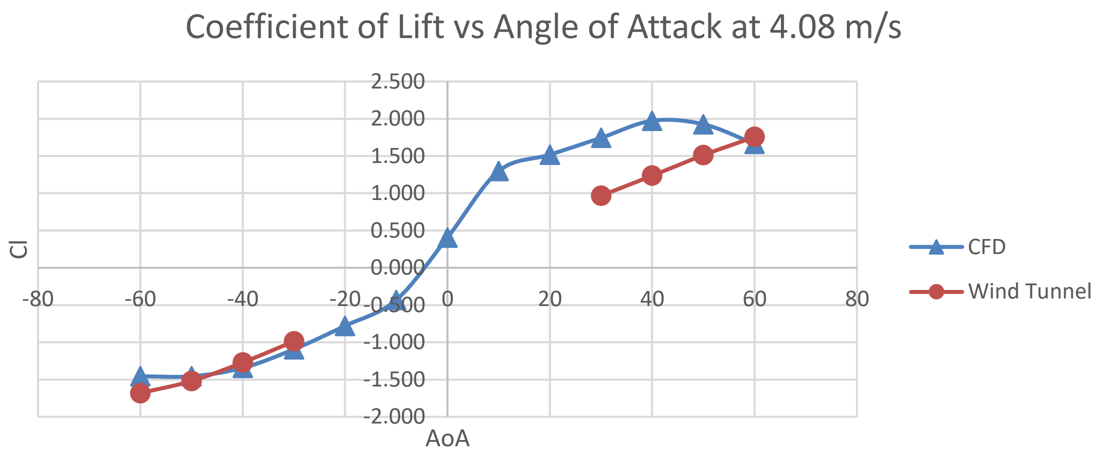

Figure 96: Comparison of CFD and Wind Tunnel Coefficient of Lifts against Angle of Attack at 2.71 m/s

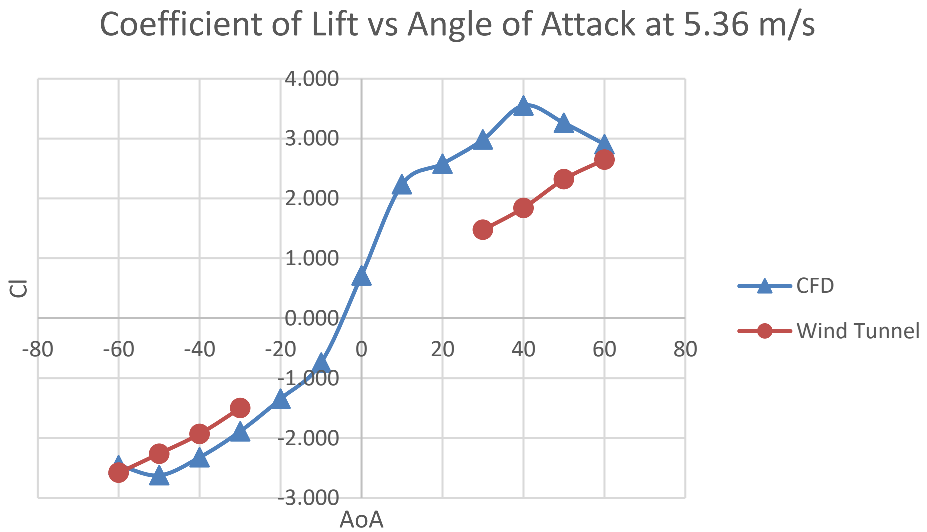

Figure 97: Comparison of CFD and Wind Tunnel Coefficient of Lifts against Angle of Attack at 5.36 m/s

ANNEXURE B: COMPARISON OF WIND TUNNEL & CFD Cd vs VARIOUS ANGLE OF ATTACK

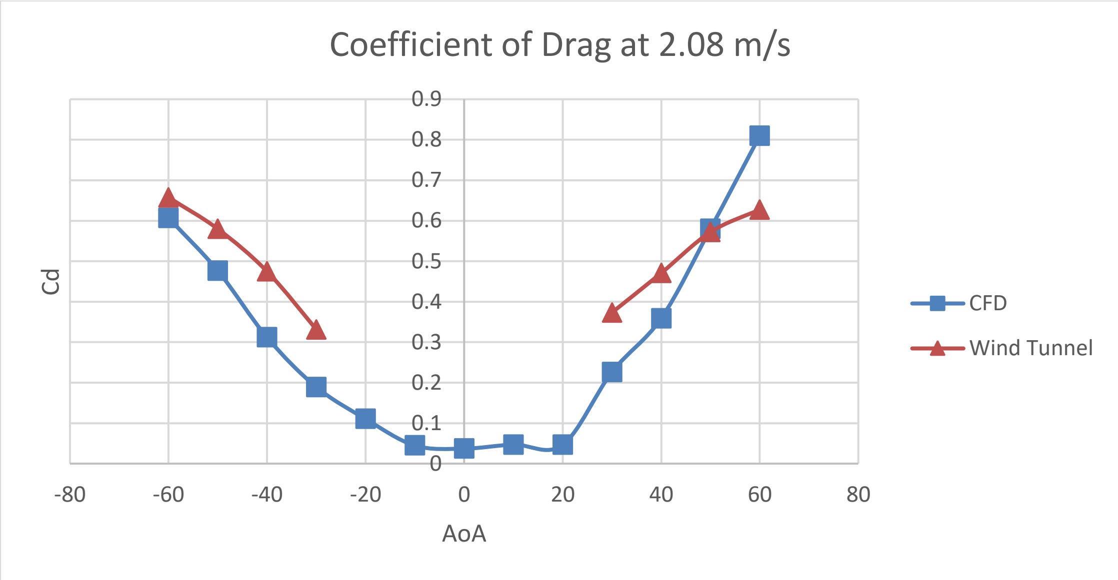

Figure 98: Comparison of CFD and Wind Tunnel Drag Coefficient against Angle of Attack at 2.08 m/s

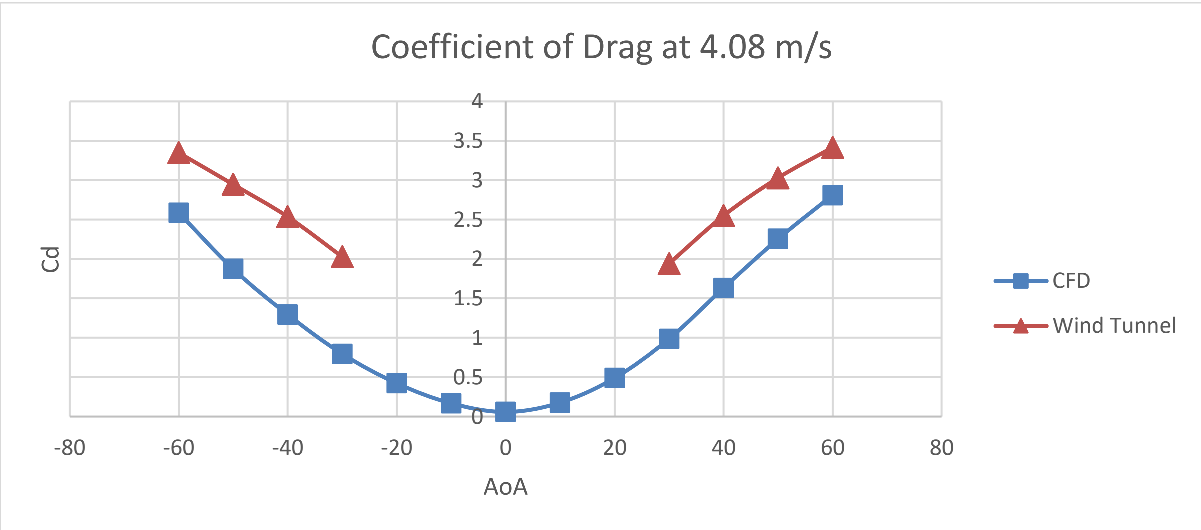

Figure 99: Comparison of CFD and Wind Tunnel Drag Coefficient against Angle of Attack at 4.08 m/s

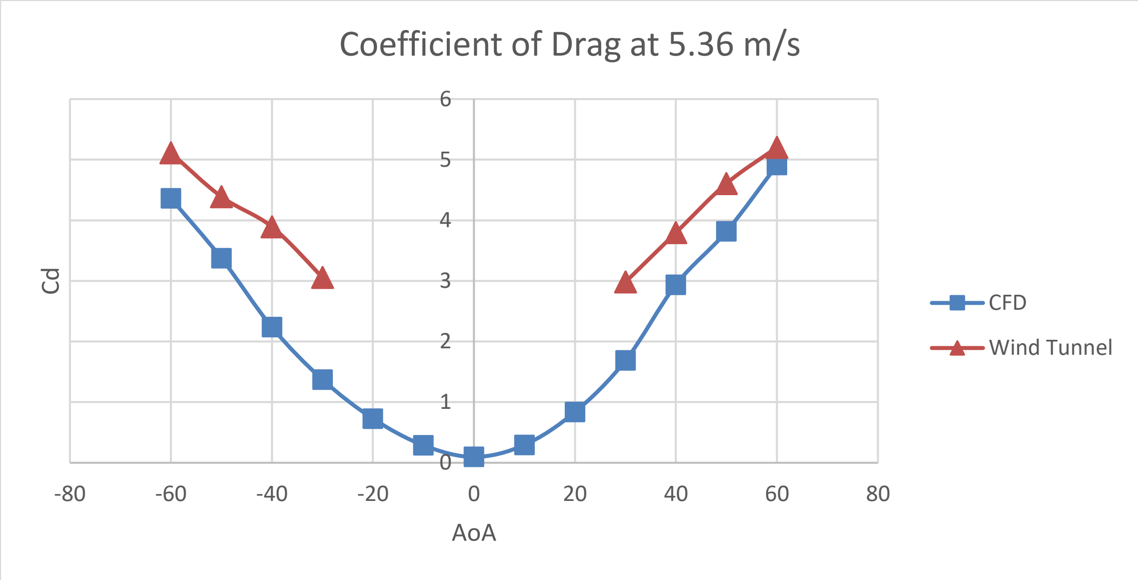

Figure 100: Comparison of CFD and Wind Tunnel Drag Coefficient against Angle of Attack at 5.36 m/s